INORGANIC ELECTROSPUN NANOFIBERS: FROM RATIONAL CATALYST DESIGN TO POWER GENERATION MATERIALS

A Dissertation

Presented to the Faculty of the Graduate School

of Cornell University

In Partial Fulfillment of the Requirements for the Degree of

Doctor of Philosophy

by

Nathaniel S. Hansen

January 2012

INORGANIC ELECTROSPUN NANOFIBERS: FROM RATIONAL CATALYST DESIGN TO POWER GENERATION MATERIALS

Nathaniel S. Hansen, Ph. D.

Cornell University 2012

Purely inorganic electrospun nanofibers containing iron and nickel catalytic nanocrystals are generated via sol-gel chemistry, with those nanocrystals in various concenctrations as well as locations by coaxial electrospinning. These nanofibers, following thermal treatment and precursor crystallization, are then applied as catalysts to the alkaline hydrolysis of glucose where they display conversions that increase with increasing catalyst concentration at the surface of the nanofiber. However, a long pretreatment drying time is required to reactivate the entrained catalyst. To decrease the pretreatment drying time a new fabrication method is developed; binding high concentrations of metal salts to a water-soluble polymer, electrospinning and using thermal treatments to remove the polymer and crystallize the metal salts. Nanofibers of a variety of morphologies and concentrations are fabricated through this approach and applied to the alkaline hydrolysis of glucose. These results detail that by increasing the concentration of available catalytic surface area within the diffusion length scale of the reactant, the temperature range at which near pure hydrogen is produced increases nearly 60℃. Subsequently this highly loaded water based electrospinning approach is used to generate nanofibers for a variety of applications. The electrical conductivity of these nanofibers are found for a variety of metals, including copper, iron, nickel and cobalt, and shown to be: tunable with the crystal

morphology within the nanofiber matrix, orders of magnitude higher than conductivities reported for other one dimensional materials, and directionally controlled by the anisotropy of the nanofiber mat. The magnetic properties of iron, nickel, and cobalt nanofibers are shown to be a function of both size and temperature ranging from near superparamagnetic behavior to highly coercive as controlled by precursor inclusion and thermal treatment procedure. Alternating layers of aligned nanofibers are subsequently used to overcome curling effects caused by volume loss during thermal treatment. By orienting perpendicular layers next to each other, axial shrinkage is minimized thereby maintaining long, linear nanofibers as well as flat, macroscopic mats. Finally, using the highly loaded water-based technique and the alternating layers of nanofibers, preliminary nanofibrous materials are synthesized for power generation applications such as lithium ion battery anodic materials and thin film photovoltaic devices. These materials display great promise due to high surface areas containing proper band gap or high capacity materials, but many future works are proposed for these materials.

BIOGRAPHICAL SKETCH

Nathaniel S. Hansen, or Nate, was born in Ontario, OR, and lived in Cambridge, ID, and Boise, ID, until the age of 2 when he moved to Moscow, ID. There Nate attended McDonald Elementary, Moscow Junior and Moscow Senior High School while pursuing many athletic activities including varsity soccer and golf as well graduating with highest honors. Following high school graduation, Nate attended both the University of Idaho and University of Rhode Island finishing with a B.S. from the University of Rhode Island in chemical engineering. During his undergraduate experience, Nate participated in a variety of research projects culminating in a research team Nate led receiving first place in a NASA sponsored statewide research competition and Nate individually receiving the Warren Award for Creativity in Research. Nate then moved on to Cornell University to pursue a Ph.D. from the School of Chemical and Biomolecular Engineering. While at Cornell, Nate presented at many national and local conferences including the American Institute of Chemical Engineers, the Materials Research Society, and the American Chemical Society. Nate also won the best oral presentation for his 4^{th} year oral presentation during the School of Chemical and Biomolecular Engineering Symposium.

This thesis is dedicated to my mother, Jennifer Hansen, for her unending support, unconditional love and guidance, and never letting me lose sight of what is important. Without you, none of this would have been possible. I thank you and I love you.

ACKNOWLEDGMENTS

I would like to acknowledge first and foremost Professor Yong Lak Joo for the guidance, support, ideas, and discussions pertaining not only to this work but to my development as a scientist, an engineer, and as a researcher. His help was invaluable and greatly appreciated. I would also like to thank my research group members, both past and present, including Dr. Jeanne Panels, Dr. Brian Pasquini, Dr. Colman Carroll, Dr. Edward Zhumayev, Professor Vibha Kalra, Dr. Jung Lee, Dr. Daehwan Cho, Jay Park, Bryan Rolfe, as well as undergraduate researchers Sasha Nayadich, David Smith, Hyesueng Chung, Tiffany Chio, and Linh Nguyen. Further, I must acknowledge tremendous support from collaborators in Professor Wiesner's group at Cornell University, specifically Hiroaki Sai, Juho Song, and Morgan Stefik who have helped with discussing potential block copolymers used in nanofiber synthesis. Inter-departmental collaborations with Professor Archer's research group, specifically Zichao Yang, have helped analyze nanofibers as anodes in lithium ion batteries, and with David Moore in Professor Hanrath's research group to analyze the absorption of PbSe nanofibers as well as the charge transport characteristics of ZnO and NiO nanofibers. External collaborations with researchers at Columbia University in Professor Park's research group, specifically Tom Furguson, have been crucial for the development of catalytically active nanofibers for biomass reforming. Great thanks must also be given to a variety of CCMR staff including John Hunt, John Grazul, Maura Weathers, Steve Kriske, Jon Shu, Yuanming Zhang, and Philip Carubia.

TABLE OF CONTENTS

LIST OF FIGURES

LIST OF TABLES

LIST OF ABBREVIATIONS

FTIR- Fourier Transform Infrared Spectroscopy

XRD- X-Ray Diffraction

TEM- Transmission Electron Microscopy

SEM- Scanning Electron Microscopy

XPS- X-Ray Photoelectron Spectroscopy

EDAX- Energy Dispersive X-Ray Spectroscopy

RGA- Residual Gas Analysis

GC- Gas Chromatography

TGA- Thermogravimetric Analysis

DSC- Differential Scanning Calorimetry

NMR- Nuclear Magnetic Resonance

CHAPTER 1

INTRODUCTION

Nanomaterials and size-dependent properties

Nanomaterials have long been identified as an exciting and groundbreaking field due to the size dependent properties generated when decreasing one or more dimension of a material below the micron level.[1] A few of the increased functionalities able to be accessed in this way are an increased surface area to volume ratio,[2] size dependent photon absorption and tunable band-gaps for photon absorbing materials,[3] control of magnetic coercivity in otherwise highly coercive materials,[4] and many others. The increase in surface area to volume ratio is especially important to processes such as catalysis where only the surface of the material is defined as the area functional to the application. With an increase in surface area to volume ratio, more of the material is available to contribute to the reaction. This is especially important when using expensive, rare-earth catalysts and results in higher catalytic efficiencies with lower loading of the catalytic material.[5] Another very exciting application of nanomaterials is in light harvesting materials for energy production. Within these materials, a photon is absorbed by an electron and promoted to the material's conducting band. This electron can then be transferred and used for electricity, while the corresponding hole needs to be transferred as well. Nanomaterials have the unique ability to control the energy required to promote the electron to the conducting band, and thus control the wavelengths of photons that will be absorbed, thereby allowing the optimization of the photon absorbing material for typical sunlight. This is known as having a tunable band-gap, and occurs when the diameter of the photon absorbing material decreases to the length scale of the

wavelength of the electron wave function for the electron being promoted. At this size, the materials become termed ‘quantum confined’, and the energy required to promote an electron to the conducting band, or the band-gap, increases with decreasing material diameter. Therefore, by controlling the size of the nanomaterial, the wavelength absorbed can be controlled and optimized to generate the most energy and increase the efficiency of the photovoltaic device.[6] Another exciting use of nanomaterials is in their magnetic property control. When a magnetic field stronger than the saturation field of the material is applied to a magnetically active crystal, all of the dipoles within the crystal align themselves with the applied magnetic field. However, when the magnetic field is then removed, the dipole of the crystal can return to its native state, can remain strongly aligned, or can fall somewhere in the middle. The amount of dipole remaining after the removal of the magnetic field is a measure of the material’s magnetic coercivity. If the material maintains a strongly aligned dipole, it has a high coercivity, but if it returns to its ground state and has no memory of the field, it is said to be superparamagnetic. Both of these states have great advantages for different applications – highly coercive materials would be useful in data storage while superparamagnetic materials could be useful in medical applications or separations. Further, the magnetic coercivity of materials has been shown to be a function of crystal size. Nanoparticles have been used to show that the magnetic coercivity of a material can be controlled by decreasing the particle size and particle density. The decrease in the nanoparticle size decreases the effect of the neighboring atoms’ dipole on each other atom, and thus decreases the relaxation time for the entire material to return to its ground state, thereby generating materials that are superparamagnetic at room temperature.[7]

Nanomaterials, though, come in many shapes and sizes with each having their own unique benefit. Near-spherical nanomaterials, termed generically nanoparticles,

have been used extensively in the aforementioned applications, but have been shown to have a few significant drawbacks, most importantly their susceptibility to aggregation. When these nanoparticles aggregate, due to high surface energy and high mobility, the advantage of increased surface area to volume ratio generated by decreasing the size of the particle is lost.[8] To remedy this, many methods have been proposed for controlling these materials' location. A few of these include adding surface functionalization to increase interaction with the solvent,[9] placing them within block copolymers,[10] placing them within a high aspect ratio one-dimensional support,[11] or generating the nanomaterial itself to be one-dimensional [12] thereby increasing the anisotropy and thus the mechanical support they offer each other. Block copolymer directed nanoparticles have been shown to have very exciting properties with the ability to generate polymer-metal hybrid structures in a variety of morphologies, or purely inorganic structures following the removal of the polymer component.[13] However, to generate highly directive nanoparticle-block-copolymer systems with high concentrations of nanoparticles, expensive block copolymers with high chi parameters must be synthesized, thereby generating barriers to significant industrial use.[14] Surface functionalization of nanoparticles to increase the nanoparticle to solvent interaction has been shown to decrease the aggregation phenomenon, but with high surface coverage of oligomers on the nanoparticle, the nanomaterials lose many functionalities such as catalytic activity.[15]

One-dimensional materials

One dimensional materials, whether as a support or as the active material itself, have emerged as a very exciting route to control nanostructures in many applications due to maintenance of extremely high surface area to volume ratios [16] and increase in property control.[17] A number of methods for synthesizing so called one-

dimensional materials, materials with a length at least an order of magnitude greater than the width or diameter, have been developed. Two of the more popular methods are the template synthesis method and the catalytic growth mechanism.

In the template synthesis method, a guiding template, such as an Anodisc, is used to control reaction location within its patterned, uniform pores (diameter 10-500 nm, length 1-10 microns). Therefore, due to a localized reaction within these pores, nanowires of similar dimensions to the original pores are collected after the guiding template is removed, typically by strong base.[18] The catalytic growth mechanism uses 10-100 nm catalytic particles placed on a substrate where a reaction is catalyzed between the particle and the substrate generating a nanowire capped on one side by a silicon substrate and the other a gold nanoparticle. Subsequently the nanowire must be removed from both the substrate and the catalytic particle to collect uninhibited nanowires.[19]

The advantages of the nanowires produced via these systems are numerous. The nanowires produced have monodisperse diameters,[20] are often single crystal materials,[21] and can have a variety of crystal structures as controlled by temperature, pressure, and catalyst structure [22] which is useful in many electromagnetic and catalytic studies. However, these systems also have many disadvantages, especially when looking to scale these synthesis processes to an industrial scale. First, the reactions are typically batch processes and would be difficult to make continuous.[23] Second, this production scheme is very expensive often involving toxic solvents.[24] The single use Anodisc template and the catalytic nanoparticles are both very expensive, and the removal processes associated with these procedures are difficult. Third the materials that are produced have relatively low aspect ratios when compared with other processes.[25] And finally, multicomponent, core-shell, or other more complicated nanowire morphologies are

difficult to produce.[26, 27]

Electrospinning

One method that can overcome these drawbacks is the process of electrospinning.[28] Electrospinning requires a polymeric or ceramic solution of proper viscosity (0.1-1 Poise) to be fed through a thin metallic spinneret (>18 gauge) where it is met by a high electric field (~1 kV/cm). This electric field generates repulsive forces that eventually overcome the surface tension of the solution and result in the emission of a linear jet toward a grounded collector. During this linear region the jet diameter decreases in diameter an order of magnitude. The jet eventually proceeds through a bending and whipping instability where further solvent evaporation occurs and the majority of the stretching occurs. Subsequently, the solidified nanofibers are collected on a grounded collector and taken for subsequent use, characterization, or further chemical reaction or thermal treatment.[29]

Electrospinning has a key disadvantage that can hinder the applicability of nanofibers produced. The nanofibers produced do not typically have a monodisperse diameter like the other methods for producing high-aspect ratio materials.[30] This could affect their use in some applications such as light harvesting or superparamagnetism, but may be acceptable in others such as electrically conductive membranes, catalytic applications, and filtration. However, the advantages of this process are numerous. First, the nanofibers produced have aspect ratios that can reach semi-infinite.[31] Second, electrospinning can utilize a solvent-free or water-based process removing toxic solvents that otherwise would require complicated solvent capture systems and expensive safety precautions in scale up.[32] Third, the electrospinning process can be scaled easily using gas assisted electrospinning to increase flow rates by more than an order of magnitude and allow for multi-nozzle

systems to be used to increase overall nanofiber production rate.[33] Fourth, the nanofiber composition is able to be controlled. Electrospun nanofibers have been synthesized from many pure homo-polymers,[34] homo-polymers including pre-synthesized nanoparticles,[35] block copolymers,[36] block copolymers directing surface functionalized nanoparticles,[37] pure ceramics,[38] ceramics including pre synthesized and *in-situ* crystallized nanoparticles,[39, 40] purely metallic and metal oxide nanofibers,[41] and more. Finally, one of the most advantageous benefits of this system is the diversity of the morphologies that can be produced by utilizing multi-axial electrospinning. Coaxial electrospinning utilizes similar electrically driven jet characteristics, but two solutions are fed into the process – one through a core spinneret and one through a shell spinneret in a concentric ring structure.[42, 43] This in turn, generates well defined core – shell structures due to the high solution viscosity and rapid solvent evaporation of the electrospinning process not allowing for mixing between the core and shell solutions. Some diverse materials have already been synthesized, such as a core of di-block copolymers containing prefabricated surface functionalized nanoparticles that are structure directed by the block copolymer, with a shell of a pure silica that serves as a thermally stable reactor vessel thereby enabling high temperature annealing to take place to generate phase separation within the core.[37]

Here the process of electrospinning is used to generate purely inorganic nanofibers of a variety of morphologies for many applications. Inorganic catalytic monoaxial and coaxial nanofibers are generated from sol-gel chemistry and *in-situ* precursor crystallization to form catalytic nanoparticles for the alkaline hydrolysis of glucose. It is seen that high conversions are achieved by tuning high concentrations of catalyst to the surface of the nanofiber. However, these silica nanofibers are plagued by catalytic deactivation due to high water absorption by the silica substrate.

Therefore, a new method to generate inorganic catalytic nanofibers is produced by binding high concentrations of metal/ceramic precursors to a water soluble polymer and electrospinning. Subsequent thermal treatment removes the polymer and the precursor ligands, leaving purely inorganic nanofibers with a wide range of nanofiber morphologies only bound by the complexity of precursor inclusion and thermal treatment conditions. These nanofibers display even greater catalytic activity than the silica nanofibers and demonstrate that the control of the geometry and concentration of catalyst within the diffusion length scale of the reactant greatly influences the selectivity and the overall conversion within the alkaline hydrothermal treatment of glucose. This highly loaded water based electrospinning method is subsequently extended to test for electromagnetic properties of purely metallic nanofibers as well as dual phase nanofibers. It is seen that the electrical properties greatly surpass those of other one-dimensional materials, and that directional electrical conductivity can be generated by generating anisotropic nanofiber mats. Control over the magnetic properties is also displayed as nanofibers displaying superparamagnetic and high magnetic coercivities are generated and controlled by crystal size, testing temperature, and thermal treatment procedure. Further, a method for maintaining flat, ordered nanofiber mats following thermal treatment is generated using alternating aligned layers of nanofibers. By alternating the layers of nanofibers, it is shown that axial contraction is limited allowing for long, linear nanofibers to be maintained thereby overcoming the curling phenomenon that had previously plagued inorganic nanofiber mat integrity. These materials are also being tested in many power generation applications including as lithium ion battery anodes due to structure, size, and concentration control within highly conductive nanofibers. Finally, ZnO, NiO and PbSe nanofibers are also in the process of being tested within thin film photovoltaic devices due to the high electrical conductivities of thin ZnO and NiO nanofibers, as

well as crystal size control within PbSe nanofibers. Ongoing work and future directions are detailed the final section of Chapter 9.

CHAPTER 2

INORGANIC NANOFIBERS WITH TAILORED PLACEMENT OF IRON NANOCATALYSTS FOR THE HYDROGEN PRODUCTION VIA ALKALINE HYDROLYSIS OF GLUCOSE

1. Introduction

The production of hydrogen gas as a fuel, especially in H_2/O_2 fuel cells, has prompted a significant amount of research due to the benign byproducts.[44, 45] Yet, the production of H_2 streams contaminated with CO and CO_2 [46] as well as problems with the safe storage of hydrogen prior to usage [47] have plagued the application of this technology. An appealing approach for CO and CO_2 free generation of fuel gas with high hydrogen yields has recently been proposed through the alkaline hydrothermal treatment of cellulosic biomass over various metal catalysts under mild reaction conditions (200 ~ 300 ºC, 1 atm).[48]

Similar reaction mechanisms have been shown to increase efficiencies when the catalyst length scale is decreased to the nanoscale thereby increasing the surface area to volume ratio and thus the number of available active sites.[49] However, even when the catalysts are formed with diameters of less than 20 nm, there are still limitations to the applicability of these materials. Nanoparticles, especially magnetically active nanocrystals,[50] have shown a strong affinity to aggregation that limits their effectiveness as catalysts due to the significant reduction in interfacial volume.[51],[52] Therefore, containing prefabricated nanoparticles [53] or creating

these crystals in-situ [54] in one-dimensional materials has been proposed and shown to lessen the aggregation phenomenon while maintaining the high surface area to volume ratio gained by generating nanoscale structures.[55] Silica is commonly used as a catalyst support due to its chemically inert behavior [56] and the porosity of the matrix generates natural nucleation sites for crystallization while also limiting secondary nucleation during in-situ creation.[54] Many different catalysts, including platinum, rhodium, nickel, and iron have been tested in the alkaline hydrolysis of cellulose.[48] While iron shows a lower catalytic efficiency, it still presents many benefits including a low cost and a simple recycle scheme if the catalyst is magnetically active. In addition to the diversity of catalysts, wide array of biomass feed stocks - including cellulose, wood mass, and food waste - have been tested in similar reactions. However, according to a proposed reaction mechanism for cellulosic degradation, [57] a significant fraction of cellulosic materials breaks into glucose subunits and then react into hydrogen and other byproducts. Therefore, iron catalysts degrading glucose via the alkaline hydrothermal treatment may provide a good stepping stone to analyze the catalytic properties of inorganic nanofibers in converting cellulosic biomass to fuel gas, while still maintaining the low cost needed to make biomass conversion via alkaline hydrothermal treatment economically viable.

As mentioned previously, containing catalysts in one-dimensional materials has been shown to prevent aggregation while maintaining the high surface area to volume ratio and other functionalities afforded by using nanoparticles.[58] A convenient and inexpensive method for creating such one-dimensional nanosupports is electrospinning.[59] In the electrospinning process, solutions are fed through a

metallic spinneret where they are charged by a high electric field (~ 1 kV/cm). With a proper solution viscosity and applied electric field, surface forces caused by the electric field break the surface tension of the solution and results in the emission of a thin jet. Initially the jet is stable, but soon enters a bending and whipping instability where further stretching and solvent evaporation occur. The solidified jet is finally collected on a grounded plate forming randomly-oriented, nonwoven nanofiber mats.[28] Electrospinning has been shown to produce uniform nanofibers of diameter 50 nm – 1 μm from both polymers [60] and inorganics.[61],[62]

In particular, this new way of making nanoscale inorganic fibers by combining electrospinning and sol-gel synthesis holds the promise to incorporate multi-functionality to nanoscale fibers and mats in part by providing thermal stability (as high as 1000°C). In addition, being able to incorporate chemical synthesis such as the sol-gel method into electrospinning processes opens doors to a wide variety of novel nanoscale materials in many morphologies including hollow,[63] porous,[64] and those containing secondary materials such as inorganic crystals [65, 66] and pharmaceuticals.[67, 68] Studies on electrospinning, however, have generally been limited to fabrication and characterization of nanofibers, and have just begun to scratch at the surface of their applications in various areas including catalysis.

Coaxial electrospinning has also garnered attention due to its flexibility to create multi-layered morphologies in sub-micron scale fibers, thereby allowing the fabrication of more functional devices in many applications. This new processing scheme exhibits the possibility to greatly increase the catalytic efficiency of nanofibers containing inorganic catalysts. The use of inorganic catalysts in monoaxial nanofibers

generally gives rise to the spread of the catalyst throughout the diameter of the nanofiber. Therefore, there can be a potential mass transfer limitation for the small molecule to diffuse through the substrate and reach any catalyst located near the center of the nanofiber. Previous results have used a shell solution containing catalytic nanoparticles to be placed on the surface of a core solution made of a second material immiscible with the shell. However, when using two immiscible solutions in coaxial electrospinning there is the potential for delamination during repetitive use and subsequent loss of activity. Using a skin layer miscible with the core layer may prevent this delamination, while loading the skin with catalytic nanoparticles will reduce the mass transfer limitation due to a high concentration toward the surface of the nanofiber, and thus the waste of the catalyst can be minimized.

In the present study, monoaxial silica nanofibers containing iron species as well as coaxial nanofibers with a pure silica core and a silica shell containing high concentrations of iron nanocrystals were obtained by electrospinning precursor solutions, followed by thermal treatment. The parameters investigated to control the phase, size, and concentration of the nanocrystals are the precursor concentration and the thermal treatment conditions. The formation of monoaxial nanofibers and the control of the oxidation state of the iron nanocrystal will be discussed first. This will be followed by the use of these monoaxial nanofibers as catalyst systems in the alkaline hydrolysis of glucose to form fuel gas with very low levels of carbon monoxide and dioxide. To increase catalytic efficiency and reduce catalytic consumption, coaxial electrospinning was applied to produce nanofibers with a pure silica core and a silica shell containing high concentrations of iron nanocrystals. The

characterization of resulting coaxial nanofibers and their application to the more effective hydrolysis of glucose for fuel gas production is presented. Finally, the quantification of hydrogen production via residual gas analysis and the effect of pre-drying time of reactant-catalyst mixtures on the catalytic performance are addressed.

2. Experimental Methods

The sol gel chemistry procedure used requires three solutions: the first containing 1 gram of ethanol (EtOH) is added to 6.5 grams of TEOS (Sigma Aldrich) in a 100 ml beaker, the second of x grams of iron nitrate and 1 gram of EtOH is created and the third of 3 drops of concentrated HCl (Sigma Aldrich) and $(1.19 - 0.4x)$ grams of deionized water. The third is then added drop wise to the first solution while simultaneously being mixed. The second solution is then added to the resulting mixture and stirred vigorously. The resulting solution is heated to 50ºC for about 3 hours until gelation produces the proper viscosity.

Monoaxial nanofiber samples are created by electrospinning using a Harvard Apparatus PHD 2000 Infusion syringe pump flowing at 0.03 ml/min. Solution flows through a 22 gauge Hamilton N722 needle where it is met by a high electric field supplied by an HV ES3OP-5W Power Supply set to 20 kV and a needle to collector plate distance of 15 cm. Coaxial nanofiber samples were generated using the same equipment and the same electric field, but with an inner syringe of 24 gauge and an outer syringe of 18 gauge. The flow rates used in coaxial electrospinning were either an inner: outer of 0.02: 0.03 ml/min or 0.03: 0.02 ml/min depending on the desired overall Fe: Si ratio as compared with the shell Fe: Si ratio.

Following sample generation, the samples are placed in a Mullen Two Zone 1700ºC Tube Furnace for high temperature thermal treatment. In producing pure iron crystals, an oxygen depleted environment consisting of an atmosphere of 94% argon and 6% hydrogen was fed through the tube furnace at a flow rate of 0.8 cc/sec. The fibers were heated at 5ºC/min to 800ºC, held for 10 hours, and then cooled at 5ºC/min back to room temperature. Hematite crystals were produced by the same primary thermal treatment above followed by a second thermal treatment by reheating from room temperature at 5ºC/min to 800ºC for 10 hours under a stagnant air atmosphere and then cooling at 5ºC/min back to room temperature. Magnetite crystals were formed by heating fibers at 5ºC/min to 250ºC under stagnant air, holding for 1 hour and then cooling at 5ºC/min back to room temperature followed by a second thermal treatment by heating at 5ºC/min to 850ºC under flowing 100% argon flowing at 0.8 cc/sec, holding for 2 hours, and then quenching these fibers back to room temperature in stagnant air. These thermal treatment procedures are summarized in Table 1.

The samples are characterized through XRD using a Scintag Theta-Theta X-ray Diffractometer, TEM using an FEI Tecnai G2 T12 Spirit TEM STEM, SEM using a LEICA 440 SEM, and XPS using an SSX-100 X-ray photoelectron spectroscopy unit. To generate TEM cross section images the samples were first placed in an epoxy resin for 8 hours and then 70 nm cross sections were cut using a Leica Ultracut UCT Cryo-Ultramicrotome and microtomed using a DiATOME diamond knife. Thermogravimetric Analysis (TGA) was conducted using a T.A. Instruments Q500 TGA while Differential Scanning Calorimetry (DSC) was conducted using a T.A. Instruments Q1000 modulated DSC. The bulk phase weight loss data was conducted

on ceramic discs in the same 2 zone tube furnace discussed previously.

Mats of silica nanofibers containing iron and hematite nanocrystals were tweezed apart into centimeter long sections. These samples were then mixed with 0.5g of d-glucose (Sigma Aldrich) and physically mixed. 2.35g of 50 wt. % NaOH solution at 100ºC is then added to the solution. First, the solution is heated to 100ºC for 24 hours in air to evaporate entrained water. Next, 1-2 mg samples are taken and measured under DSC or TGA. These measurements are done under flowing N_2 and a heating rate of 2ºC/min from 100ºC to 300ºC. The area under the curve of the DSC is used to calculate the amount of heat given off due to a particular reaction, and then using the heat of reaction from the previously discovered chemical reaction [48] and mass of sample the percent conversion can be calculated. Using the amount of generated hydrogen and evaporated water the percent conversion can also be calculated from TGA. Bulk weight loss data was calculated in a similar way. This procedure consisted of treating the solution at 100ºC for seven days in air to release entrained water. The sample was then heat treated under argon at 10ºC/min to 100ºC, followed by thermal treatment at 2ºC/min from 100ºC to 300ºC and then cooling at 5ºC/min to room temperature. From the weight difference due to thermal treatment, the percent conversion can be calculated.

Mass spectroscopy analysis was performed using a Vulcan 3 130 Box Furnace with a leak valve attached to an Extorr XT200 Residual Gas Analyzer following the same thermal treatments and dry times listed in the bulk weight loss experimental setup. Finally, to more thoroughly understand the drying time requirement XRD analysis was performed on solids after various dry times. During these experiments

the sample was heated in air for *x* hours, cooled to room temperature in air, and immediately analyzed under XRD. FTIR analysis was performed on the samples prior to treatment with NaOH, following NaOH treatment after 1 hour drying, and following NaOH treatment after 24 hour drying time at 100ºC.

3. Results & Discussion

As-spun monoaxial silica nanofibers with three Fe: Si ratios (1:12, 1:6, and 1:4) are generated and shown through SEM images in Figures 1a, b, and c. It is observed that the diameter of as-spun nanofibers increases with increasing iron nitrate concentration, yielding average diameters of 251 $\pm$ 118, 403 $\pm$ 156, and 563 $\pm$ 203 nm, respectively. This trend is consistent with other results studying silica nanofibers containing an inorganic precursor.[39, 69] Such an increase in nanofiber diameter may be due to an increase in viscosity and a potential inhomogeneity caused by aggregation of metal precursors within the sol-gel solution. Figure 1d shows the diameter distribution of 300 fibers observed through SEM images for each Fe: Si ratio. The gelation time also decreases with increasing metal precursor concentration, resulting in a narrower window of spinnable viscosity for the production of ultrathin nanofibers.

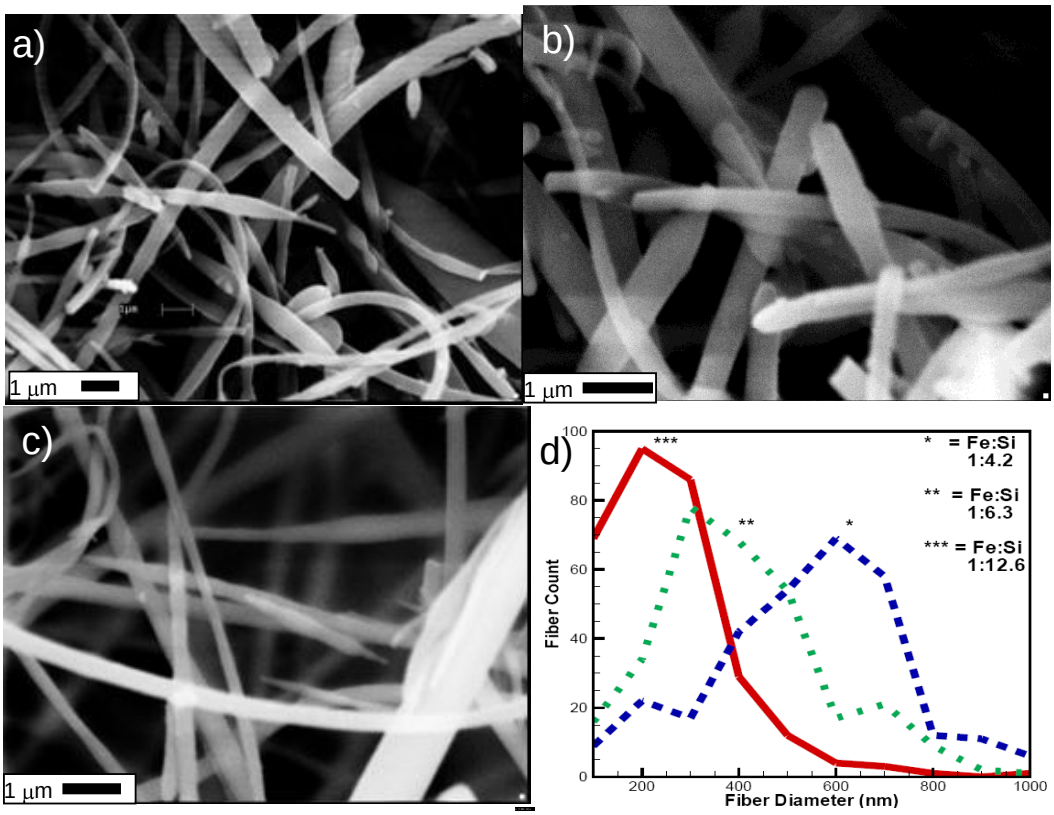

Figure 1. SEM images of as-spun fibers. a) Fibers with an Fe:Si ratio of 1:12, b) Fibers with an Fe:Si ratio of 1:6, c) Fibers with an Fe:Si ratio of 1:4, and d) The average diameter and distribution of diameters observed under SEM for as-spun fibers of different iron content.

Following the generation of precursor as-spun nanofibers, thermal treatment is required to generate functional catalytic nanocrystals in inorganic nanofibers. According to the predicted phase diagram [70] for the silica-iron system, the formation of iron and iron oxide crystals strongly depends on the temperature and partial pressure of oxygen present. In addition, due to complications with the production of nitrogen from the iron precursor, iron nitrate [$Fe(NO_3)_3$], a nitrogen and oxygen depleted environment must be used at initial crystallization. Therefore, in some cases a 100% argon and in others a mixture of 94% argon and 6% hydrogen was used. The use of stagnant air as a thermal treatment atmosphere was also used either to

oxygenate the crystal or to nucleate the iron precursor. The formation of iron, hematite, and magnetite nanocrystals in silica nanofibers via different thermal treatments and their characterization will be discussed in the following sections. Table 1 presents the thermal treatment conditions used to generate the respective oxidation states.

Crystal Formed	Step	Atmosphere	Conditions	Cooling
Pure Iron	1	94% Ar and 6% H_2	800 ºC for 10 hrs.	to RT at 5 ºC/min
Hematite	1	94% Ar and 6% H_2	800 ºC for 10 hrs.	to RT at 5 ºC/min
	2	Air	800 ºC for 10 hrs.	to RT at 5 ºC/min
Magnetite	1	Air	250 ºC for 1 hr.	to RT at 5 ºC/min
	2	Ar	850 ºC for 2 hrs.	quenching to RT in air

Table 1. Thermal treatment conditions for various iron species in silica nanofibers. The heating rate is kept at 5 ºC/min.

As-spun fibers are collected and heated to 800ºC for 10 hrs. under 94% argon 6% H_2 to obtain silica nanofibers containing pure iron metal crystals. Figure 2a, 2b and 2c show TEM images of microtomed cross- and longitudinal- sections of nanofibers with a Fe: Si ratio of 1:12, 1:6 and 1:4 after the thermal treatment.

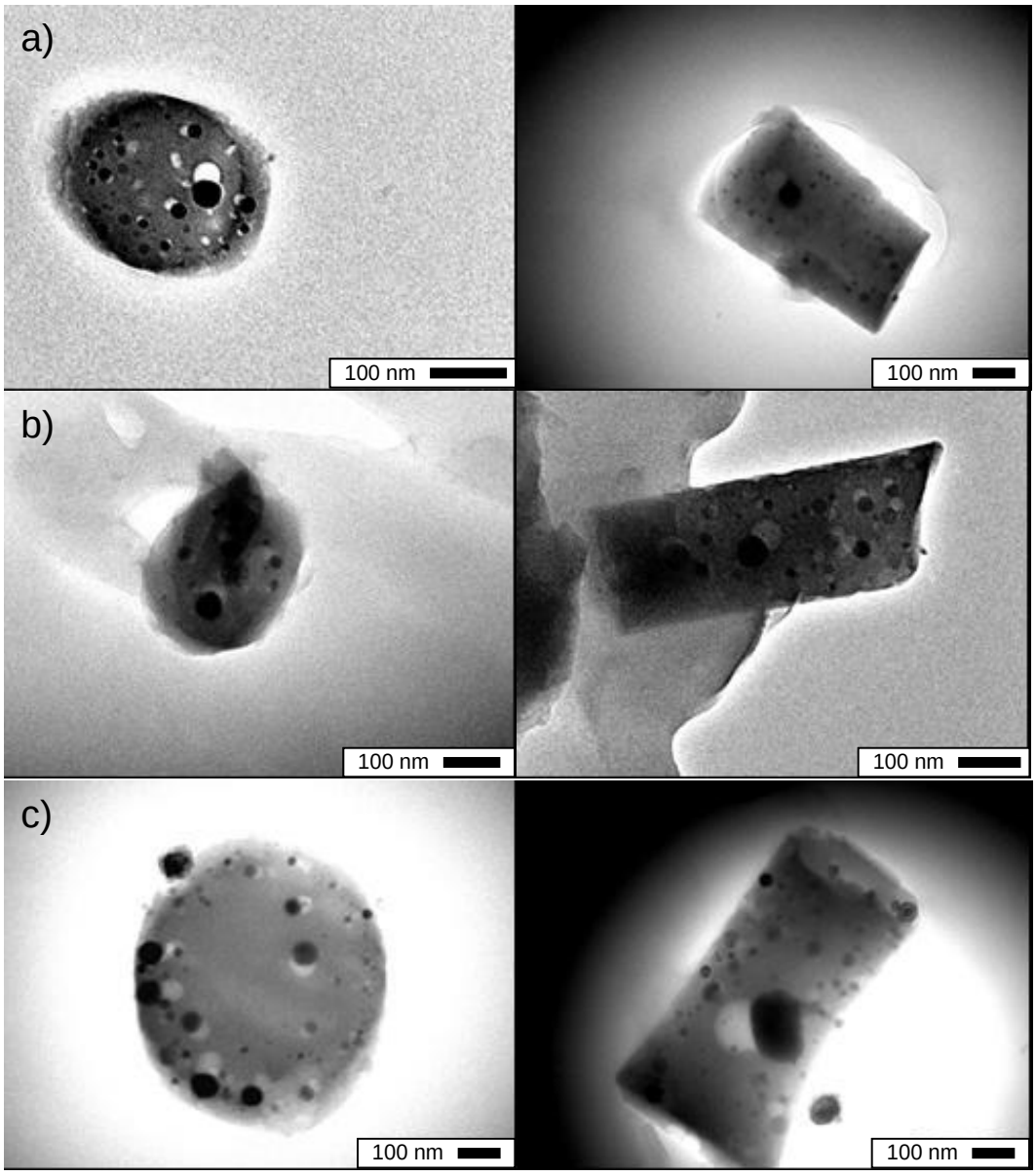

Figure 2. Monoaxial silica nanofibers treated under Argon/H_2 at 800 C for 10 hr. Microtomed cross sectional (left) and longitudinal (right) images of fibers containing a Fe: Si ratio of (A) 1:12, (B) 1:6, and (C) 1:4.

The distribution of crystal sizes and their location were obtained from these TEM images and summarized in Figure 3 together the XRD pattern after thermal treatment. Figure 3a presents the crystal size distribution observed in cross sectional images with respect to the amount of iron in the nanofibers. For this Figure, 10 microtomed cross

sectional TEM images were taken and crystal sizes observed in each image were documented to within 5 nm. It is observed that the average size of iron crystals in silica nanofibers under the same thermal treatment conditions increases with increasing the iron concentration. Fibers having a Fe: Si ratio of 1:12, 1:6 and 1:4 displayed average crystal diameters of 28.0 $\pm$ 15.8, 32.8 $\pm$ 14.1, and 48.7 $\pm$ 22.0 nm, respectively. It is also found that the distribution of the crystal diameters increases with increasing iron concentration. This, therefore, allows one of two possible conclusions about the crystallization process. Either nucleation is occurring in a homogeneous fashion where critical nuclei formation is time dependent, or there is a large amount of secondary nucleation occurring in nanofibers with high iron concentrations. Since there is a large distribution of crystal diameters formed in low iron content nanofibers, along with the fact that silica provides pores that can function as nucleation sites, it is perhaps more likely that heterogeneous nucleation is taking place with a large impact from secondary nucleation. A comprehensive study of the crystallization of metals in silica nanofibers using Cellular Automata meso-scale simulation is currently underway.

The XRD pattern in Figure 3b exhibit diffraction peaks at 2-theta angles of 43º, 45º, 51º and 65º. Peaks at 43º and 51º correspond to austenite (γ-iron) crystals, while those at 45º and 65º are identified as ferrite (α-iron). It should be noted that some peaks discussed here are slightly offset due to the fibrous morphology rather than powder morphology. In addition, there is a large diffraction peak at a 2-theta angle of 27º in fibers with a small Fe: Si ratio of 1:12, which is consistent throughout all fibers tested with that iron concentration and may correspond to the small formation of

quartz. The crystal size was calculated from the XRD peaks using the Scherrer Equation. This data was compared to the average crystal size determined previously for each iron phase and concentration as presented in Figure 3c. For the pure iron case, the crystal size from the Scherrer Equation is comparable to the average crystal size from TEM image analysis, and also shown to increase with increasing the iron concentration. The fraction of crystals along the radial direction for nanofibers with three different Fe: Si ratios are presented in Figure 3d. For this Figure, the same analysis was done to produce Figure 3a, but rather than the size of the crystal, the location of the crystal relative to the center of the nanofiber was probed. As shown in the Figure, a significant fraction of the crystal is in fact located inside the nanofiber with very little located near the surface.

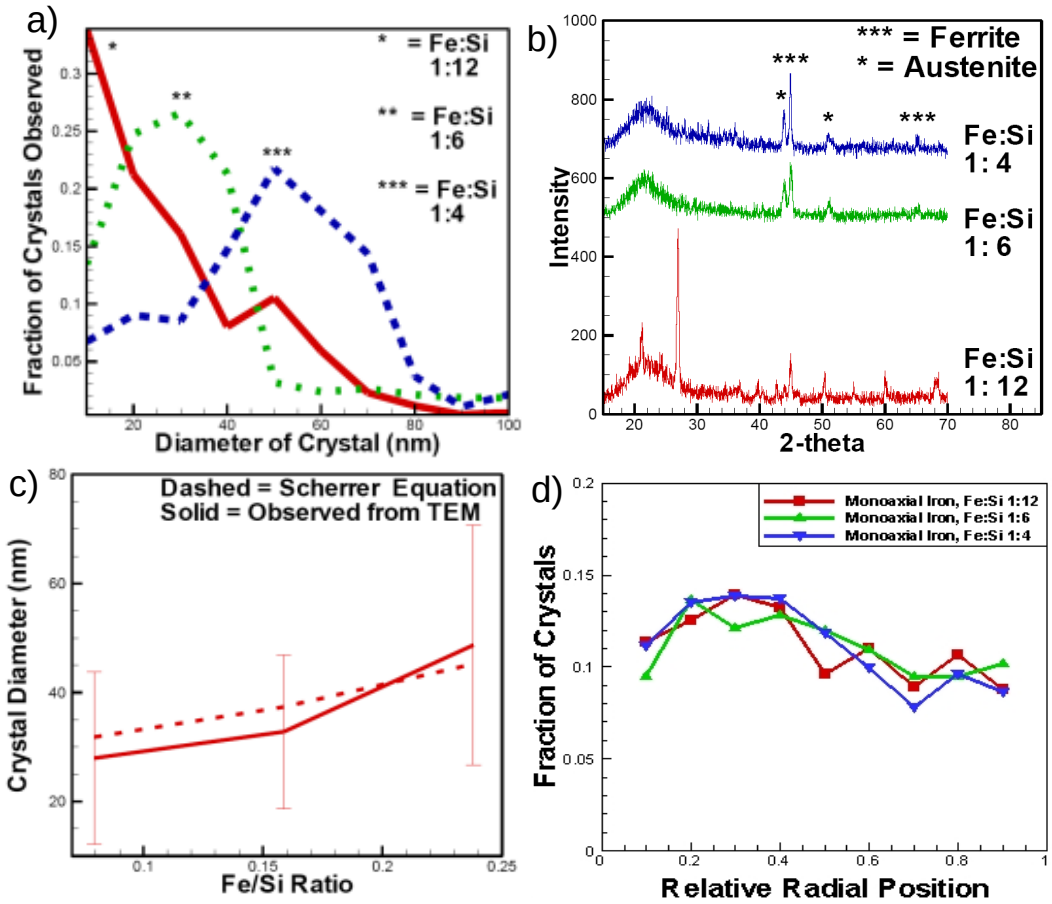

Figure 3. Characteristics of iron crystals in monoaxial silica nanofibers. a) distribution of crystal sizes observed in microtomed image, b) XRD pattern confirming the presence of iron crystals, ferrite and austenite, c) comparison of observed crystal diameter and calculation by the Scherrer equation, d) statistical measurements of the crystal location throughout the nanofiber diameter.

Following the formation of pure iron crystals, the oxidation state can be tuned by secondary thermal treatment. Therefore, the fibers were treated a second time to 800ºC for 10 hours under stagnant air. TEM images of microtomed cross sections and longitudinal sections of silica nanofibers containing hematite crystals with a Fe: Si ratio of 1:12, 1:6 and 1:4 are displayed in Figure 4a, b and c, respectively.

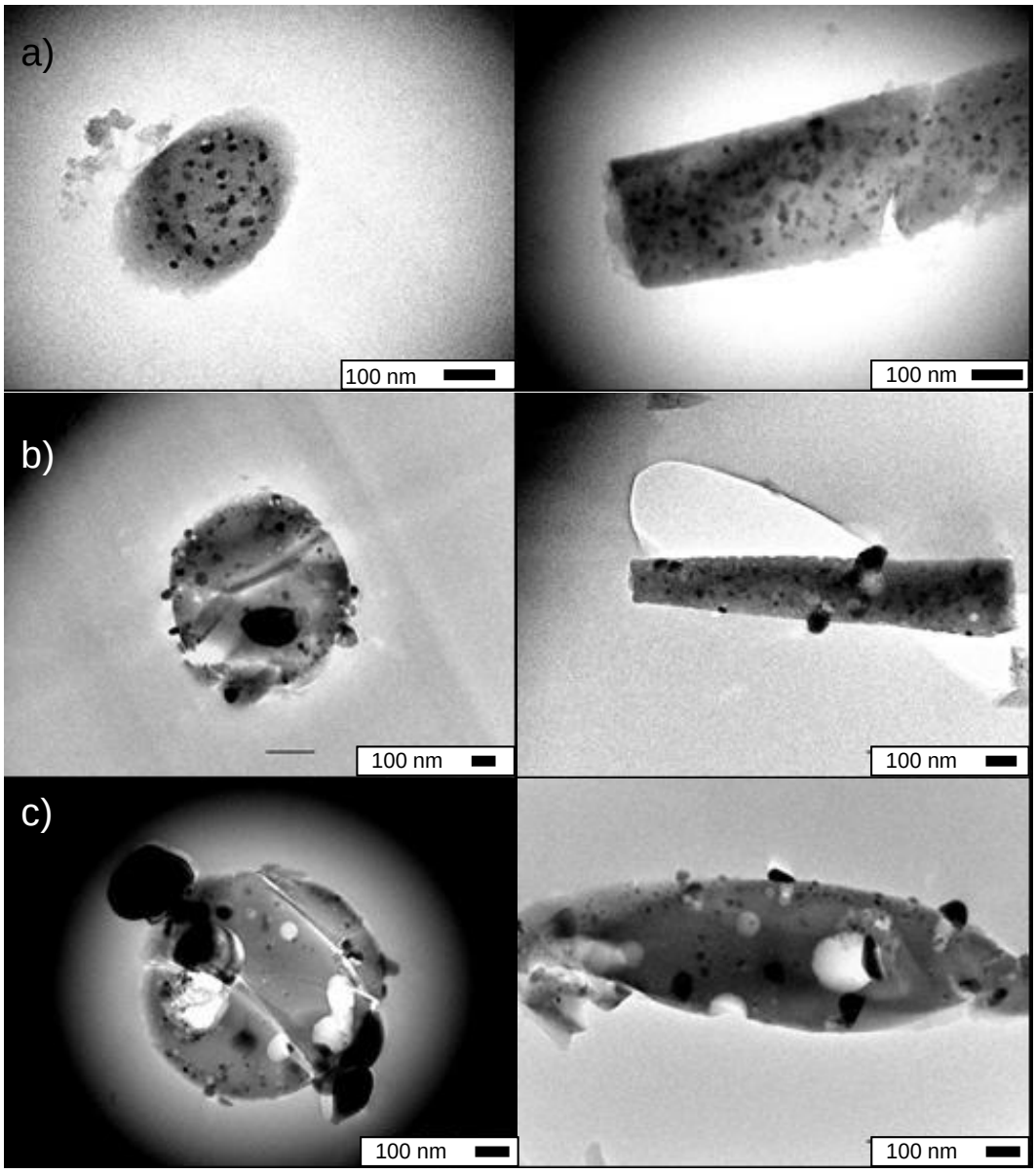

Figure 4. Nanofibers treated under Argon/H_2 at 800ºC for 10 hr. and then under stagnant air at 800 ºC for 10 hr. Microtomed cross sectional (left) and longitudinal (right) images of fibers containing a Fe: Si ratio of a) 1:12, b) 1:6, and c) 1:4.

The distribution of the crystal sizes with respect to the amount of iron in the fibers is calculated similar to the method used for Figure 3a and is presented in Figure 5a, indicating that the crystal size again increases with increasing iron concentration as shown by crystal diameters of 34.1 $\pm$ 20.1, 49.6 $\pm$ 15.4, and 51.1 $\pm$ 23.2 nm for

nanofibers with Fe: Si ratios of 1:12, 1:6 and 1:4, respectively. Additionally, the average crystal diameter increases from the pure iron case to the hematite case. This perhaps is due to the additional thermal treatment time allowing further crystallization iron in the presence of oxygen and further secondary nucleation to form larger crystal domains.

The XRD pattern for these nanofibers, as shown in Figure 5b, displays sharp diffraction peaks at a 2-theta angle of 33º, 36º, 41º, 50º, 54º, 58º, 62º and 64º, demonstrating the complete conversion of iron crystals into hematite crystals. As with the pure iron case, the crystal size was calculated using the Scherrer Equation and the XRD pattern discussed previously. This was then compared to the average crystal size determined by observation of TEM images. These two trends are presented in Figure 5c. Again, similar to the pure iron case, the hematite case demonstrated the fact that the crystal size from the Scherrer Equation and the average crystal size from observation are very similar and in both trends the crystal diameter increases with increasing iron concentration. In addition, with both the Scherrer Equation and the TEM observational average, the hematite case demonstrated larger crystals than the pure iron case.

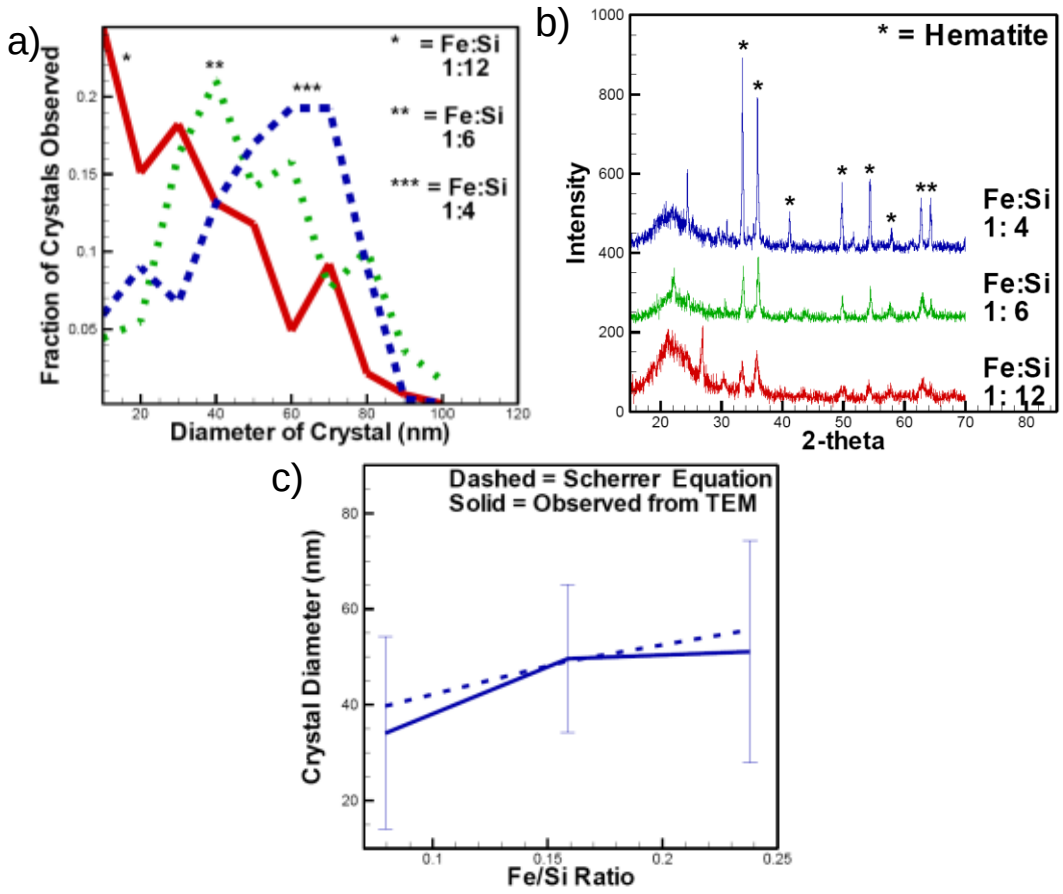

Figure 5. Characteristics of hematite crystals in nanofibers treated under Argon/H_2 at 800ºC for 10 hr. and then under stagnant air at 800 C for 10 hr. a) Distribution of crystal sizes observed in microtomed images at various iron contents, b) XRD pattern with strong hematite peaks confirming the complete conversion of iron to hematite, and c) comparison of observed crystal diameter and calculation by the Scherrer equation.

Following the fabrication of nanofibers with iron or hematite crystals, they were utilized as catalyst systems for the alkaline hydrolysis of glucose to produce fuel gas as shown in Figure 6. Two control samples were tested first, one with no catalyst and one with pure SiO_2 nanofiber supports. Next, samples with pure iron crystals and Fe: Si ratios of 1:12, 1:6 and 1:4 in SiO_2 nanofibers and a catalyst: glucose ratio of 1:10 were tested using DSC and TGA and are presented in Figure 6a. This data is calculated by the heat of reaction in DSC, the area under the DSC curve for a

particular reaction, and the total weight loss from TGA. Of significance is the very low conversion for the two control samples with no catalyst support at 12% and pure SiO_2 at 19%. The percent conversion then consistently increased to a maximum of 65% for fibers with a Fe: Si ratio of 1:4 and a catalyst: glucose ratio of 1:10. Figure 6a also displays general agreement between DSC and TGA in both number and trend. Bulk weight loss calculations in the tube furnace were then tested for the remaining samples due to the ease of this method, and the results are presented in Figure 6b. Here, three catalyst: glucose ratios (1:10, 1:5, and 1:3.33), and three Fe: Si ratios (1:12, 1:6, and 1:4) were tested, and the crystal type was also varied (ferrite to hematite). The same two control tests were also run: one with pure SiO_2 and one with no catalyst or support. These control tests from the bulk weight loss calculations are in general agreement with those from Figure 6a for the TGA and DSC tests run. Also, included in this Figure are the DSC results, presented as open squares whereas the similar catalyst loading and Fe: Si ratio scheme calculated through bulk weight loss is presented as closed squares for comparison.

From this Figure a few important observations can be made. As would be expected, increasing metal content, whether by increasing the Fe: Si ratio or by increasing the catalyst: glucose ratio, increases the catalytic efficiency. Furthermore, from the catalyst: glucose ratio of 1:5 tests it is apparent that the nanofibers containing pure iron crystals display significantly better catalytic efficiency than nanofibers containing hematite.

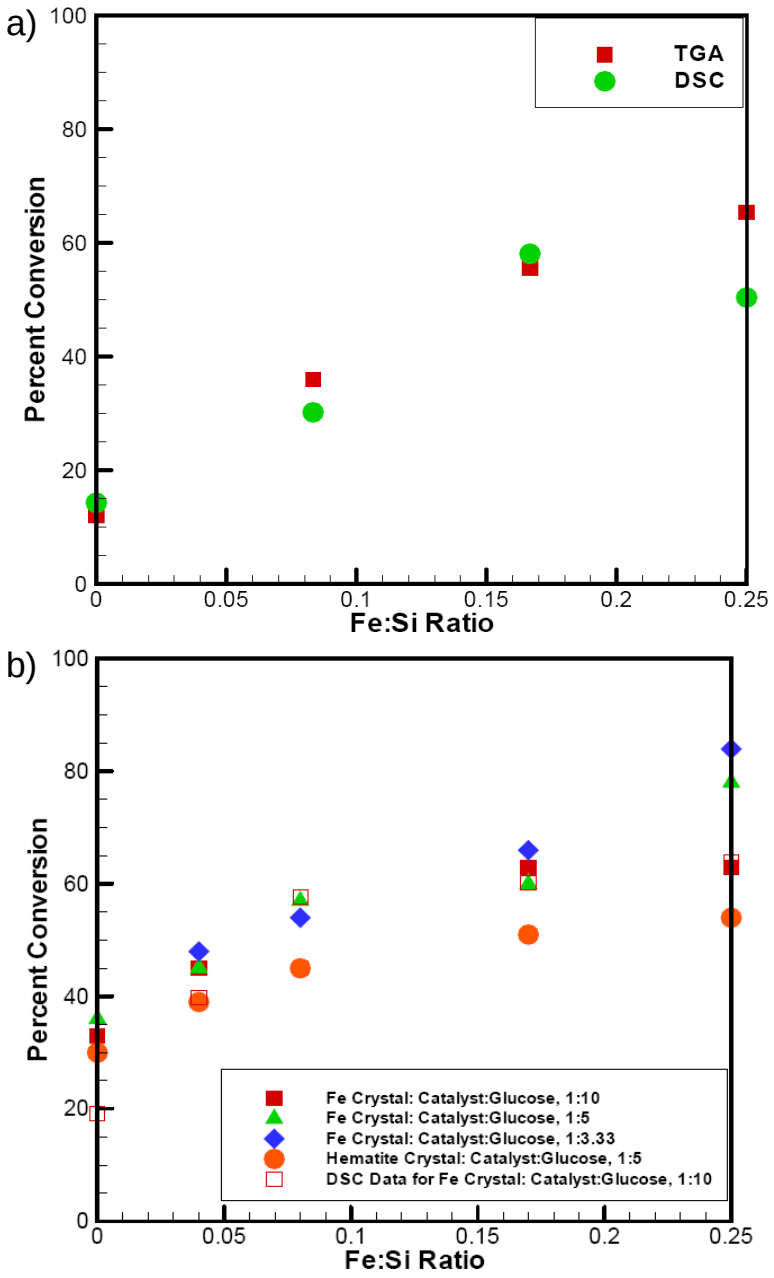

Figure 6. Alkaline hydrolysis of glucose using monoaxial silica nanofibers. a) Data calculated from DSC and TGA scans for catalyst: glucose ratio of 1:10 and various Fe: Si ratios. b) Bulk weight loss data for monoaxial silica nanofibers containing pure iron and hematite nanocrystals. Also included are the DSC result as open squares and the corresponding bulk weight loss method as closed squares for comparison confirming the accuracy of the bulk weight loss method.

For a maximum conversion of 85% with a very high loading of catalyst (a Fe: Si ratio of 1:4 and a catalyst: glucose ratio of 1:3.33), this method still leaves significant room for improvement. Therefore, coaxial electrospinning has been utilized to generate nanofibers with high load of iron nanocrystals in the skin layer. These nanofibers were then subjected to the same thermal treatment as the monoaxial nanofibers to produce pure iron crystals, since it was found that the reduced oxidation state displayed the best catalytic performance. Microtomed samples were then viewed under TEM, with representative images displayed in Figure 7. Figure 7a displays a TEM image of a microtomed nanofiber with a shell Fe: Si ratio of 1:4, which volumetrically results in a nanofiber with an overall Fe: Si ratio of 1:10.5 when the silica core is factored in due to the core/shell flow rate ratio of 0.02/0.03 ml/min. It is observed that there is a noticeable difference in the iron concentration between the core and the shell due to the coaxial electrospinning method utilized, leading to the selective placement of iron near the fiber surface.

Figure 7b displays a TEM image of a microtomed nanofiber with a shell Fe: Si ratio of 1:3, which similarly results in an overall Fe: Si ratio of 1:6 due to the same core/shell flow rate analysis discussed above. From this Figure it appears that although there is noticeable presence of nanocrystals within the shell similar to in Figure 7a, there are also crystals located toward the interior of the shell layer and perhaps even moving into the core. The size variation of the crystals is potentially due to the diffusion of iron precursor into the silica core prior to crystallization. The possible influence of the difference in metal precursor concentrations on crystal size and dispersion is also currently being investigated in the Cellular Automata code discussed previously. Similar nanofibers with shell Fe: Si ratios of 1:4, 1:3, and 1:2.5 were used to generate various combinations of shell concentrations versus overall concentrations. In Figure 7c, statistical analysis of the crystal location

throughout the fiber diameter for various coaxial nanofibers further indicates that the iron crystals generated are tuned toward the surface of the nanofiber through the use of coaxial electrospinning (see Figure 3d for monoaxial cases).

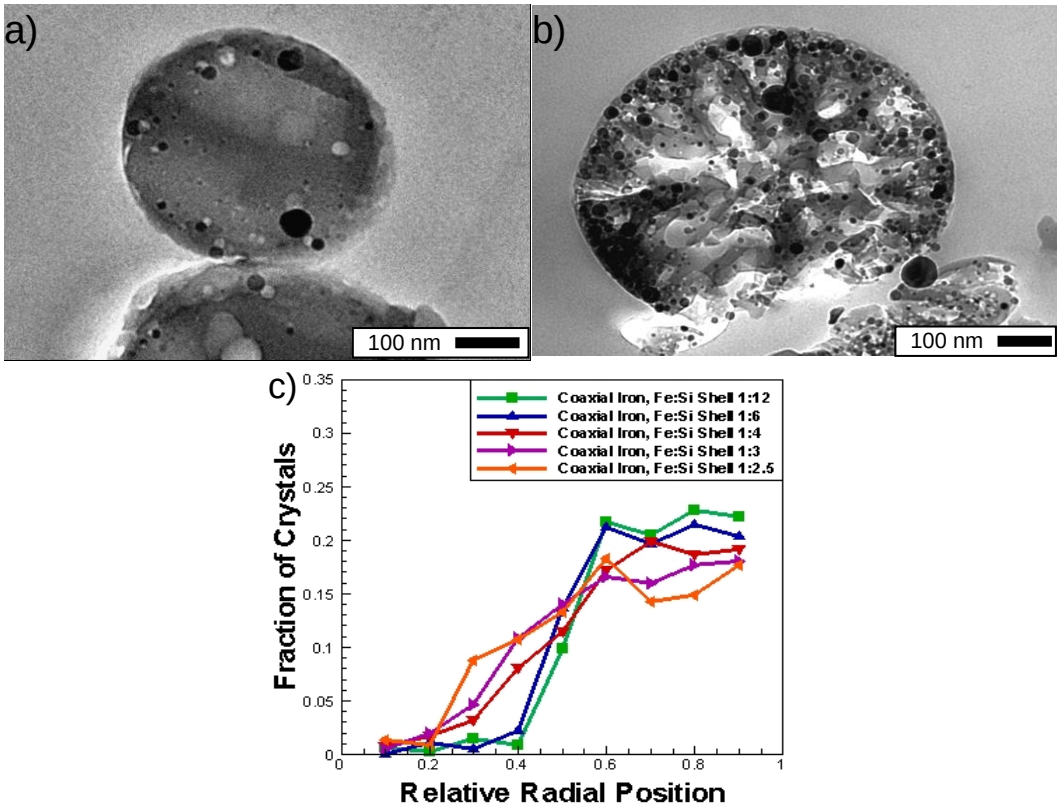

Figure 7. TEM images of microtomed coaxial silica nanofibers with highly loaded shells. a) Overall Fe: Si of 1:10.5 with a shell Fe: Si of 1:4, b) Overall Fe: Si of 1:6 with a shell Fe: Si of 1:3, and c) Statistical analysis of crystal location throughout the fiber diameter for various coaxial nanofibers confirming the substantial presence of iron crystals on the fiber surface.

These nanofibers were subsequently used in the alkaline hydrolysis of glucose in the same bulk weight loss manner previously utilized for the monoaxial nanofibers. The results of these experiments are presented, along with the results from the monoaxial case for comparison, in Figure 8. Figure 8a displays the percentage of conversion from glucose into fuel gas plotted versus the overall Fe: Si ratio throughout

the nanofiber. It is observed that coaxial nanofibers display a significant increase in catalytic efficiency of up to 30% versus monoaxial nanofibers at similar overall Fe: Si ratios. It is believed that this increase is due to the capability of tuning the location of the catalyst toward the surface of the nanofiber in coaxial nanofibers thereby making the more of the catalyst available for reaction. Support for this hypothesis is provided by Figure 8b. In this Figure the percent conversion of glucose to fuel gas is displayed against the concentration of metal within the theoretical shell region as calculated by the volume fraction afforded by the core/shell flow rates of solution in the initial electrospinning procedure. We note that this shell concentration is assumed to be the same as the overall concentration for monoaxial nanofibers whereas it corresponds to the concentration in the skin layer for coaxial nanofibers. It appears as though all of the data, both monoaxial and coaxial conversions, fall into a single trend within this Figure. Therefore, this indicates that it is primarily the catalyst located within the shell diameter that contributes to the catalytic efficiency, and placing iron species selectively in the skin layer via coaxial electrospinning gave rise to two to three fold reduction in catalytic consumption to maintain high conversion as compared to the monoaxial fibers with uniform distribution of catalysts.

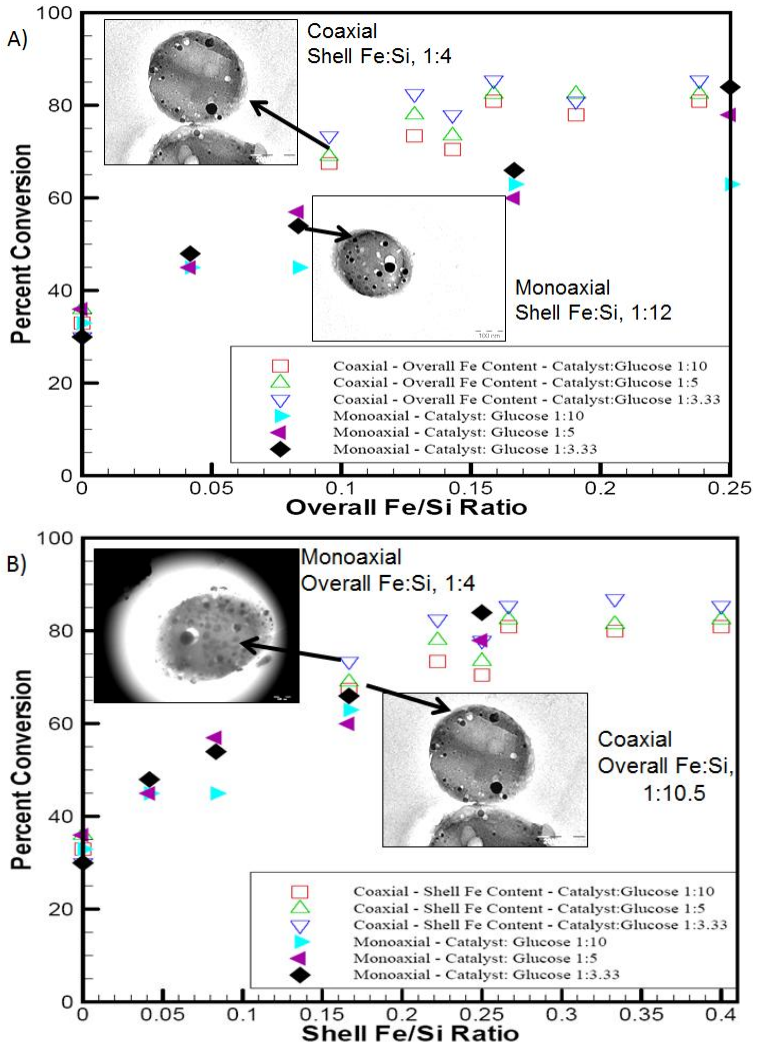

Figure 8. Alkaline hydrolysis of glucose using coaxial silica nanofibers containing highly loaded shells of pure iron nanocrystals. Also included is the monoaxial data presented in Figure 6 for comparison. a) The conversion of glucose to hydrogen vs. overall Fe: Si ratio throughout the nanofiber, and b) the conversion of glucose to hydrogen vs. shell concentration in both coaxial and monoaxial nanofibers. Inserts are TEM images of monoaxial and coaxial fibers with the same shell concentration, but different overall Fe: Si ratios.

It should also be noted that nanofiber-based iron catalysts in the current study exhibited a higher catalytic performance than the iron catalyst supported on a porous silica substrate, as summarized in Table 2. At the same catalyst loading, monoaxial nanofibers yielded about 85% conversion which is about 15% higher than the iron supported on silica. Furthermore, coaxial nanofibers with high loading of iron on the shear layer can yield the same conversion as monoaxial nanofibers with only one third of the catalyst loading. In addition, the Fe catalyst on the porous silica substrate yielded a very delayed onset of hydrogen production (the peak is more around 180ºC than the 130-150 ºC seen by the nanofiber catalysts in Fig.9) which generates a greater overlap with the CO_2 and methane production as well as a less pure hydrogen stream. We also note that a relatively low value of the maximum conversion, 70%, was obtained even with a very high loading of the iron catalyst supported on Al_2O_3 (2:5 ratio of catalyst to reactant) in the alkaline hydrolysis of cellulose.[48]

Fe Catalyst System	Fe:Si Ratio	Reactant	Catalyst/ Reactant Ratio	Total Conversion (wt. %)	H_2 in Product Gas (Mole %)
Monoaxial SiO_2 nanofibers with Fe	1:4	Glucose	1:3.33	85	> 96
SiO_2/SiO_2-Fe Coaxial nanofibers	1:6	Glucose	1:5	85	> 96
Fe catalyst in porous SiO_2 substrate	1:4	Glucose	1:3.33	69.5	88
Al_2O_3 substrate with Fe impregnation[48]	1:4	Cellulose	2:5	70	> 96

Table 2. Comparison of catalytic performance for fuel gas production via alkaline hydrolysis reaction

Finally, further thorough analyses on both solid and gas products were carried out to confirm the conversion of glucose into hydrogen gas and sodium carbonate

during the alkaline hydrolysis via the following reaction:

$$C_6H_{12}O_6 + 12NaOH \xrightarrow{cat.} 6Na_2CO_{3(s)} + 12H_{2(g)} \qquad (1)$$

First, quantification of the gaseous products was desired to confirm the production of hydrogen gas. RGA was used with a corresponding leak valve to allow low pressures of gasses into the apparatus, which allowed for the quantification of the gas stream using the mass spectrometer based on ionized species. This had the further advantage over the postmortem analysis of the collected gas via Gas Chromatography, or GC, to allow characterization of the gaseous products in near real time. As this reaction was performed under argon, the ionization of all gases was characterized. From the corresponding output pressures of each mass the volume percent could be calculated, and then with the known argon flow rate the corresponding flow rate ratio and thus molar flow rates could be calculated. These are displayed in Figure 9a, and 9b for monoaxial and coaxial nanofibers, respectively. Integrating this curve numerically then gave a close approximation to the total moles of each gaseous stream generated. The percent conversion based solely on the hydrogen moles produced is 67% for monoaxial nanofiber system, 81% for coaxial system. However, for more adequate comparison to the bulk weight loss method, the mass of all species released was calculated and subtracted from the original mass. According to this analysis, the conversions were 76%, and 84%, respectively. This falls much more in line with the bulk weight loss method analysis described previously. It should be noted that the product gas is composed of mostly H_2 (> 96 mole %) and CH_4 with very low concentrations of CO_2 and CO. More importantly, due to the clear separation of reaction temperature for H_2 and CH_4 productions, pure hydrogen can also be obtained under low temperature conditions. Further, the purity of the hydrogen gas produced at

various temperatures was determined and plotted in Figure 9c. It is clear that at low temperatures an almost pure stream of hydrogen is produced. In the monoaxial nanofiber case there is a pure hydrogen reaction with a slower decline to almost pure methane at moderate temperatures, which is perhaps due to the larger amount of reactants still present as a result of lower hydrogen production. In the coaxial case, a very sharp transition occurs where hydrogen goes from pure production to zero production showing that the selectivity and purity of the gaseous stream in the coaxial case is higher than that of the monoaxial case. Nonetheless, both have near pure hydrogen production at low temperatures.

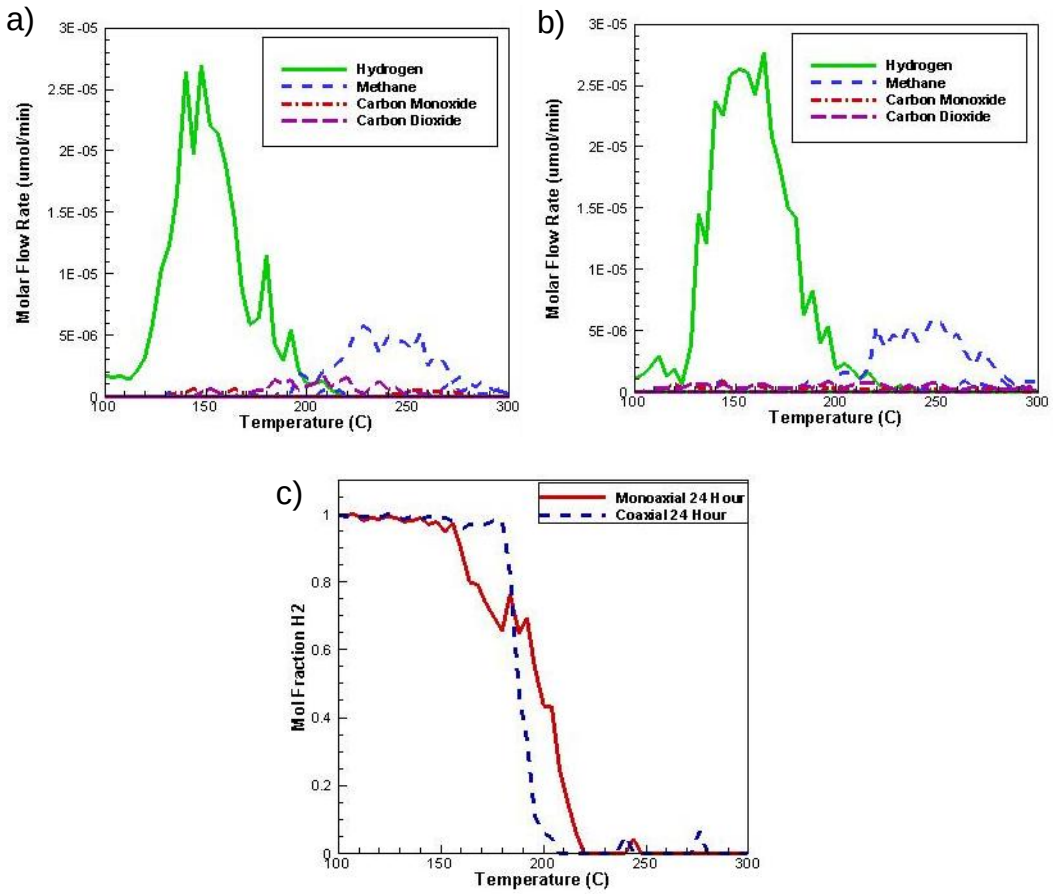

Figure 9. Product gas analysis through GC/RGA for (A) monoaxial nanofibers (Fe: Si = 1:4, catalyst: glucose = 1:3.33), (B) coaxial nanofibers (Fe: Si = 1:5, catalyst: glucose = 1:3.33), and (C) molar fraction of H_2 over reaction temperature for monoaxial and coaxial nanofibers

We note that all the alkaline hydrolysis experiments via various routes (DSC, TGA and RGA) in the present study were done after drying the mixture of glucose, NaOH solution and catalyst at 100ºC for 24 hours in air to prevent a potential deactivation of the catalyst due to the presence of water. To understand the mechanism of catalyst deactivation, XRD analysis was performed on the solids after 1, 5, 10, 15, 20 and 24 hour drying times. Each pre-drying time before the reaction was further allowed to go through the reaction mechanism and the bulk weight loss analysis was carried out to characterize the extent of reaction. This analysis is presented in Figure

10a. As shown in the Figure, the percent conversion remains low until 20 or 24 hour drying time. XRD analysis on the mixture of reactants and catalyst after 1 hour and 5 hour drying times showed the formation of iron hydrates for both monoaxial and coaxial nanofibers. XRD analysis on the solids after various drying times is shown in Figure 10b. The mixture of reactants and catalyst showed the formation of iron hydrate after 1 hour and 5 hour drying times for both monoaxial and coaxial nanofibers. XRD analysis for drying times of 10 and 15 hours were flat line with no sharp crystal signatures, indicating the presence of minimal iron catalyst crystals and formation of amorphous iron oxide hydrates such as $Fe(OH)_3$, as discussed in the FTIR results, Fig. 10c below. However, after 20 hours of drying time of the mixture of reactants and catalyst, austenite peaks returned under XRD for both monoaxial and coaxial nanofibers, which seems to result in much higher conversion. It is hypothesized that water and sodium hydroxide potentially absorbed by the silica substrate may generate hydrates and/or iron hydroxide which would limit the efficiency of these catalysts.

Further understanding of the actual deactivation mechanism was found through analyzing the samples under FTIR. Analysis was performed on the nanofiber catalysts prior to treatment with NaOH (Starting), after 1 hour drying time with NaOH and after 24 hour drying time with NaOH as shown in Figure 10c. Prior to treatment with sodium hydroxide, it appears that there is no indication of the presence of the hydroxide group (-OH) or water in the catalyst. However, following the treatment with NaOH solution and a short drying time it is apparent that there is a large amount of hydroxides by the broad curve between 3600 and 3000 cm^{-1} as well as the peak around 1650 cm^{-1} for the H-O-H bending mode from the hydrate form of either silica or iron, Fe-O-OH-H_2O (also known as $Fe(OH)_3$).[71, 72] The broad peak below 900 cm^{-1} for the 1 hour pre-drying sample may account for Fe-OH peaks (895 cm^{-1} and

798 cm^{-1} for Fe-O-H bending, 624 cm-1 for Fe-O stretching vibration).[73] The final curve after 24 hour drying details the regeneration of the catalyst and loss of hydrates and water, signified by the disappearance of the peaks at 3600 and 1650 cm^{-1}.

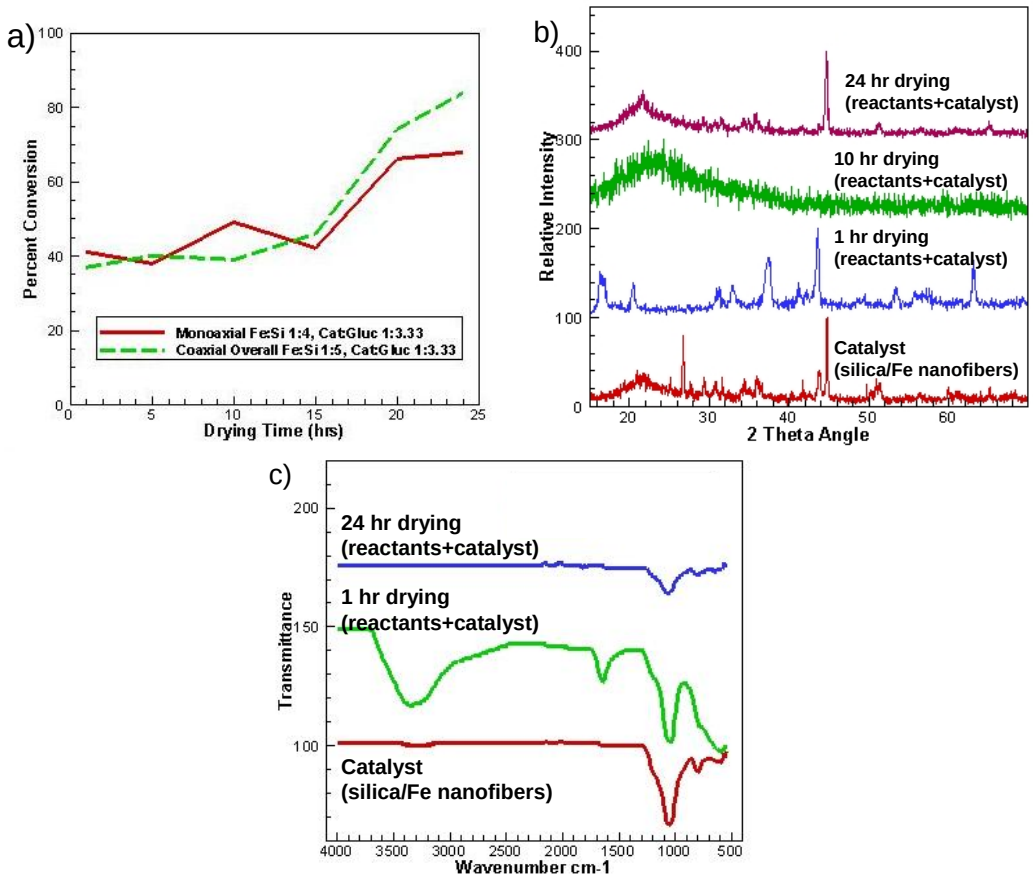

Figure 10. Effect of drying time of the reactant/catalyst mixtures on a) catalytic performance of monoaxial and coaxial nanofiber systems, b) XRD pattern and c) the FTIR spectra.

Finally, this issue associated with the catalyst deactivation at short pre-drying time was also confirmed by the quantification of the solid products after the reaction. NMR was performed on solid products produced by the alkaline hydrolysis reaction after a short (1 hour) as well as those produced after a long (24 hour) pre-drying time using the high catalyst: glucose ratio of 1:3.33 and silica nanofibers containing Fe: Si

ratios of 1:4, and the results are compared in Figure 11. A low concentration of acetone was added and used as a marker to confirm the location of the sodium carbonate for comparison and is also displayed. After allowing for only a 1 hour drying time, little sodium carbonate can be observed in the solid product through NMR, and the solid product appears charred, black, and brittle, possibly due to the thermal degradation of glucose. However, NMR results conducted on the solids residue from the reaction after 24 hour dry time exhibits strong sodium carbonate concentration confirming that with long drying times of the mixture of reactants and catalyst, glucose was converted into sodium carbonate while the hydrogen gas was produced via the alkaline hydrolysis reaction, Eq. (1). Calculating the conversion using the bulk weight loss method, the 1 hour dry time converted 41% to hydrogen while the 24 hour sample converted 77%.

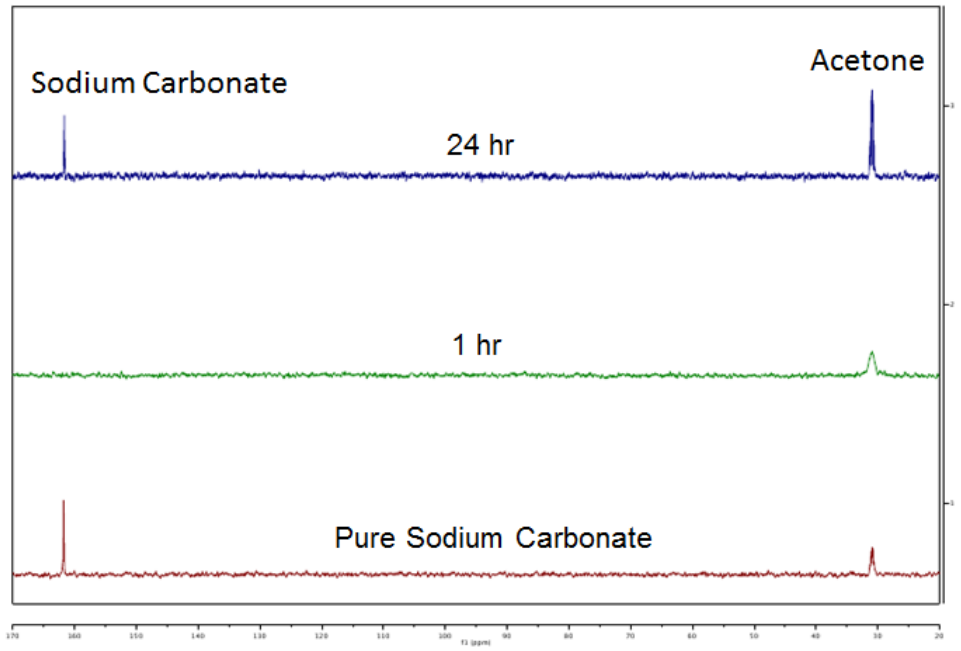

Figure 11. Analysis of solid products through NMR confirming the production of sodium carbonate for nanofibers with long pre-drying time

4. Conclusions

Monoaxial silica nanofibers from a sol-gel reaction have been successfully electrospun with various iron nitrate concentrations, and the characteristics of iron and nickel species in silica nanofibers have been analyzed via XRD, TEM and XPS. Through high temperature thermal treatment in 94% argon and 6% H_2, crystals of ferrite and austenite are formed from iron nitrate. Secondary thermal treatment of fibers containing pure iron crystals in stagnant air converts the iron crystal into hematite crystal. Fibers consisting of pure iron and hematite nanocrystals have been tested as catalysts in the alkaline hydrolysis of glucose to produce fuel gas such as hydrogen and methane. These results show that the reduced, pure iron crystal is much more efficient at catalyzing the reaction than the oxidized counterpart. However, the fact that the bulk of the crystal is located within the interior of the fiber seems to present a mass transfer limitation to glucose accessing the catalyst causing a significant catalysts loading for high conversion. Therefore, coaxial electrospinning was utilized to form nanofibers with highly loaded shells to limit the mass transfer problem. This method of tuning the crystal location allowed for a 30% increase in efficiency for fibers with the same overall Fe: Si ratio. NMR, GC/RGA, and bulk weight loss method through pre-drying time analysis confirm that the solids residue is predominantly sodium carbonate, while the gaseous stream is greater than 96 mole% hydrogen with ultra-high selectivity at low temperatures. This demonstrates that electrospinning, when combined with the exciting possibilities presented by sol-gel chemistry, creates a simple and inexpensive method for producing systems capable of catalyzing the reaction of glucose and perhaps cellulose to form CO and CO_2 free gas.

CHAPTER 3

SILICA NANOFIBERS WITH DISCRETE NICKEL NANOCATALYSTS AND THEIR USE IN THE HYDROGEN PRODUCTION VIA ALKALINE HYDROLYSIS OF GLUCOSE

1. Introduction

Recently, significant attention has been focused on catalysis by nanoscale materials and the increased number of active catalytic sites per unit mass resulting from the increased surface area to volume ratio of nanomaterials. Nanoparticles have been used to catalyze many reactions,[74, 75] but performance has been limited by the tendency of nanoparticles to aggregate.[76] To maintain the high surface area to volume ratio and catalyst accessibility while preventing nanoparticle aggregation, supporting the nanocatalysts in/on various substrates has been investigated. It is desired that these supports maintain the high surface area to volume ratio to allow the catalyst to be accessed while still preventing the aggregation of catalyst particles. One such support that has been recently used is electrospun silica nanofibers [40] due to the high aspect ratio of one dimensional materials, the ease of fabrication [77] and inexpensive nature of electrospinning,[28] as well as the high thermal stability, chemical resistance,[39] and low cost afforded by silica. Many reactions have been catalyzed using nanofibers,[78] but one reaction in particular that has garnered attention lately that electrospun nanofibers could influence is treatment of biomass.

There are a wide variety of thermochemical methods for converting biomass feedstock to usable energy sources. Combustion is the most rudimentary of these methods where high solids content biomass is burned in air directly to generate heat from chemical energy. However, the conversion to heat rather than a more easily

storable energy form as well as the high solids content prior to burning are major drawbacks for this system.[79] Another more promising method for biofuel treatment is through gasification, where organic products are heated and partially oxidized in the attempt to form high concentrations of syn-gas or methane gas by controlling a set of reactions between carbon, hydrogen and oxygen by controlling temperature and oxygen concentrations.[80] These reactions are further tuned by using metal oxide catalysts, but even with high catalytic efficiencies they fail to generate the cost effective means to produce highly pure streams of hydrogen gas at low temperatures.[81] Perhaps the most widely used method for biomass conversion, however, is pyrolysis. Pyrolysis is a method by which biomass is thermally degraded in the absence of air to produce liquid fuels as opposed to the gaseous products from gasification. This method has been thoroughly tested with a variety of heating rates and catalyst compositions and morphologies and shown to produce high concentrations of alcohols and other fuels. However, the even with high solids contents the heating requirements of the solution require such high energy that the amount of energy produced is only marginally greater than the energy expended to generate the liquid products. Further, the relative lack of selectivity in the liquid products generated currently does not allow for the direct use in generation of fuels. A relatively unstudied method for generating a usable fuel source from biomass is the alkaline hydrothermal treatment.[57] This method has been studied [48] and shown to produce near pure streams of hydrogen gas from cellulosic biomass at lower temperatures, with the onset of methane at higher temperatures. This is a particularly exciting method of thermal treatment due to the lack of tar produced, the generation of a near pure stream of usable fuel gas, and the generation of a usable solids byproduct of sodium carbonate.

Previously, monoaxial and coaxial silica nanofibers have been electrospun

with iron nanocrystals and were subsequently used in catalyzing the alkaline hydrolysis of glucose.[40] In this study glucose was chosen because of the simplicity of the reaction mechanism and the knowledge that a substantial fraction of cellulose biomass degrades into its monomeric form before reacting into hydrogen and sodium carbonate. Therefore, understanding the reaction mechanism of glucose into hydrogen contributes significantly in understanding the reaction of cellulose into hydrogen. In this previous study, monoaxial nanofibers were generated with the catalyst distributed throughout the nanofiber diameter as well as coaxial nanofibers where the catalyst was tuned toward the surface. When comparing the monoaxial to coaxial nanofibers in the study, it was found that the use of coaxial nanofibers generated a maximum conversion of greater than 80% and allowed for the tuning of the catalyst at the surface of the nanofiber, thereby decreasing the potential mass transfer limitation of reactant reaching catalyst located at the interior of the nanofiber. This therefore increased the catalytic efficiency up to 20% for nanofibers with the same overall catalytic loading or reducing the catalytic requirement by 3 fold to maintain the same catalytic efficiency.

However, a high ratio of the iron/silica nanofiber catalyst to glucose (1:3 to 1:5) was still needed to maintain a high conversion. Nickel has been shown to be a significantly more efficient catalyst than iron while maintaining the cost effective nature and potential magnetic recycle process of this catalyst.[57] It has also been shown that nickel catalysis of cellulosic biomass produces hydrogen at low temperatures with methane production occurring at slightly more elevated temperatures.[48] To this end, here we report on monoaxial electrospun silica nanofibers containing nickel nitrate for in-situ crystallization and their subsequent use in catalyzing the alkaline hydrolysis of glucose. Further, the reaction conditions including the heating rate and/or reaction temperature were varied to investigate reaction kinetics with nickel nanofiber catalysts to optimize the conversion and

selectivity of hydrogen production. The magnetic extraction and reusability of these nanofibers were also analyzed with regeneration tested after the performance began to decrease. Finally, coaxial electrospinning has been used to detail the tuning of the catalyst toward the surface of the nanofiber showing a decrease in mass transfer limitations. However, this tuning of the catalyst toward the surface is also shown to greatly increase the selectivity of hydrogen produced as well as an increase in the temperature range at which near pure hydrogen is produced. This implies that not only the reaction conditions but also the concentration and geometry of the catalyst plays a large role in the production of hydrogen gas from glucose through the alkaline hydrolysis of glucose.

2. Experimental Methods

Electrospun nanofibers were prepared using sol-gel chemistry. Silica precursor solutions of TEOS: EtOH: H2O: HCl (Sigma Aldrich) of 1:2:2:0.1 were generated with varying concentrations of nickel nitrate (Sigma Aldrich). The resulting solution is heated to 50℃ until gelation produces the proper viscosity. Monoaxial nanofiber samples are created by electrospinning using a Harvard Apparatus PHD 2000 Infusion syringe pump flowing at 0.03 ml/min through a 22 gauge Hamilton N722 needle where it is met by an electric field generated a 15 cm needle to plate distance and a 20 kV electric charge supplied by an HV ES3OP-5W Power Supply. Coaxial nanofiber samples were generated using the same equipment and the same electric field, but with an inner syringe of 24 gauge and an outer syringe of 18 gauge with either a 0.03/0.02 or 0.02/0.03 ml/min core/shell flow rate ratio.

Following sample generation, the samples are placed in a Mullen Two Zone 1700ºC Tube Furnace for high temperature thermal treatment. In producing reduced nickel crystals, forming gas (94% argon and 6% hydrogen) was fed through the tube

furnace at a flow rate of 0.8 cc/sec. The fibers were heated at 5ºC/min to 800ºC held for 5 hours, and then cooled at 5ºC/min back to room temperature. Nickel oxide nanocrystals were formed by flowing 100% Ar through the same tube furnace at 0.8 cc/sec. These fibers were heated at 5ºC/min to 800ºC held for 5 hours, and then cooled at 5ºC/min back to room temperature. The samples are characterized through XRD using a Scintag Theta-Theta X-ray Diffractometer and TEM using an FEI Tecnai G2 T12 Spirit TEM STEM. To generate TEM cross section images the samples were first placed in an epoxy resin for 8 hours and then 70 nm cross sections were cut using a Leica Ultracut UCT Cryo-Ultramicrotome and a DiATOME diamond knife. The bulk phase weight loss data was conducted on ceramic discs in the same 2 zone tube furnace discussed previously.

Mats of silica nanofibers containing nickel or nickel oxide nanocrystals were tweezed apart into centimeter long sections. These samples were then added to 0.5g of d-glucose (Sigma Aldrich) and physically mixed. 2.35g of 50 wt. % NaOH solution at 100ºC was then added to the solution. Bulk weight loss data was found by treating the solution at 100ºC for 24 hours in Argon to release entrained water. The sample was then heat treated under argon at 10ºC/min to 100ºC, followed by thermal treatment at 2ºC/min from 100ºC to 300ºC and then cooling at 5ºC/min to room temperature. From the weight difference due to thermal treatment, the percent conversion was calculated. Further analysis of the gas produced was conducted via mass spectroscopy using a Vulcan 3 130 Box Furnace connected to a low pressure leak valve which then fed the gas into an Extorr XT200 Residual Gas Analyzer following the same thermal treatments and dry times listed in the bulk weight loss experimental setup. This RGA setup operates similar to a rugged Mass Spectrometer and generates data in real time by ionizing the gas stream fed into it and outputting the relative partial pressure of each mass component within the stream. By analysis of the

partial pressures and the known flow rate of argon, the flow rate and thus the molar composition of the stream can be analyzed. Known gas compositions as purchased were tested in this method and found to have an acceptable error rate per data point of < 3.1%.

3. Results & Discussion

Monoaxial nanofibers were fabricated using sol-gel chemistry using tetraethyl orthosilicate (TEOS), ethanol (EtOH), water (H_2O) and hydrochloric acid (HCl) as precursor to silica in a 1:2:2:0.01 molar ratio and various concentrations of nickel nitrate [$Ni(NO_3)_2$] as a precursor to metal or metal oxide nanocrystals. Coaxial nanofibers were fabricated using a concentric ring spinneret with a pure silica core solution and a silica solution with nickel precursors as the shell. Representative SEM images for both monoaxial and coaxial nanofibers are displayed in **Figure 12**. The average diameter ranged 200-500 nm, and 300-700 nm for as-spun monoaxial and coaxial nanofibers, respectively.

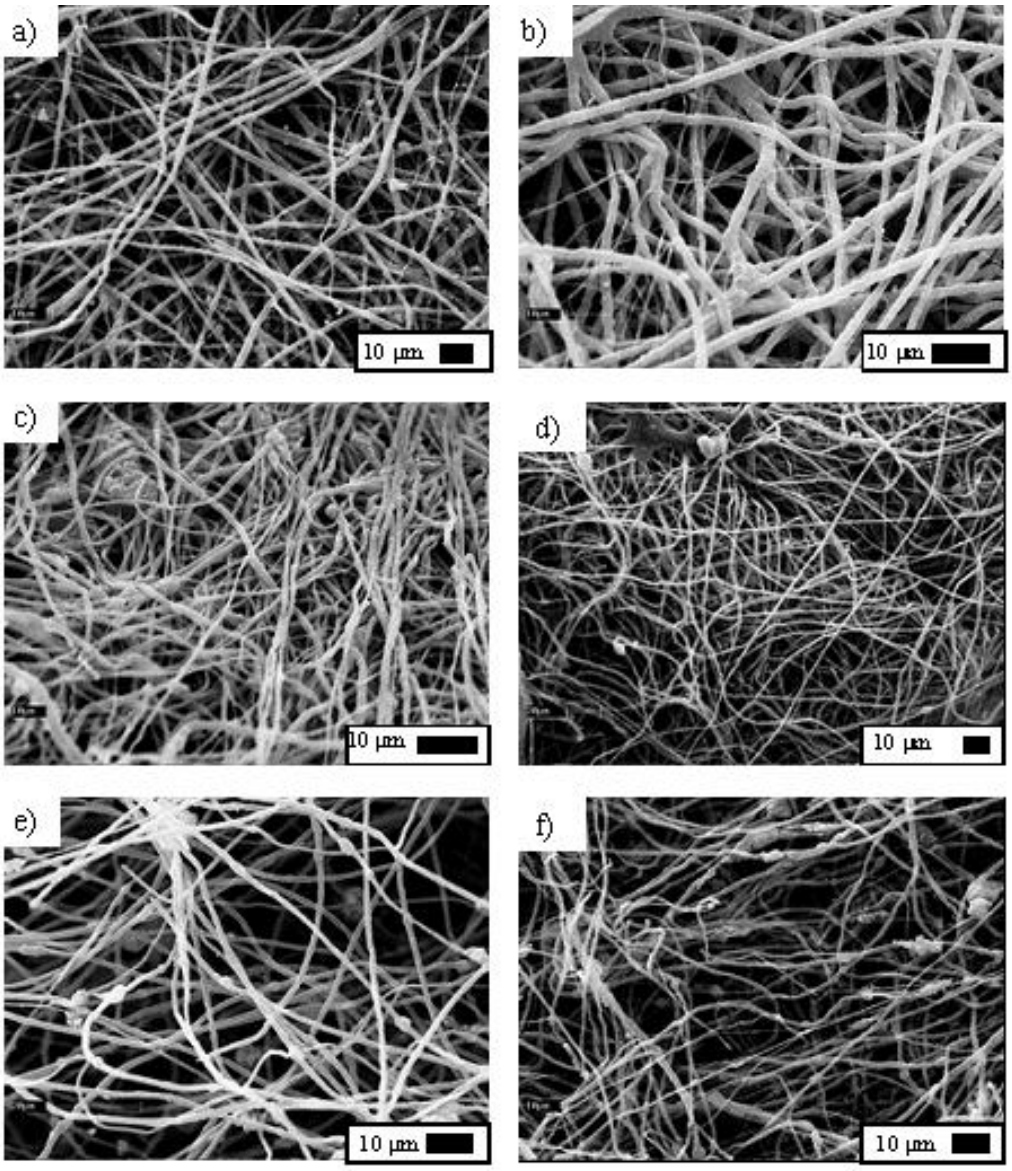

Figure 12. Representative SEM images of as-spun monoaxial nanofibers with Ni: Si atomic ratios of (a) 1:12, (b) 1:6, (c) 1:4, and coaxial nanofibers with shell Ni: Si ratios of (d) 1:6, (e) 1:4, and (f) 1:2.5.

Collected as-spun fibers were heated to 800ºC for 5 hours under forming gas (94% argon 6% H_2) to generate a reduced nickel metal crystal or under pure argon to produce an oxidized nickel oxide crystal. Nickel oxide nanocrystals are created similarly using the same thermal treatment under stagnant air. The XRD and TEM

results after reducing thermal treatment are presented in **Figure 13**. Figure 13a presents the XRD pattern for silica nanofibers reduced under forming gas with diffraction peaks at 42º and 52º corresponding to those of face-centered cubic nickel crystal. These nanofibers were then mounted in epoxy resin and microtomed to be imaged under TEM. Figures 13b,13c, and 13d present TEM images of monoaxial silica nanofibers containing nickel crystals with Ni: Si ratios of 1:12, 1:6, and 1:4, respectively, and Figure 13e displays the statistical analysis of the crystal location within the nanofiber diameter for monoaxial nanofibers. It is apparent from these images as well as the statistical analysis that the location of the majority of the nickel crystal is toward the interior of the nanofiber.

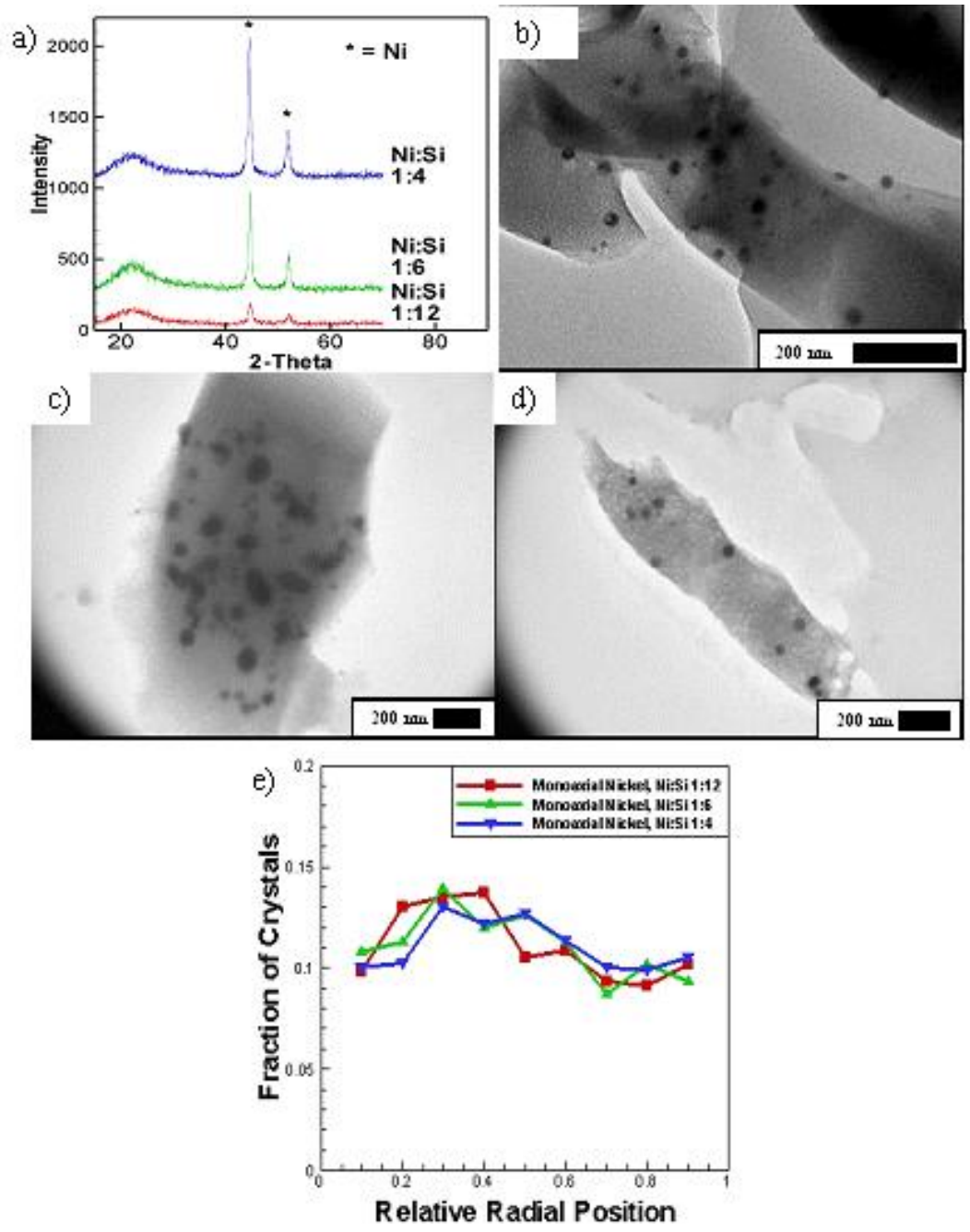

Figure 13. Monoaxial silica nanofibers with nickel nanocrystals. (a) XRD pattern demonstrating nickel peaks for three Ni: Si atomic ratios. TEM images of microtomed monoaxial nanofibers with nickel nanocrystals with Ni: Si ratios of (b) 1:12, (c) 1:6, and (d) 1:4 as well as the (e) statistical analysis graph of the relative location of the nickel crystal within the diameter of the nanofiber.

Meanwhile, **Figure 14** presents microtomed TEM images of coaxially produced nanofibers. Figure 14a displays the coaxial case having an overall Ni: Si

ratio of 1:12 and a shell Ni: Si of 1:4 with a clear indication of a core shell boundary, while Figure 14b displays an Ni: Si of 1:2.5 and an overall Ni: Si of 1:6 but a smeared core shell boundary potentially due to the diffusion of nickel precursor during the coaxial electrospinning process. Figure 14c displays a statistical analysis of the crystal location similar to the graph presented in Figure 13e. Through these figures and analyses it is seen that coaxial electrospinning can tune the crystal location toward the surface of the nanofiber., which has particular relevance in catalytic applications, such as the alkaline hydrolysis of glucose, to reduce the potential mass transfer limitation for the reactant to reach catalyst crystals located near the core of the nanofiber.

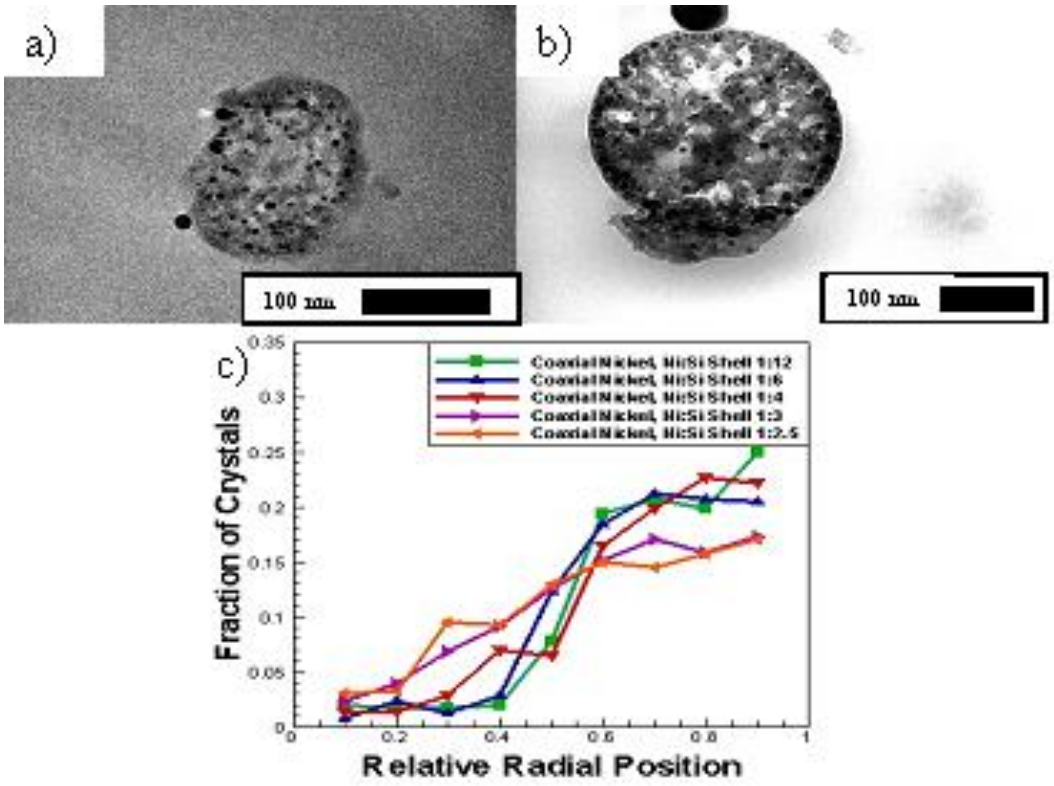

Figure 14: Representative microtomed coaxial silica nanofibers containing nickel nanocrystals with (a) low concentration (overall Ni: Si of 1:12, shell of 1:4) and (b) high concentration (overall Ni: Si of 1:6 and shell of 1:3). (c) The fraction of crystals located within the nanofiber diameter is presented versus the relative radial position where they were observed for various coaxial samples tested detailing the statistical observation of tuning the crystal toward the surface of the nanofiber.

Monoaxial nanofibers containing nickel and nickel oxide nanocrystals were then tested in the bulk weight loss method for alkaline hydrolysis of glucose. The conversion obtained from the bulk weight loss in a tube furnace has shown to be in good agreement with those measured from the heat of reaction during differential scanning calorimetry (DSC) and weight loss during the thermogravimetric analysis (TGA) experiments.[40] It is further tested and confirmed in both purity and conversion by residual gas analysis (RGA) later. The data corresponding to the percent conversion versus the amount of catalyst used in the system for monoaxial nanofibers is shown in **Figure 15**. The catalyst loading in the experiment was varied either by changing the ratio of nanofiber catalyst to glucose (1:10, 1:5 and 1:3.33) and that of nickel to silica in the nanofibers (Ni: Si 1:12, 1:6, 1:4) for both oxidized (nickel oxide) and reduced (nickel) crystals. It is observed that through the inclusion these catalytic nanofibers, the conversion increases from 30% without catalyst to a maximum of 92% with high catalyst: glucose ratio and the Ni: Si ratio. Nickel oxide nanocrystals, however, have a greatly reduced catalytic effect as the conversion hovers around 30-40% and shows little correlation with the amount of nickel oxide present. Comparing the previously reported silica nanofibers with iron nanocrystals to the current study, the results show that the maximum conversion for nickel (92%) significantly outperforms that of iron (82%) with the same catalyst loading.

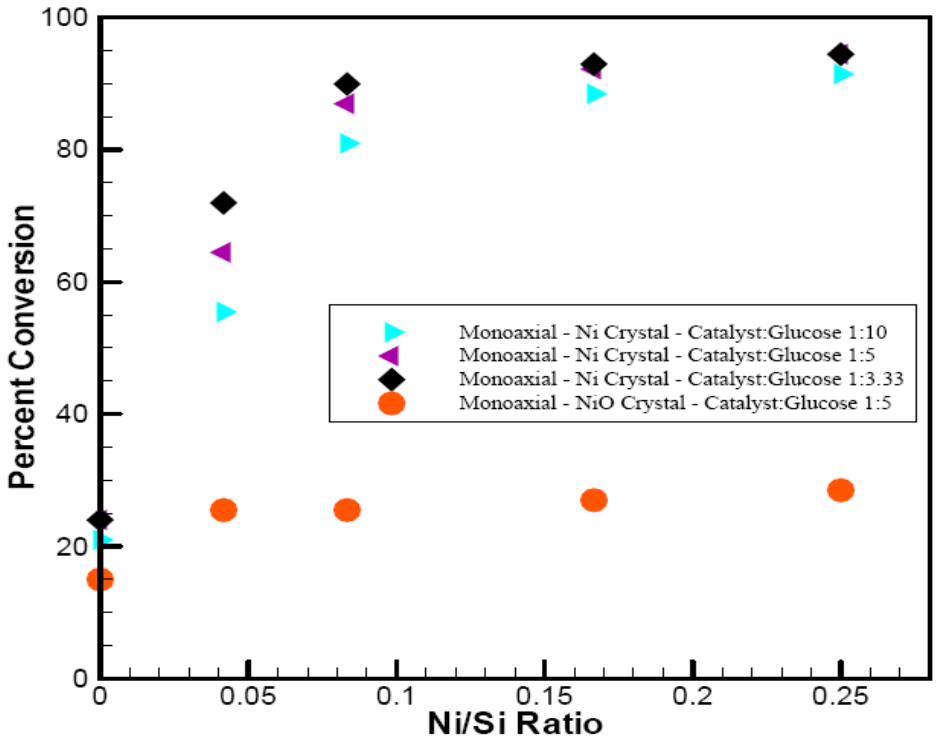

Figure 15. Alkaline Hydrolysis of Glucose. Bulk weight loss method displays increase in loading increases conversion and that reduced nickel is significantly more efficient than nickel oxide.

Further analysis of the reaction was desired to both confirm the purity of the hydrogen production as well as to tune the conversion and products. As discussed previously, it is desired to understand if glucose has the same reaction profile as cellulosic biomass reacted across embedded nickel catalysts where hydrogen is produced at low temperature followed by a production of methane at high temperatures.[40] In this effort as shown in **Figure 16**, the heating rate was fluctuated and subsequently a constant temperature was used to separate production of hydrogen from other byproducts with Figures 16a, 16b, and 16c, representing the data for heating rates of 1ºC/min, 2ºC/min and 5ºC/min, respectively concluding with Figure 16d presenting the data for the mole fraction of hydrogen in the gaseous stream versus temperature for each heating rate tested. A table of the conversions for each thermal

treatment method is also summarized in **Table 3**. The hydrogen conversion is calculated via two ways. First, the ratio of molar quantities of hydrogen produced to the theoretical maximum, and second the overall conversion is also calculated by determining the mass of the gasses released and then calculating the moles of hydrogen that would represent. The overall conversion is used to determine the validity of the bulk weight loss method and to give an additional relative purity of the gaseous stream produced.

Heating Conditions	Molar Hydrogen Conversion	Bulk Weight Loss Conversion
1ºC/min to 300ºC	90%	92%
2ºC/min to 300ºC	88%	94%
5ºC/min to 300ºC	81%	90%
Step to 100ºC	6%	11%
Step to 130ºC	79%	81%
Step to 150ºC	89%	91%
Step to 170ºC	67%	88%
Step to 210ºC	46%	84%

Table 3. Analysis of the Thermal Treatment Conditions and their effect of the conversion based on the moles of hydrogen produced versus the theoretical maximum due to the glucose added to the system as well as an equivalent bulk weight loss calculation to confirm the validity of this method under benign heating conditions.

The analysis of RGA data presented in Figure 16 leads to a few key observations. First, as the heating rate is increased, there is a clear spreading of the hydrogen production over a wider range of temperatures. It is thought that this is due to reaction limitation and thus with a faster heating rate more side reactions are thermally enabled and thus byproducts are formed rather due to the increase in reactant concentration remaining at higher temperatures. The decrease in hydrogen selectivity with increasing heating rate in the highest heating rate case (Figure 16d) would tend to support the second explanation. Further, it is apparent from the slow heating rate that hydrogen can be selectively generated from glucose with minimal

side products especially at low temperatures. Between 130 and 160 ºC, the selectivity of hydrogen is near pure suggesting that perhaps holding the temperature at this temperature would produce pure hydrogen without allowing side reactions to occur. Thus, from this analysis it was deemed that perhaps moving to a constant reaction temperature could increase selectivity while also producing hydrogen at an increased rate.

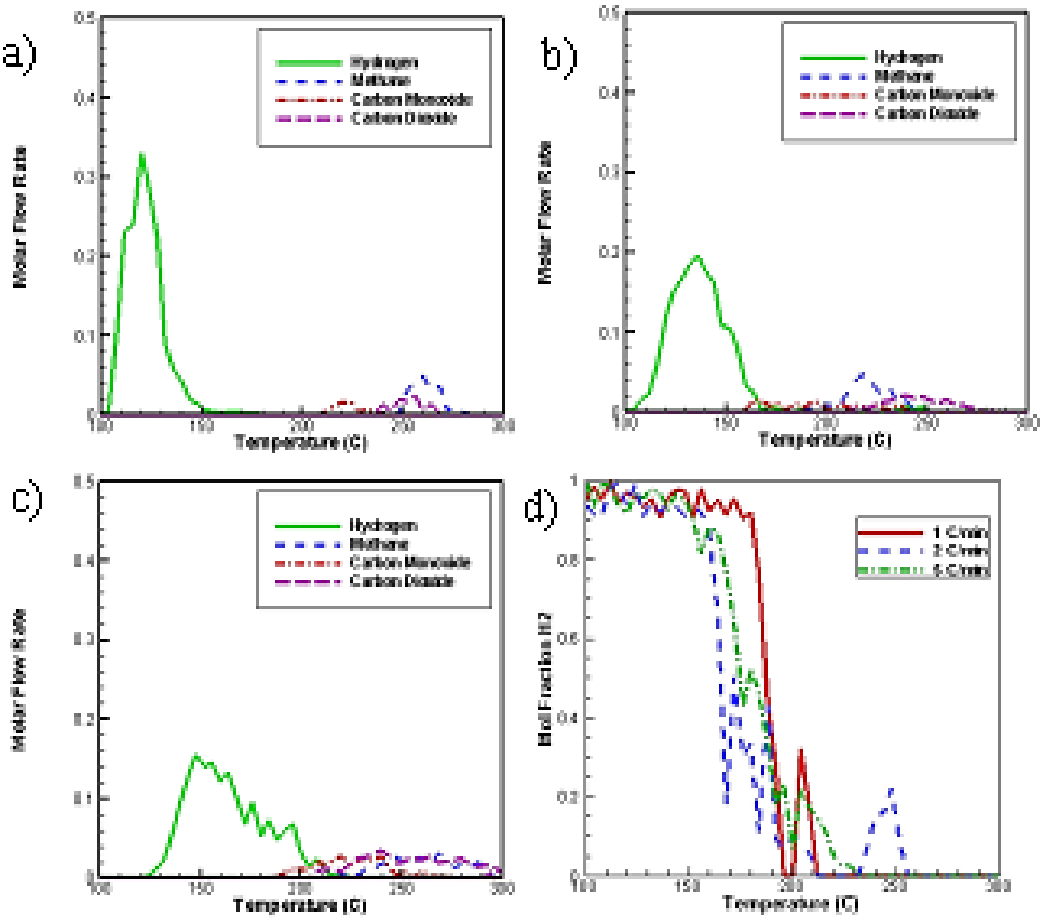

Figure 16. RGA analysis of gaseous products from glucose reacting across monoaxial silica nanofibers with a Ni: Si ratio of 1:4 and a catalyst: glucose ratio of 1:3.33 for various heating methods where first the heating rate was fluctuated from (b) 1, (c) 2, and (d) 5 ºC/min. (e) The overall mole fraction of hydrogen in the gaseous stream is displayed for all three heating rates.

Five temperatures were selected from the slow heating rate graph to test. **Figure 17** further presents the results for the constant reaction temperature tests with Figures 17a, b, c, d, and e displaying the graphs of fuel gas production for 100ºC, 130ºC, 150ºC, 170ºC, and 210ºC, respectively again concluding with Figure 17f presenting the mole fraction of hydrogen in the gaseous stream versus time for each temperature tested. As can be seen by these Figures the selectivity and the conversion increases from near zero at 100ºC to moderate conversion and high selectivity at 130ºC and finally to very high conversions with high selectivity at 150ºC. However, this still requires a significant time to conclude the production of hydrogen (~200 min), so higher temperatures also were chosen, but these temperatures decreased the selectivity considerably, as can be seen by Figure 17d and 17e. At these elevated temperatures, glucose may be thermally degrading enabling side reactions which increases concentrations of methane and carbon dioxide. It should be noted that there was still a relatively low concentration of carbon monoxide present at this temperature. These trends can also be seen in Table 1 where the conversion based on hydrogen and the bulk weight loss conversion are presented numerically as evidence of hydrogen production and selectivity of hydrogen. This analysis shows that by tuning the final temperature (< 170ºC) or the heating rate (< 5ºC/min); nearly pure hydrogen can be selectively generated with minimal side reactions allowed. Yet, at increased temperatures it seems that the reaction rate of the byproducts overtakes the production of hydrogen – or at least comes to a point where it rivals the production of hydrogen. Hence, an analysis of the concentration of products produced was used to back calculate reaction rate coefficients to analyze optimal temperatures to operate this reaction.

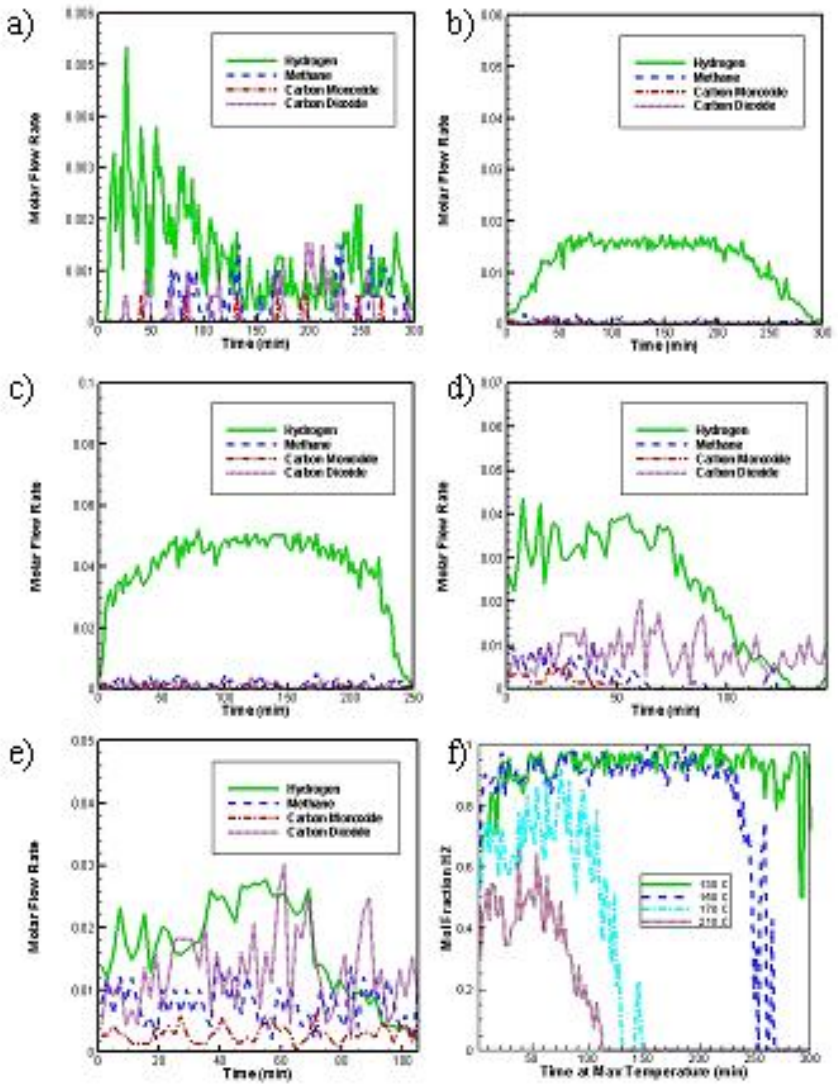

Figure 17. RGA analysis of gaseous products from glucose reacting across monoaxial silica nanofibers with a Ni: Si ratio of 1:4 and a catalyst: glucose ratio of 1:3.33 for various maximum temperatures of (a) 100 (b) 130 (c) 150 (d) 170, and (e) 210 ºC. (f) The mole fraction of hydrogen in the gaseous stream is displayed for 130, 150, 170 and 210ºC with 100ºC omitted due to the overall low concentration of products at that temperature.

Using the data presented at early times in Figure 17b, c and d, the reaction rate constant for each product at each temperature was calculated and are presented versus their corresponding temperature in **Figure 18**. The hydrogen reaction was found to be

second order while the rest of the reactions were found to be first order indicating they depended strictly on the glucose concentration and thus are hypothesized to be thermal degradation reaction mechanisms. As can be seen, at low temperature (130ºC) the rate constant for hydrogen production is ~2 orders of magnitude greater than that for any of the other side reactions which leads to the high selectivity at this temperature previously seen. At moderate temperatures (150ºC) the rate constant for hydrogen production increases slightly and is still significantly greater than that of other side products, though carbon dioxide increases at a greater rate than hydrogen over this temperature increase. High temperatures (170ºC), however, display a more uniform distribution of reaction rate constants where the constant of carbon dioxide surpasses that of hydrogen, and those of methane and carbon monoxide are now the same order of magnitude as that of hydrogen. This confirms the conversions previously discovered at higher temperatures where the hydrogen selectivity decreased significantly. These reaction rate constants, which were calculated strictly on the onset of the reaction profile, were then used to attempt to predict the concentration profile to determine where the variance occurs.

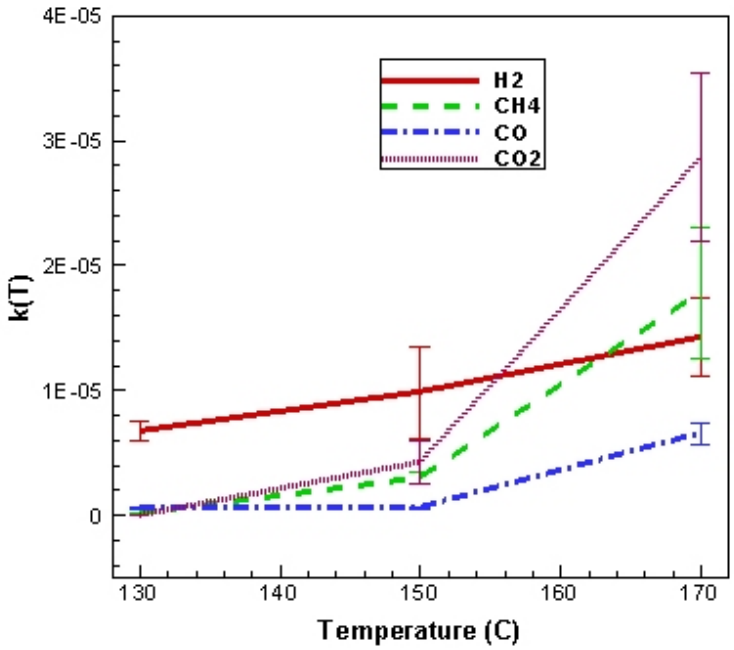

Figure 18. The data from maximum heating temperatures of 130, 150 and 170 ºC were used calculate reaction rate constants for each product at each temperature.

Figure 19 presents the predicted production of each product versus time as well as the actual data found. General observations from these figures are as follows. It is found that the production of products at 170ºC is faster than at other temperatures, but quickly declines in all cases except carbon dioxide. It is also seen that the byproduct reactions increase for both predicted and actual production as temperature increases. Finally, it is found that in all cases there is general agreement between actual and predicted values at early times as displayed in Figure 19. Figure 16a displays the hydrogen production for each temperature and clearly shows that low temperatures (130ºC and 150ºC) have very good agreement between the predicted values and actual values, but a large deviation is seen for 170ºC where byproducts are produced at higher concentrations. It follows that a relatively pure stream of hydrogen would be expected with the knowledge of the magnitude of the reaction constants and the agreement between prediction and actual values. Figure 19b, c, and d present

similar plots for the production of methane, carbon monoxide and carbon dioxide for both predicted and actual values at each temperature tested. These trends are similar to the hydrogen case except are calculated based on the corresponding first order rate constant calculated previously. However, in each case except for carbon dioxide the production deviates from the actual data heavily after about 50 min. This would seem to indicate that the concentration of reactant has decreased to the point of inhibiting reaction. Yet, at 170ºC carbon dioxide continues to increase over the time range tested; which may indicate that the thermal degradation potentially occurs in such a way that carbon dioxide is favorable to any other side reaction. Further, from these graphs it is also found that even at short times with high temperatures, there is minimal selectivity to produce hydrogen gas, and thus there are few degrees of freedom to manipulate at high temperatures to increase reaction rates while maintaining the hydrogen selectivity.

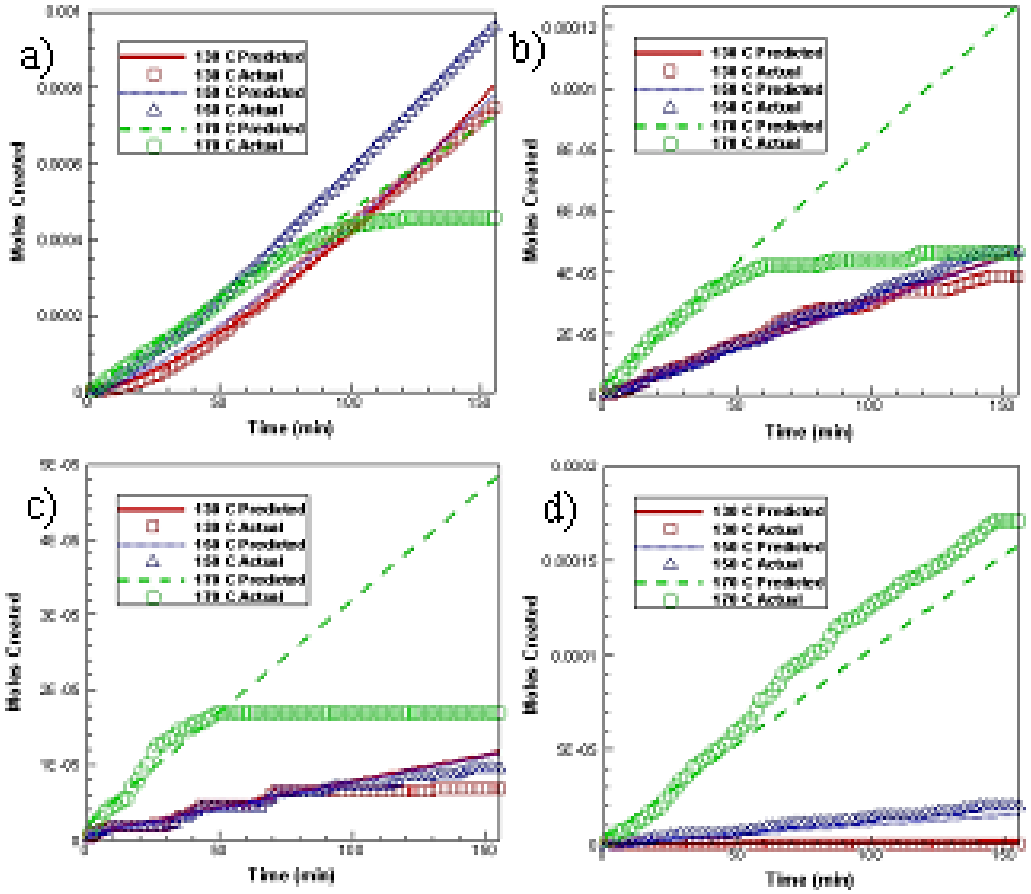

Figure 19. Time evolution of production of (a) hydrogen, (b) methane, (c) carbon monoxide and (d) carbon dioxide predicted by the calculated reaction rates versus the observed rate.

Recyclability, reusability and regeneration are also very important issues when discussing catalysts. Due to the magnetic activity of these catalyst systems a very simple recycle scheme with a magnet is used to gather the nanofibers following reactions. In this process the solids products after thermal treatment were mixed in an aqueous solution and agitated and then filtered. The catalyst was then recovered magnetically, and the mass of catalyst recovered was at least 97% of the mass of catalyst initially introduced to the system. This catalyst sample was then introduced to a new biomass solution and reacted under the same conditions as the first sample. This was repeated until the conversion, as tested by the bulk weight loss method,

showed significant decrease after 5 repetitions displayed in **Figure 20**. The conversions are presented in bar graph form in Figure 20a. TEM and XRD results of the nanofibers recovered from the solutions are also shown in the Figure. TEM analysis shows strong crystalline peaks after each of the first four reactions as displayed in Figures 20c - g. After the fifth reaction, however, there is significantly fewer catalyst crystals observed as shown in Figure 20h. This correlates well to the XRD analysis where the catalyst recovered after the first four reactions show strong diffraction peaks of nickel crystals until the fifth reaction when the strength of the nickel peak is significantly diminished as can be seen by the relative increase in the strength of the broad silica band at lower angles. Following the decrease in conversion, crystal intensity and number of crystals after the fifth reaction, the catalyst was taken for repeated thermal treatment under the same conditions as initial crystallization to form reduced nickel. This in turn produced high conversions as seen by run number 6 in Figure 20a, a similar number of catalytic sites observed under TEM as seen by Figure 20i, and a regenerated strong nickel peak in XRD together indicating that the nickel is still present in the nanofiber support and catalytically active after thermal treatment. The solids product has been analyzed through NMR, XRD, and FTIR and shown to be primarily sodium carbonate as expected with conversions above 80% for all tests.

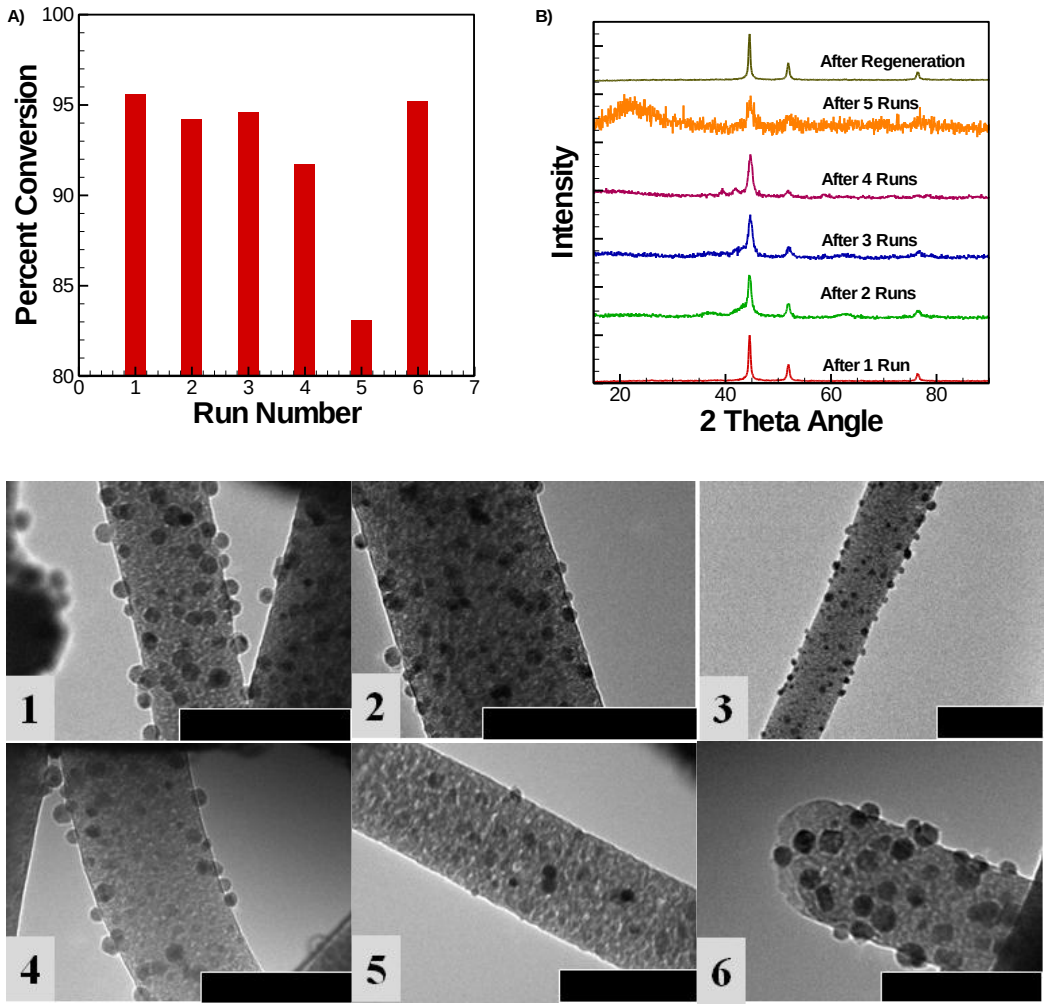

Figure 20. The recycle, reuse, and regeneration of these catalyst samples are tested. (a) The percent conversion as found by the bulk weight loss method for catalyst samples used, recycled, and reused in five successive experimental runs. Run number six represents a run after catalyst regeneration. (b) The catalyst samples are characterized in XRD after multiple runs. (1-6) TEM images of catalytic nanofibers following 1, 2, 3, 4 and 5 successive runs, respectively displaying a decrease in observable nickel catalyst domains as seen in XRD as well. (6) TEM image of catalytic nanofibers following repeated thermal treatment showing regeneration of observable nickel catalysts as can be seen in XRD and further is observed in conversion as well.

Beyond studying how different catalyst concentration within the nanofiber and engineering variables changed the catalytic performance, it was desired to understand how the nanofiber morphology versus other substrate geometries influenced the reaction performance. To this end, two bulk substrates were generated using previously defined procedures for treating cellulosic biomass.[48] In this study, different surface areas are afforded by the different substrates used and also differ after impregnation. However, while the surface area differs as reported according to the generation mechanism,[48, 57] the Si: Ni ratio and the Ni: glucose ratio are consistent throughout this study. The conversion, as tested by the bulk weight loss method, was tested for multiple runs after the catalyst was recovered using the same approach as for the nanofiber method. These results are presented along with the conversion found for monoaxial nanofibers in Figure 20a, are presented in **Table 4**. As can be seen the peak performance for these two respective geometries differ as the nanofiber case produces 92% conversion during the first run and the bulk support is significantly lower at 83%. Further, the decrease in performance begins after the first run for these supports and continues nearly linear to a final performance of 61% after five runs while the nanofiber case remains above 90% for four cases and only drops after the fifth run. Both cases, though, display great recovery and regeneration as they both produce very similar conversions as their initial use after a repeated thermal treatment.

Run Number	Monoaxial Silica Nanofibers	Fumed Silica	Cab-O-Sil
1	92%	81%	83%
2	90%	77%	78%
3	91%	70%	71%
4	90%	66%	67%
5	82%	61%	64%
Regeneration	91%	79%	83%

Table 4. The data is presented detailing the conversion found for monoaxial silica nanofibers containing nickel nanocrystals versus two different bulk silica samples impregnated with nickel nanocrystal catalyst previously used in cellulosic biomass conversions.[48] These samples are recycled and reused in multiple runs, and finally after decrease in conversion is observed they are regenerated through repeated thermal treatment as displayed above.

However, even with high selectivity afforded by these catalytic nanofibers, there was still a significant drawback due to the initial high catalytic loading requirement. It was hypothesized that this might be due to a potential mass transfer limitation inhibiting reactants from reaching the catalyst located within the nanofiber support. Therefore, the second order reaction rate constant was used to calculate the second kind of the Damkohler number for the monoaxial nanofiber system to analyze the effective diffusion time versus the effective reaction time. The dimensionless diffusion-reaction equation governing a second order reaction in a cylindrical nanofiber catalyst can be written as:

$$\frac{1}{\tilde{r}}\frac{d}{d\tilde{r}}\left(\tilde{r}\frac{d\tilde{c}}{d\tilde{r}}\right)-\mathrm{Da}_{\mathrm{II}}\tilde{c}^{2}=0 \tag{2}$$

where $\tilde{r}$ and $\tilde{c}$ are the dimensionless radial coordinate and the dimensionless concentration of glucose, respectively. $\mathrm{Da}_{\mathrm{II}}=\frac{k_0 c_0 \ell^2}{\mathcal{D}}$, the ratio of the diffusion time scale to the reaction time scale is the second kind of the Damkohler number where ℓ is the length scale which was used as the radius of the monoaxial nanofibers, D is the

diffusivity found in literature,[82] k_0 is the rate constant at the reference temperature as calculated previously, and c_0 is the initial concentration of glucose. This yields a Damkohler number of 7.88 for the monoaxial nanofibers with a Ni: Si ratio of 1:4 and a catalyst: glucose ratio of 1:3.33, which implies that the diffusion time scale is much longer than the reaction time scale and thus there is a significant mass transfer limitation imposed by this system. Further, the effectiveness factor which is defined as the average reaction rate with diffusion divided by the average reaction rate if the rate of reaction is evaluated at the bulk-stream (or boundary condition) values, *i.e.*

$$\eta = \frac{\int_0^1 \tilde{c}(\tilde{r})\tilde{r}d\tilde{r}}{\int_0^1 1\cdot\tilde{r}d\tilde{r}} = 2\int_0^1 \tilde{c}(\tilde{r})\tilde{r}d\tilde{r} \qquad (3)$$

was found to be 0.27. The low effectiveness factor as well as the high Damkohler number indicates that there was a large mass transfer limitation imposed by the system.

Therefore, coaxially generated nanofibers were used to attempt to overcome these mass transfer limitations by shortening the diffusion length via tuning the catalyst toward the surface of the nanofiber. In these coaxial nanofibers, as mentioned previously, a pure silica solution was used as a core with a silica solution containing high concentrations of nickel precursor used as a shell solution in the concentric ring geometry. It is also of note that higher concentrations of nickel precursor were able to be used in the shell than were able to be used in monoaxial nanofibers potentially due to the use of the pure silica core to drive the electrospinning process. These coaxially produced silica nanofibers with nickel nanocrystals were then used as catalyst systems in the alkaline hydrolysis of glucose, as displayed in **Figure 21**, through the same bulk weight loss method as for monoaxial systems previously discussed in Figure 15. Data from these tests is shown in Figures 21a and 21b presented as open data pointes along

with the monoaxial data discussed previously presented as solid data points for comparison. The advantage of placing nickel in the sheath layer via coaxial electrospinning is demonstrated in Figure 21a by presenting the percent conversion versus the overall concentration within the nanofiber, which includes the volume contribution of the pure silica core in the coaxial nanofibers towards the concentration calculation. Here, it is found that coaxial nanofibers produce a conversion of 91% with an overall Ni: Si ratio of 1:24 (generated using a shell Ni: Si of 1:6 with a core/ shell flow rate of 0.04/0.01 ml/min), while monoaxial nanofibers required a Ni: Si ratio of 1:6 to reach such conversions. This confirms that by utilizing coaxial electrospinning the catalyst required to produce > 90% conversions is decreased by a factor of 4. The percent conversion versus the shell concentration is presented in Figure 21b. Again, this is presented along with the monoaxial data for comparison. It is observed that both the monoaxial and coaxial data appear to nearly align on a single trend line, indicating that it is only the catalyst located within that shell that contributes to the catalytic properties of the nanofiber system.

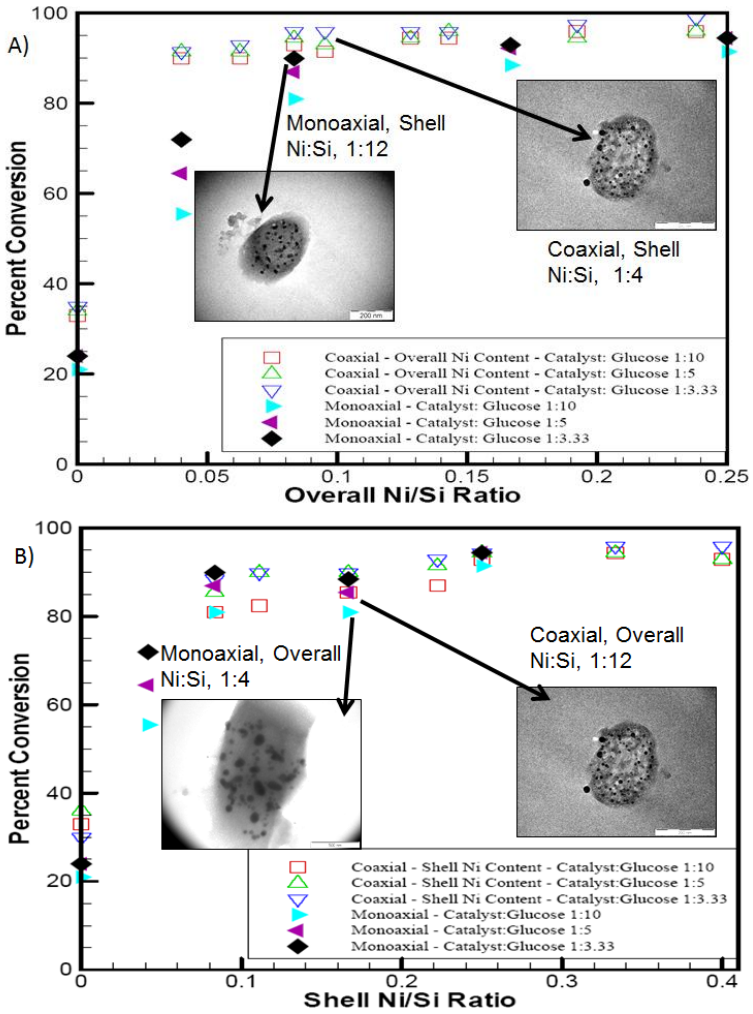

Figure 21. Alkaline hydrolysis of glucose using silica nanofibers containing nickel crystals via the bulk weight loss method. Data is presented with the percent conversion based on the overall change in mass versus (a) the ratio of nickel versus silica overall within the coaxial nanofibers, and (b) the ratio of the nickel versus silica only including what theoretically should be located within the shell region.

Here, the second Damkohler number was calculated again to determine how the change in length scale affected the efficiency of the reaction. The length scale in the coaxial system was reduced to 70 nm which was the average length of the sheath layer within the nanofibers where the bulk of the catalyst is located. With the same reaction constant used for the same reaction profile, the second Damkohler number is calculated to be 0.87, which corresponds to the effectiveness factor of 0.82.

Therefore, by placing the catalyst selectively toward the surface of the nanofiber thereby reducing the diffusion length, the efficiency of the reaction is increased dramatically. A final comparison of the iron and nickel monoaxial and coaxial nanofibers produced in this study and the previous one is supplied in **Table 5**. Here the reaction rate constants calculated for the second order reaction, the Damkohler number and the effectiveness factor calculated to describe the mass transfer limitations found are presented. In this context it can be seen that while the monoaxial nanofibers produce high conversions, there is still a strong mass transfer limitation as shown by the high Damkohler number and the low effectiveness parameter. However, when the catalyst is tuned toward the surface these restrictions are decreased in the iron case as shown, but they are even further decreased in the nickel case as shown by the Damkohler number less than one and the effectiveness parameter about 0.8. It can also be seen that under the same heating conditions the reaction rate coefficient for the iron case is nearly half that of the nickel case which further shows that nickel surpasses iron in catalytic performance found by conversion, selectivity, and now reaction rate coefficient.

Sample	Reaction Rate Constant	Damkohler Number	Effectiveness Factor	Final Conversion
Monoaxial Iron	$5.3*10^{-6}$	9.84	0.176	82%
Coaxial Iron	$5.3*10^{-6}$	2.72	0.526	86%
Monoaxial Nickel	$1.2*10^{-5}$	7.88	0.27	93%
Coaxial Nickel	$1.2*10^{-5}$	0.87	0.82	95%

Table 5. A comparison of the reaction rate constants, Damkohler numbers, effectiveness factors and final conversions found for monoaxial and coaxially produced silica nanofibers containing iron or nickel nanocrystals.

Further, the hydrogen selectivity generated by these catalytic coaxial nanofibers was analyzed. **Figure 22** presents RGA data comparing monoaxial and coaxial catalytic nanofibers. Figure 22a presents the monoaxial data presented previously in Figure 16b for a heating rate of 2ºC/min. Figure 22b presents the same heating rate and reaction conditions but using coaxially produced nanofibers with a shell Ni: Si ratio of 1:2.5 and an overall Ni: Si ratio of 1:4. As can be clearly seen, coaxial silica nanofibers have a similar ultra-high conversion with an even increased hydrogen/bulk weight loss conversion ratio indicating an increased overall selectivity toward hydrogen. Further, the coaxially produced silica nanofibers have a maximum hydrogen production rate at a lower temperature than the monoaxially produced nanofibers indicating a shift in the time sensitivity of the reaction due to the increased catalytic surface area and the increased efficiency factor previously discussed. Finally, there is a further separation between the temperature (and thus the time) at which hydrogen in produced versus the temperature at which the byproducts are produced from the thermal degradation of the remaining glucose. Figure 22c presents the mole fraction of hydrogen versus temperature for both monoaxial versus coaxial nanofibers. From this Figure it can be seen that coaxial nanofibers have a larger temperature range at which nearly pure hydrogen is produced, and thus placing nickel nanocrystals selectively into the sheath layer can increase the maximum reaction temperature for pure hydrogen production from 140ºC to 200ºC. It is also observed that the monoaxial case displays a slower decrease in selectivity due to the production of byproducts during the tail end of the production of hydrogen gas. From this analysis, it appears that the availability of catalyst at low temperature and time can maximize the selectivity of hydrogen production and produce nearly pure fuel gas with ultra-high conversions.

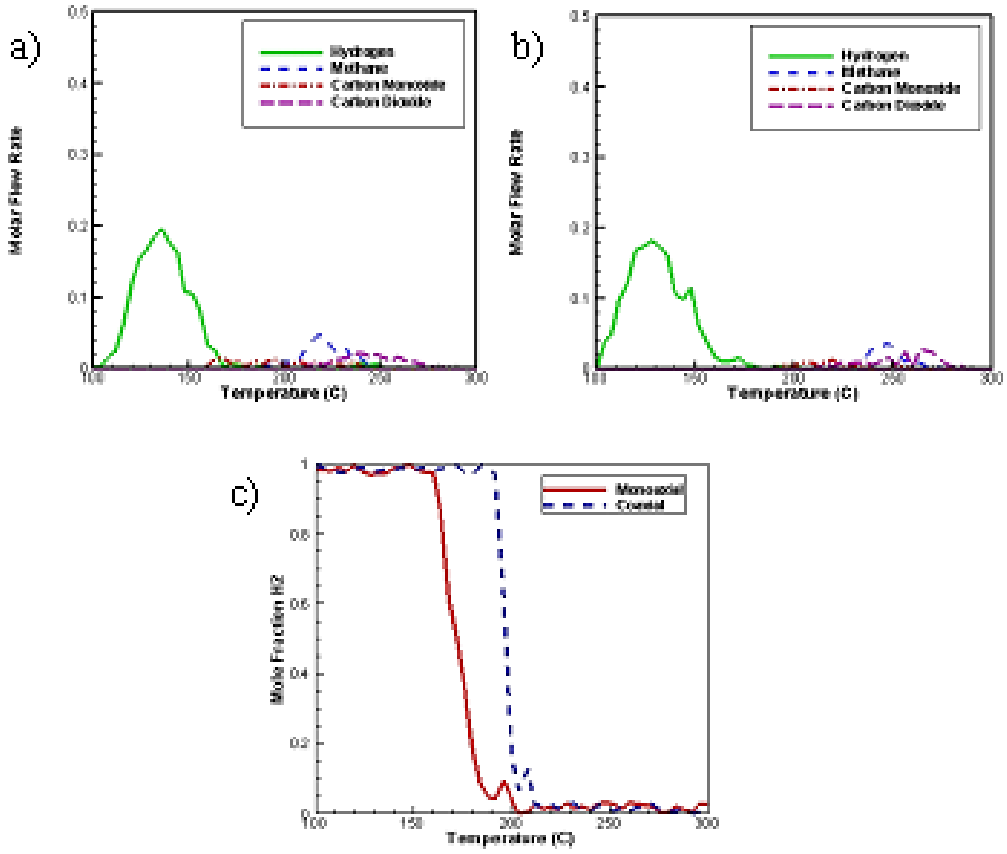

Figure 22. RGA analysis of gaseous products for (a) monoaxial silica nanofibers with a Ni: Si ratio of 1:4 and (b) coaxial silica nanofibers with an overall Ni: Si ratio 1:5. (c) The selectivity of hydrogen is presented through RGA by plotting the mole fraction of hydrogen versus temperature for both monoaxial and coaxial nanofibers.

4. Conclusions

Precursor nanofibers have been fabricated via electrospinning and sol-gel synthesis along with the incorporation of nickel precursors. Subsequent thermal treatment generates uniform silica nanofibers with nickel or nickel oxide nanocrystals depending on the thermal treatment conditions. These nanofiber/nanocrystal systems were then applied as catalysts in the alkaline hydrolysis of glucose for hydrogen production. Monoaxial nanofibers demonstrated that the reduced form (nickel) has superior catalytic properties over the oxidized form (nickel oxide) and that nickel is

more efficient than the previously reported iron catalyst case. Further analysis of the gaseous streams was then conducted to show that by tuning the heating rate or the final temperature high selectivity with nearly zero carbon monoxide content and high conversions greater than 90% can be attained at relatively low temperatures. Further, the kinetics of the reaction profile were analyzed and used to calculate rate constants based on the gas production profiles. These profiles, as expected, detailed an increase in reaction rate uniformly, but a significant increase in methane and carbon dioxide production at increased temperature. By analysis of the second Damkohler number and the effectiveness factor of the reaction, it was found that there was a significant mass transfer limitation in the monoaxial nanofibers that was alleviated by placing the catalyst selectively within the shell of the coaxial nanofibers. These coaxial nanofibers were then applied as similar catalysts and used to show that the catalyst located within the shell region is the only catalyst used in the conversion and that similar catalytic efficiencies can be achieved with significantly reduced catalyst loading due to tuning the catalyst location. Through analysis of the produced gas, it was determined that little could be done to increase reaction rate through thermal means, while still maintaining the hydrogen selectivity. These electrospun silica nanofibers containing nickel nanocrystals have been shown to be extremely effective catalysts at producing a tunable purity of hydrogen gas from glucose.

CHAPTER 4

CONTROL OF CATALYST GEOMETRY AND LOCATION WITHIN HIGHLY LOADED WATER BASED ELECTROSPUN NANOFIBERS FOR SELECTRIVE HYDROGEN PRODUCTION FROM BIOMASS VIA ALKALINE HYDROTHERMAL TREATMENT

1. Introduction

Currently there are a vast array of different approaches for converting biofuel feed stock such as microbial bioremediation,[83] pyrolysis,[81] gasification,[84] steam explosion,[85] and others,[86] to useable energy products such as alcohols,[87] simple sugars,[88] or hydrogen gas.[89] One less studied method that is beginning to garner interest due to the simplicity of the reaction scheme and usefulness of both the benign solids products as well as the clean, useful gaseous products is the alkaline hydrothermal treatment of biomass.[48] This process has been shown to convert cellulosic biomass into hydrogen gas with minimal carbon byproducts and a usable solids product over bulk, meso-porous supports impregnated with catalytic particles (sodium carbonate) at mild temperatures and pressures. It has been proposed that a large portion of the cellulosic biomass reacts first into its glucose monomer and then subsequently into the hydrogen gas and the inert solids product of sodium carbonate,[57] and thus glucose has been the primary biomass component used in this study due to the simplicity of the reaction scheme.[48]

As detailed previously, the bulk catalytic support morphology used previously [48] can have significant drawbacks. While the porosity of the support may allow

penetration beyond typical supports, the near solid state reaction likely inhibits many catalytic sites from being accessed resulting in a large catalyst/reactant ratio required to achieve high conversions. Nanostructured supports have been shown to increase the available surface area and decrease the catalyst domain size, and thus they will be utilized here. Electrospinning has been chosen as the fabrication method for these nanostructured supports due to its cost effective nature and ease of fabrication of diverse materials afforded by this process. Previously sol-gel synthesis has been used to generate nanofibers comprised of a silica matrix with varying concentrations of both iron [40] and nickel [90] catalytic nanoparticles fabricated *in-situ* evenly distributed throughout the nanofiber diameter and tuned toward the surface of the nanofiber via coaxial electrospinning. These studies yielded results indicating that nickel surpassed iron as a catalyst, that the tuning of the catalyst to the surface of the nanofiber both increased the conversion toward hydrogen and decreased the overall required catalytic loading. Further it was shown that by varying the heating rate or the final temperature in a constant temperature reaction the selectivity of hydrogen formed and the temperature at which the near pure hydrogen was formed could be tuned while still yielding ultra-high hydrogen conversions.

However, even this silica nanofiber framework displayed a few significant drawbacks.[40] Sol-gel electrospinning includes a number of difficulties including time sensitive viscosity, need for humidity control, and metal precursor reactivity with the silica solution. Further, it was found that when the silica nanofibers were applied as catalysts in the alkaline hydrolysis, catalytic deactivation occurred after immersion in the aqueous sodium hydroxide solution. The catalyst initially transforms from the

reduced, active crystal form to a hydrate, subsequently to an amorphous anhydrous form, and finally after long drying times (20 hours) back to the active, reduced form. It was hypothesized that this deactivation and required drying time may be due to absorption of water by silica, and therefore if the substrate was changed the drying time requirement would decrease significantly. Further, an additional advantage to moving away from sol-gel synthesis could be attained by increasing the number of nanofiber and catalyst morphologies that could be probed, including pure catalyst nanofibers or pure catalyst shells. Here we present a water based approach to generate electrospun nanofiber catalysts of many morphologies - an inert matrix with varying concentrations of discrete nickel domains distributed throughout the nanofiber, an inert matrix with varying concentrations of nickel particles tuned toward the surface, a pure nickel nanofiber catalyst system, and an inert matrix core coated with a pure nickel layer, and others. This approach is shown to not only display surface area advantages over meso-porous, bulk supports, but also catalyst crystal size control indicating additional surface area to volume advantages. Further, the variation of support composition indicates a solution to the deactivation and synthesis problems detailed from sol-gel chemistry. Finally, these nanofibers demonstrate that by controlling both the concentration and the geometry of the catalyst toward the surface of the nanofiber, the conversion of glucose to hydrogen can be maximized and a wider temperature range can be found with nearly pure hydrogen produced.

2. Experimental Methods

Solutions containing aqueous 10 wt. %, 79 kDa, 99.7% hydrolyzed PVA as purchased from Sigma were heated at 95℃ for 8 hours. These solutions were then mixed with a previously prepared solution of *x* grams metal or ceramic acetate, also as purchased from Sigma, 1 gram water, 1 gram acetic acid, and 0.05 grams surfactant with *x* varying to control the PVA to metal ratio. After these solutions mixed for 2 hours, electrospinning occurred using a Harvard Apparatus PHD 2000 Infusion syringe pump and a HV ES3OP-5W Power Supply at 15 kV, tip to collector distance of 15 cm, flow rate of 0.005 ml/min through a 22 gauge metal needle for monoaxial or an inner flow rate of 0.007 ml/min and an outer flow rate of 0.005 ml/min with inner gauge needle of 24 and outer gauge of 20. Following fiber generation, high temperature thermal treatment using a Mullen Two Zone 1700℃ Tube Furnace, a heating and cooling rate of 5 ℃/min and a maximum temperature of 600℃ for 2 hours under a flowing argon environment at 0.8 cc/min was used to remove the PVA and acetate ligand resulting in amorphous ceramic or crystalline metal nanofibers. A Scintag Theta-Theta X-ray Diffractometer was used to detail crystal content, size and structure through X-ray diffraction patterns, a Leica X95 Scanning Electron Microscope was used to view nanofiber mat morphology, and FEI Tecnai G2 T12 Spirit TEM STEM was used to view crystal structure within the nanofiber domain through transmission electron microscopy images and energy dispersive X-ray spectroscopy.

Mats of calcined nanofibers were broken into millimeter size sections and then added to d-glucose as purchased from Sigma in a 1:10 catalyst: glucose ratio. 50

wt. % aqueous NaOH solution was then added to twice the stoichiometric requirement. This was subsequently entrained in a dual outlet glass reactor vessel and placed in a Vulcan 3 130 Box Furnace. This was heated at 25℃/min under flowing argon to 100℃ for the necessary drying time. Finally the sample was heated at 2℃/min to a maximum of 300℃. The outlet gas line was connected to a low pressure leak valve which then fed the gas into an Extorr XT200 Residual Gas Analyzer which detailed the partial pressure of the corresponding molecular masses in the gaseous products, similar to a rugged mass spectrometer. From these partial pressures and known ionization potentials, the concentration of each component in the gas stream and subsequently the conversion was calculated. Various known gasses were used to verify the accuracy of the RGA system and found to have less than a 1.7% error in analysis of the components interested in here.

3. Results & Discussion

A schematic detailing the general approach toward water based electrospinning to generate catalytic nanofibers of various morphologies is presented in **Figure 23**. Polyvinyl alcohol and high concentrations of metal acetates, up to a molar ratio of 1:4 polymer: metal, are covalently bound via heating and mixing in aqueous solution, with these two chosen particularly because of their known interaction.[91] This high loading and covalent bond generation increases the homogeneity of the metal distribution throughout the polymer chain, inducing proper solution properties for electrospinning. Following electrospinning, resultant nanofibers are collected and taken for thermal treatment to remove the polymer and induce crystallization of metal

nanocrystals. The morphology of these nanofibers is shown to strictly depend on the precursors included in the initial electrospinning solution as well as the electrospinning geometry.

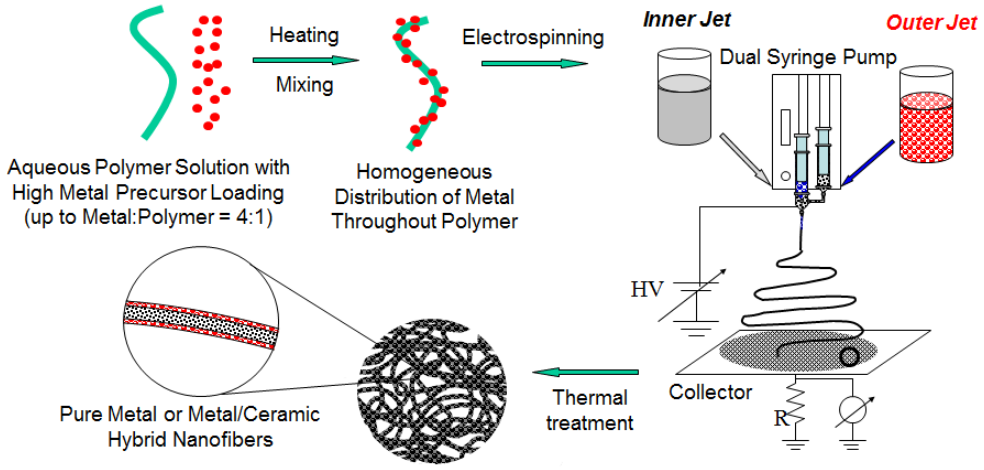

Figure 23. Schematic on the generation of pure metal or ceramic nanofibers of various compositions. The tuning of composition and morphology is done by varying inner and outer solution flow rates and relative precursor to precursor and precursor to polymer ratios. Also available is monoaxial electrospinning where a single syringe pump and as single solution is used.

The loading mechanism is further probed by FTIR of as spun nanofibers with various metal acetate concentrations. The known interaction discussed previously by Cho et al. described the ability to highly load hafnium nanoparticles surface functionalized with acetate ligands, but little was discussed about the mechanism of attachment to PVA. According to **Figure 24** it is seen that the raw polymer produces an -OH band, a -CH band, and a -CO band due to the alcohol group. However, with low concentrations of nickel acetate bound and electrospun, there is the initiation of a -C=O bond, an amplification of the -C-O band and an amplification of the -OH band. The -C=O and -C-O band characteristics are due simply to the inclusion of the nickel

acetate, and the amplification of the -OH band is potentially due to the hydrolysis of the remaining acetate ligands on the nickel acetate. As can be seen, with increasing metal acetate concentration the -CO and -C=O bands decrease due to the decreasing amount of acetate ligands, the and the -OH band decreases continuously due to increased bonding between the PVA and metal acetate. Finally, at a mass ratio of 4:1 nickel acetate: PVA the -OH band is reduced to its maximum indicating there is a near saturation of the PVA with metal and nearly all the -OH groups have been reacted off the polymer. This indicates not only a maximum loading of metal to polymer, but also a homogeneous distribution of metal on the polymer chain which allows for homogeneous solution properties and thus an easily electrospinnable solution.

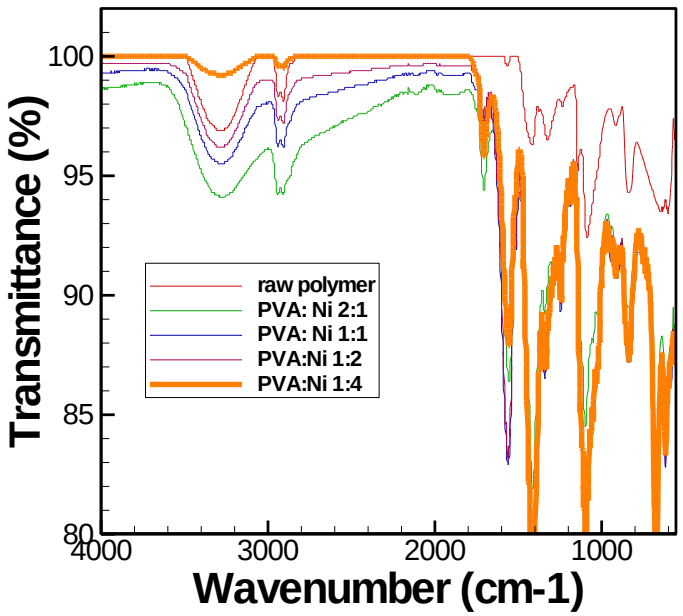

Figure 24. FTIR of raw PVA and PVA-nickel acetate as-spun nanofibers with various concentrations of nickel detailing the loading mechanism for homogeneous metal distribution.

Nanofibers were then generated either monoaxially or coaxially with single or

multiple precursors in each domain depending on the morphology desired. Thermal treatment then occurs to remove the organic components and crystallize the metal as detailed previously.[92] One primary concern when using polymer electrospinning to generate inorganic nanofibers is the complete removal of the organic components. Energy dispersive x-ray spectroscopy is used to quantify the atomic ratio of samples microtomed and viewed under TEM. A bank of these TEM dark field images are presented in **Figure 25** along with a bar graph for the atomic percent found at each of these points. As can be seen, in all samples and locations the atomic percent of carbon is below 2% with the metal content remaining above 70% indicating the samples are void of large carbon deposits. This details, along with bright field TEM to be presented later, that the nanofibers indeed are purely inorganic.

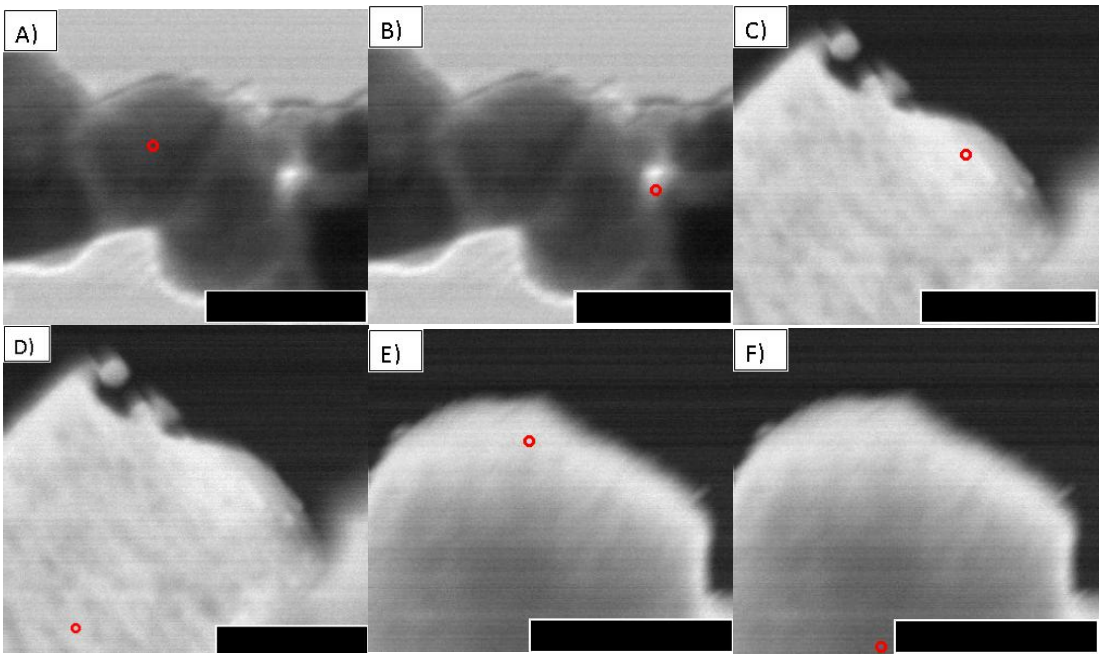

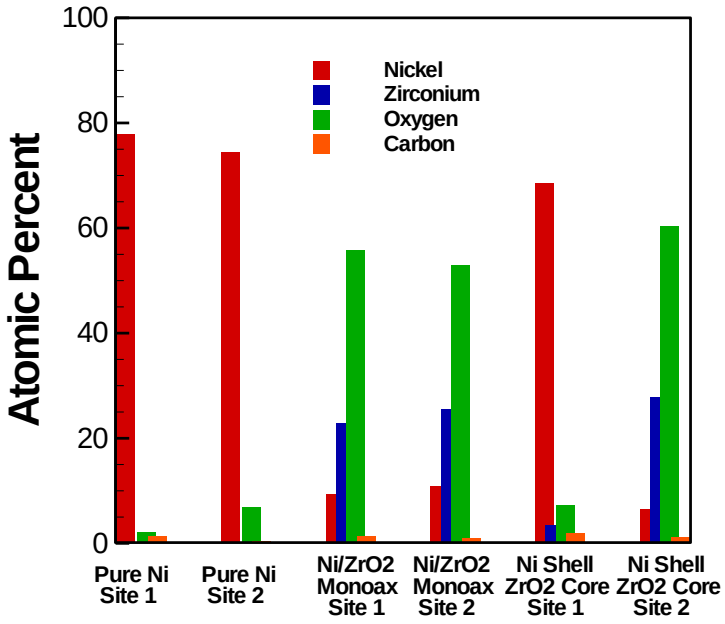

Figure 25. Energy dissipative x-ray spectroscopy results for three morphologies at two locations, pure nickel (A-B), nickel in zirconia monoaxially (C-D) and a pure nickel shell with a pure zirconia core (E-F) as well as a graph detailing the atomic percent at each location.

Further, to probe the morphology of the samples bright field TEM was used to view the different morphologies achieved through electrospinning. A bank of TEM images of microtomed nanofiber samples is presented in **Figure 26** displaying the diversity of this method. Monoaxial pure nickel nanofibers (26a), coaxial nickel nanofibers with a pure nickel shell (26b), monoaxial alumina nanofibers with discrete nickel crystals at low (26c) and high (26d) concentrations and coaxial alumina nanofibers with nickel nanocrystals tuned toward the surface (26e) are presented. Similar nanofibers were also created with a zirconia substrate in the same morphologies. As can be seen from these figures, fibers are fabricated with the intended structure, composition, and morphology and the catalyst concentration and geometry are tuned based on the ratio of ceramic precursor to metal precursor included in the initial solution as well as the electrospinning scheme used. It should be noted that the pure alumina core anticipated in Figure 26b wasn't present, potentially due to the diffusion of metal precursor into the core during electrospinning and/or crystallization. However, the pure nickel shell is still intact and serves as a purely catalytic surface with a reduced catalyst concentration in the core.

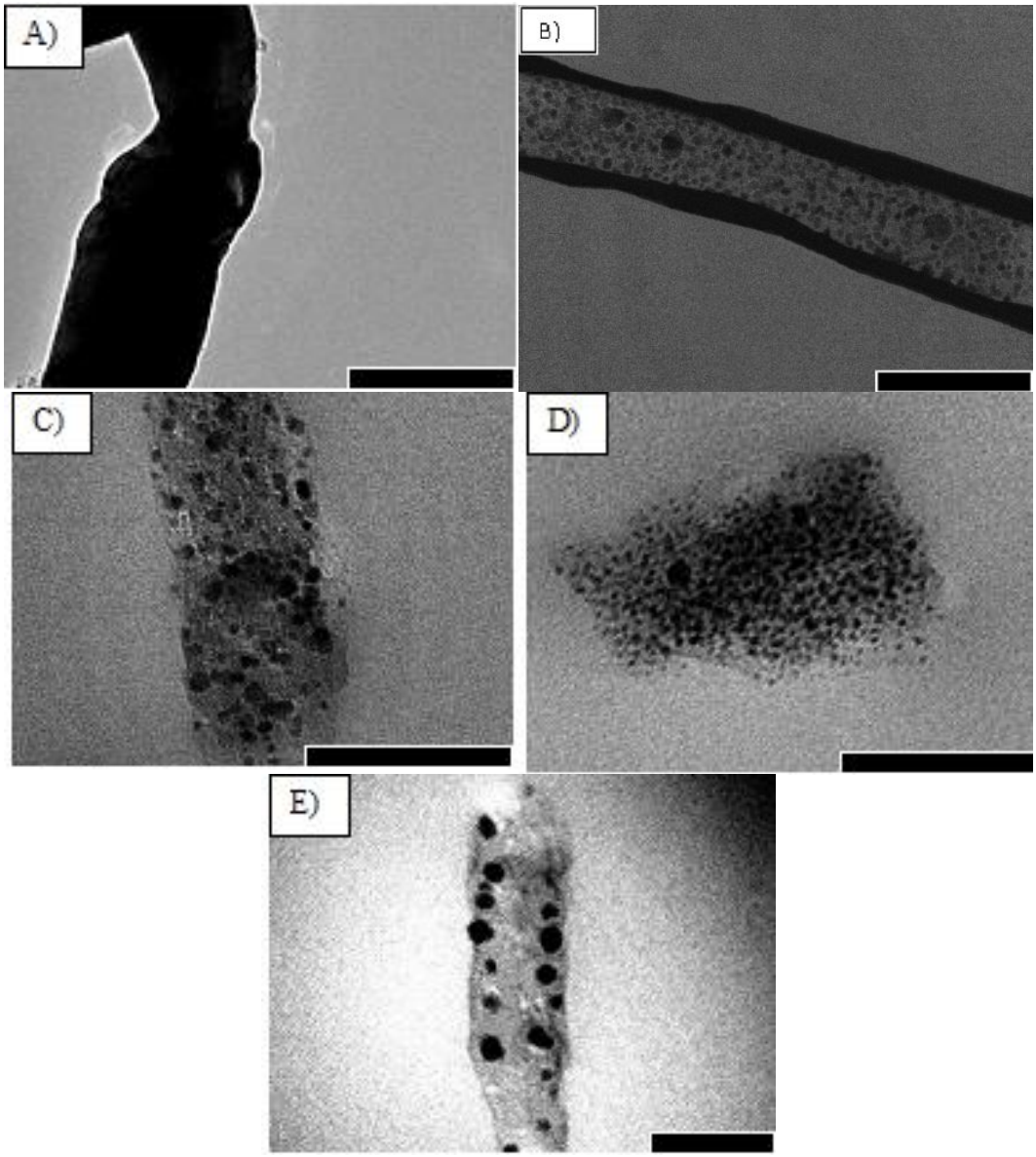

Figure 26. Microtomed samples of catalytic nanofibers viewed under TEM. Nanofibers displayed are (a) pure nickel, (b) pure nickel shell, alumina core, (c) monoaxial alumina with low concentration of nickel, (d) monoaxial alumina with high concentration of alumina, (e) coaxial alumina with discrete nickel domains toward surface s pure alumina core. Scale bar is 100 nm.

The nanofiber catalysts were then compared to the bulk, impregnated catalyst supports previously described.[48] The primary objective of the electrospinning process is to decrease the catalyst size, increase the surface area to volume ratio, and

increase the availability of that surface area to the reactant thereby decreasing the potential mass transfer limitations. It is well known that nanofiber systems have an optimized surface area to volume ratio, and so to analyze the size of the catalytic nanoparticles hydrofluoric acid was used to remove the silica, alumina, or zirconia support in both bulk and nanofiber case to analyze the catalyst crystals specifically under TEM. Average crystal sizes for the bulk support method were 117, 102, and 107 nm for silica, zirconia, and alumina bulk impregnated supports, respectively. This differs greatly from the water based electrospinning approach to produce nanofibers containing catalytic nanocrystals. When nanofibers were dissolved and crystals recovered, the average crystal size was 18, 15, and 21 nm for silica, zirconia, and alumina nanofibers, respectively, indicating almost an order of magnitude decrease in diameter and thus a great increase in surface area to volume ratio. Further, there is an increase in available surface area to volume ratio simply afforded by the nanofiber morphology versus bulk catalytic supports, indicating the strong advantages of the nanofiber based catalyst design.

These nanofibers were then used as catalysts in the alkaline hydrolysis of biomass. First, various drying times were tested to analyze whether a change in support composition in fact would overcome the deactivation phenomenon observed from the sol-gel nanofibers. A graph displaying the percent conversion as calculated through the bulk weight loss during calcination versus the length of drying time at 100℃ prior to alkaline hydrolysis reaction is shown in **Figure 27**. Each sample contains nanofibers with a nickel to glucose molar ratio of 1:10 and a nickel to substrate molar ratio of 1:4 for nickel nanocrystals in silica, zirconia, and alumina. It

is shown that ultra-high conversions (>90%) with are found after a drying time of only 30 minutes when the zirconia or alumina is used as the substrate, while silica nanofibers still require > 20 hours to reach high conversions indicating absorption and deactivation of the catalyst occurs similarly.[40] This indicates that zirconia and alumina do not suffer the same deactivation of catalyst as silica nanofibers, which allows for shorter drying times allowing a more economical process.

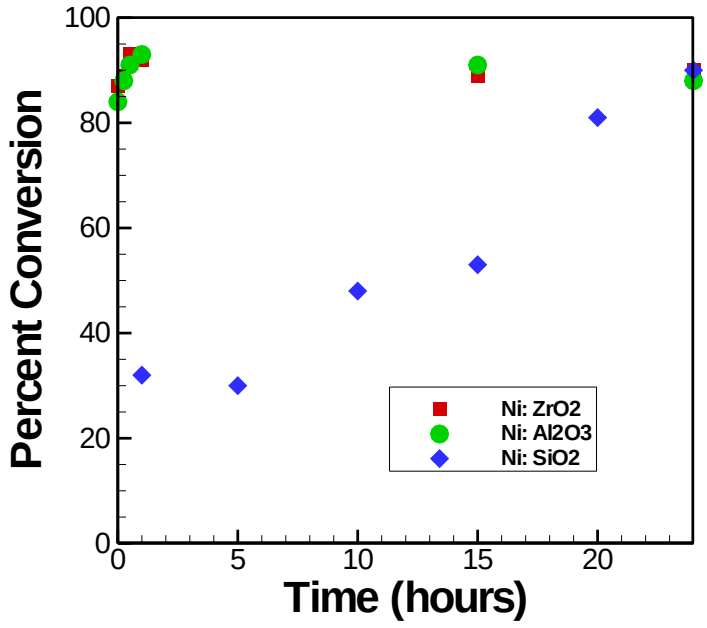

Figure 27. Drying time analysis based on the bulk weight loss calculations of conversions indicating that a change in substrate does indeed decrease the drying time required from 24 hours to ~30 min.

The sol-gel fabrication method discussed previously [40, 90] also detailed that primarily only the concentration of catalyst within the shell of the nanofiber is accessible by the reactant and any catalyst at the core of the nanofiber is inactive due to mass transfer limitations as indicated by monoaxial and coaxial conversion comparison as well as Damkohler number and effectiveness factor calculations.

However, the water based approach allows control not only of catalyst location, but also of the geometry of the catalyst at the surface, which is shown by **Figure 28** to have a large impact on the catalytic performance. Figure 28a details the available surface area within each catalytic nanofiber sample while Figure 28b displays the mole fraction of hydrogen in the gas stream versus the temperature at which the gas was detected for each nanofiber and catalyst morphology tested. From this it is observable that, while each of these nanofiber systems produced conversions of greater than 90% based on hydrogen production with less than 9% carbon byproducts, the composition of the gas stream is tunable based on catalyst location and composition, which is essential if this gas stream were to be used in an application such as an H_2/O_2 fuel cell. From Figure 28a it can be seen that low catalyst concentration monoaxial nanofibers have a relatively low available surface area of catalyst distributed throughout the nanofiber domain, which results in a gas steam containing near pure hydrogen only up to 141 ℃. Further gas production occurred but was contaminated by carbon products limiting the usefulness of these gaseous products. Increasing the catalyst concentration within monoaxial nanofibers increases the available surface area throughout the entire nanofiber diameter as seen in Figure 6a, and subsequently the near pure hydrogen increases to 163 ℃ for moderate concentrations and finally to 179 ℃ for high concentrations as seen in Figure 28b. These nanofibers, though, still display some mass transfer limitations for the reactant to reach the active catalytic sites at the core of the nanofiber indicating that some catalyst is wasted.

Pure nickel and pure nickel coated zirconia and alumina nanofibers were also

created and tested to saturate the surface of the nanofiber with available catalytic sites. The temperature range for which near pure hydrogen was produced increased further to 183 ℃, which corresponds to a dramatic increase in available catalytic sites at the surface of the nanofiber. However, the overall availability of catalytic sites here is limited to the surface of the nanofiber as any catalyst located inside the nickel domain is limited. Thus, while this contains the most catalyst, the geometry of the catalyst was tuned further to have high concentrations of discrete domains at the surface of the nanofiber. This allows for a maximization of nickel surface area within the diffusion length scale of reactant to catalyst surface. This produced the highest overall available surface area within the top third of the nanofiber system as seen by Figure 4a, and corresponded to a further increase of 10 ℃ up to 193 ℃ where near pure hydrogen is produced. This indicates that, not only by increasing the concentration of catalytic domains, but decreasing the catalyst size and tuning the location even in the nanofiber case increases the catalytic efficiency.

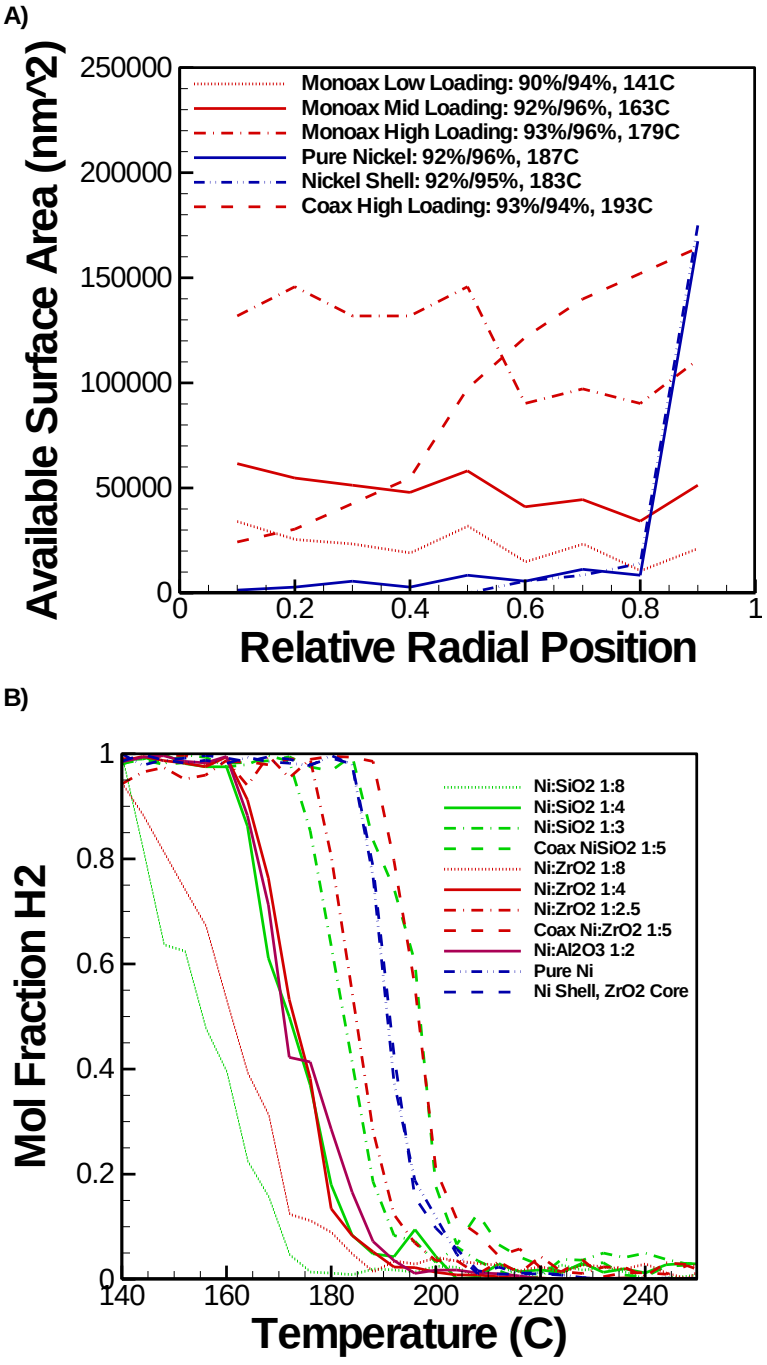

Figure 28. (a) Functional surface area is plotted versus the relative radial position located throughout the nanofiber domain as the catalyst located within the closest seventy nanometers of the nanofiber surface is available for catalytic activity. (b) Moll fraction of hydrogen sampled within the gas stream at each temperature for various nanofiber morphologies tested.

4. Conclusions

In summary, we have presented a purely water based route to produce nanofibers with a variety of morphologies through the generation of covalent bonds between a metal/ceramic precursor and a polymeric backbone. The subsequent electrospinning of this solution followed by a controlled thermal treatment removes the polymer and precursor ligands, crystallizes the metal leaving a pure metal or metal and ceramic nanofiber with no organic component. By varying the electrospinning conditions and arrangement, precursor inclusion and the thermal treatment, morphologies ranging from pure metal to ceramic with discrete metal domains to metal domains tuned to the surface all the way to a ceramic core coated with a metal layer are generated. It was found that nanofibers produced in this method can generate catalytic domains with an order of magnitude smaller diameter than typical bulk, impregnated catalytic supports. These nanofibers were then used in the alkaline hydrothermal treatment of glucose. Previous work had shown that nickel loaded in silica nanofibers produced high conversions with high selectivity, but the catalyst deactivated during thermal treatment and long drying times to regenerate the catalyst into its functional, reduced form were required. Here it is shown that a change in substrate - made possible by the water based electrospinning described above - decreases the drying time required from 24 hours down to 30 min while still producing hydrogen conversions greater than 93% with selectivity better than 3%. Further, through the generation of catalyst with such unique morphologies it was found that by increasing the number of available active catalyst sites within the nanofiber, the temperature range at which nearly pure hydrogen was produced increased up to 35℃

using monoaxial nanofibers. Pure nickel and zirconia coated with nickel were used, which increased the surface concentration of active sites beyond that of monoaxial nanofibers and subsequently the temperature range where near pure hydrogen seen was increased a further 5℃. Finally, coaxially produced nanofibers with high concentrations of discrete nickel domains in a ceramic shell surrounding a ceramic core were fabricated and it was found that even beyond increasing the concentration of catalyst used, the control of the geometry of this catalyst at the surface of the nanofiber plays a great role in the catalytic effectiveness. The nanofibers with the greatest surface area of catalyst available within the diffusion length scale of reactant were the coaxial nanofibers with discrete catalyst domains at the surface, which in turn produced the greatest selectivity and the highest conversion based on hydrogen gas produced. Further these nanofibers also produced greatest temperature range at which near pure hydrogen was detected. This effectiveness and benefit of this approach is therefore the control of the substrate through electrospinning controls crystal size and available surface area, while control of the catalytic morphology – specifically allowed by this water based electrospinning approach – can increase the number of available active catalytic sites within the diffusion length scale of the reactant resulting in higher conversions, higher selectivity, a larger temperature range at which near pure hydrogen is produced all with a lower overall loading of catalyst in the framework.

CHAPTER 5

METAL NANOFIBERS WITH TUNABLE ELECTRICAL AND MAGNETIC PROPERTIES VIA HIGHLY LOADED WATER BASED ELECTROSPINNING

1. Introduction

Recently a large focus has been given to nanoscale materials due to their very interesting size dependent properties,[93, 94] especially electrical conductivity [95] and magnetic coercivity.[96] Further, nanomaterials with high aspect ratios have been fabricated with the goal of controlling their electromagnetic properties for applications such as data storage, power generation, and filtration among others. Many methods have been devised to synthesize a broad array of one-dimensional materials,[19, 97] but one method that presents great potential due to its inexpensive nature and ability to produce diverse materials with various morphologies is electrospinning.[31, 98] Previously purely metallic nanofibers have been electrospun from aqueous polymer solutions containing metallic precursors, followed by thermal treatment to remove the polymer matrix and to form metal crystals.[99-102] However, the use of low metal precursor concentrations resulted in weak and coarse fibers due to the disintegration of the polymer matrix in fibers during calcination, and little work was done to increase the loading of metal precursor and thus the yield and properties of metal nanofiber. Previous work on purely metallic electrospun nanofibers surfaced the measurement of the magnetic [99-102] and electrical [103] properties, and lacked the analysis detailing the effect of crystal size or density on the coercivity or electrical conductivity. In the

present communication, we present a facile method to generate pure metal nanofibers by water based electrospinning with ultra-high loading of metal precursor (up to the ratio of metal precursor to polymer by mass of 4:1), and finally control the crystal structure within the resultant metal nanofibers to subsequently tune the magnetic and electrical properties. Further, we use an alignment apparatus to generate anisotropic electrical conductivity throughout the electrospun metal nanofiber mat. Finally, we finish by presenting studies detailing the use of two precursors to contain discrete metal crystals within an electrically insulating ceramic nanofiber matrix, subsequently decreasing the metallic crystal size and thereby allowing the further control of the magnetic properties. Through this analysis, it is shown that the electrical properties can be tuned from highly resistive to near bulk electrical conductivities – orders of magnitude greater than previously reported methods – while the magnetic properties are tuned from highly coercive to superparamagnetic behavior by controlling the composition of these nanofibers, the crystalline morphology within the nanofiber matrix, and the degree of orientation of the nanofiber mat.

In the current work, metal acetate precursors and polyvinyl alcohol have been used due to the known interaction between these two,[91] allowing for very high concentrations of precursor to be bound to the polymer in a homogeneous fashion and to maintain spinnability during electrospinning. Nanofibers containing metal acetate to polymer mass ratio of 4:1 were electrospun and subsequently thermally treated. The metals tested and presented here are copper, solely for its electrical conductivity, and nickel, cobalt and iron for their electrical and magnetic properties. Particular attention is paid to the crystal morphology within the nanofiber diameter as this plays

a critical role in both the magnetic and electrical properties of these nanofibers.

2. Experimental Methods

Electrospinning solutions were prepared by creating an aqueous 10 wt. % solution of polyvinyl alcohol (PVA, 99.7% hydrolyzed 79 kDa), a 1:1:1 water: acetic acid: metal acetate by mass solution, and mixing them in the proper ratio to create a polymer: metal mass ratio of 1:4. Electrospinning was carried out on a Harvard Apparatus PHD 2000 Infusion syringe pump at 0.005 ml/min at an electric field of 1 kV/cm generated by an HV ES3OP-5W power supply. Thermal treatment was conducted in a Mullen Two Zone 1700ºC tube furnace with gas flowing at 0.8 cc/sec. The first thermal treatment (scheme 1) consisted of heating to 400ºC, holding for 2 hours under flowing argon. The second thermal treatment (scheme 2) consisted of heating to 400ºC for 2 hours under air, then subsequently heating to 400ºC and immediately cooling under flowing argon. The third thermal treatment (scheme 3) consisted of heating to 800ºC for 2 hours under flowing argon. All heating and cooling rates were 5ºC/min. Samples were viewed with a Leica 440 SEM or an FEI Tecnai G2 T12 Spirit TEM STEM, electrical properties were tested using a two point probe following ASTM Standards for Conducting Materials, and magnetic properties were tested using a Quantum Design MPMS-XL SQUID using ROS variable field scanning at a constant temperature.

3. Results & Discussion

Figure 29 presents a bank of transmission electron microscopy (TEM) images of four different metal nanofibers (columns) where the thermal treatment conditions were varied (rows). The first thermal treatment condition that was tested was low temperature (400ºC) under inert atmosphere. As can be seen by the images presented in Figure 29a, this thermal treatment condition generates nanofibers with small discrete crystalline domains supported within an amorphous metal nanofiber matrix. Energy dispersive X-ray spectroscopy (EDAX) confirmed that the amorphous regions had extremely low carbon content (< 0.25%) and were primarily metallic with minor concentrations of oxygen, perhaps indicating a metallic amorphous region with low ordered structure. These samples were subsequently microtomed and imaged under TEM to analyze the distribution of crystal throughout the fiber. As presented in Figure 29b, these crystal domains in microtomed metal nanofibers are evenly distributed throughout the fiber in all cases. The crystal size is much smaller and density is much higher in the nickel and iron case as opposed to the cobalt and copper case, perhaps indicating a difference in nucleation and crystallization phenomena of these metals.

The second thermal treatment tested was at the same low temperature (400ºC) but under air to crystallize the metal into an oxide, followed by low temperature under inert atmosphere to generate reduced crystal. This thermal treatment was used previously [99] to produce reduced crystal in pure metal nanofibers. As can be seen by Figure 29c, this appears to produce isotropic crystals connected at narrow regions generating nanofibers of connected crystals with the amorphous region completely or

nearly completely removed. The cobalt case still contains minor concentrations of amorphous material but the volume fraction of crystal is still significantly higher than in the previous case. These results differ from those previously reported [99] due to the new ability to load a large amount of metal precursors throughout the polymer chain such that during nucleation and crystallization there is a significantly higher probability of encountering stable nuclei and adding to the crystal formation. Therefore, we see well connected domains of crystals with extremely low concentrations of amorphous metal. Finally, the third thermal treatment tested was high temperature (800ºC) under inert atmosphere as presented in Figure 29d. This thermal treatment produced purely crystalline nanofibers across the entire fiber diameter in the copper and nickel case, but only produced large crystals of iron and cobalt supported in an amorphous region.

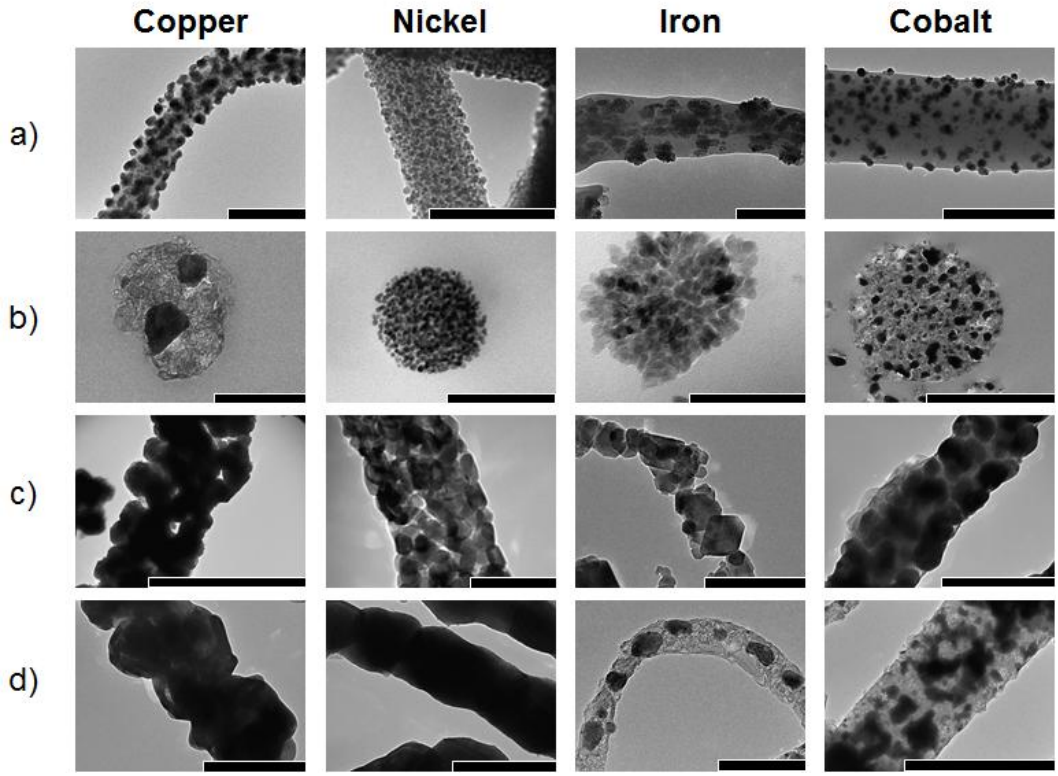

Figure 29. Bank of TEM images for various metallic nanofibers (copper, nickel, iron, and cobalt) from various thermal treatment procedures. a) The surface and b) microtomed cross-section of each metal nanofiber after low temperature (400ºC) treatment under inert atmosphere, c) after low temperature treatment under air and then under inert atmosphere, and d) after high temperature (800ºC) treatment under inert atmosphere. Scale bar is 200 nanometers.

These nanofibers were then tested using a two-point electronic probe to detail the effect of the size and distribution of metal crystals on the electrical conductivity. This data is presented on a log scale in **Figure 30** for each metal nanofiber tested after three different thermal treatment schemes. The data collected is also presented against the control of the known electrical conductivity of bulk crystalline metal of the same composition and crystal type. As can be seen in the Figure, the second thermal treatment scheme which generated nanofibers void of amorphous regions with isotropic crystals connected to each other produced the highest electrical conductivity

near 10^6 to 10^7 S/m, which consistently was about an order of magnitude below the electrical conductivity of the bulk material.

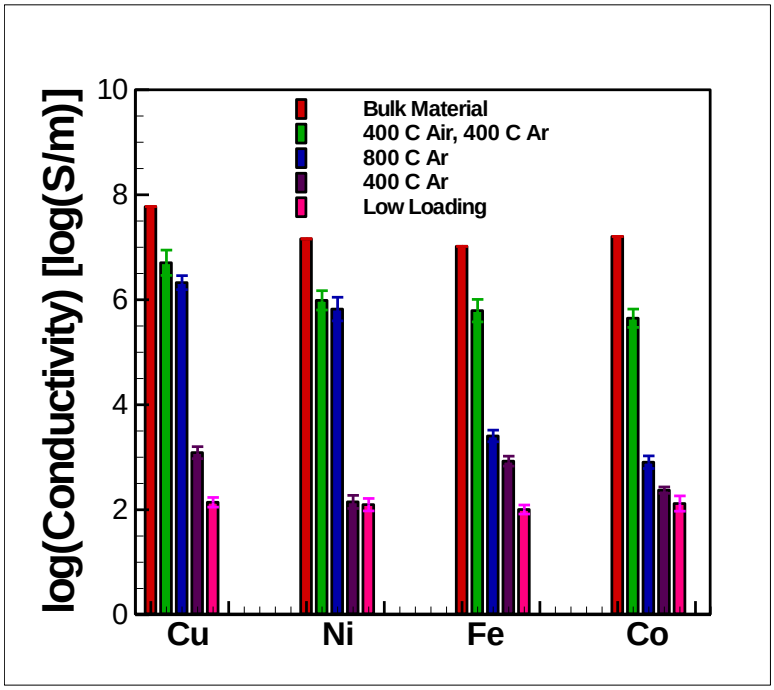

Figure 30. Electrical conductivity data for copper, nickel, iron, and cobalt electrospun nanofibers from various thermal treatment procedures as indicated, all presented on a log scale versus the bulk pure metal value as tabulated and electrical conductivities gained from low loading of metal in precursor nanofibers.

The high temperature thermal treatment (scheme 3) which produced purely crystalline fiber diameters had the second greatest electrical conductivity. In the copper and nickel case where the third thermal treatment scheme reduced the amount of amorphous region to the extent that pure metal diameters were seen, the electrical conductivity rivaled that of the second thermal treatment scheme. With the reduction of the amorphous region, the highly resistive regions of the nanofibers were removed, and thus a higher electrical conductivity was seen. This differs from iron and cobalt where nanofibers from the third thermal treatment scheme still contained significant

quantities of amorphous material and subsequently had a significant reduction in electrical conductivity near that of the first thermal treatment scheme.

The first thermal treatment scheme produced nanofibers containing high concentrations of amorphous region throughout the nanofiber with only small discrete crystal domains. A large amount of more resistive amorphous material remaining subsequently reduced the electrical conductivity to the lowest value seen for each material. However, even with high amorphous content, these values of electrical conductivities (10^2 to 10^3 S/m) are still among the highest seen by one-dimensional nanomaterials.[103] Copper nanofibers were synthesized with metal acetate to PVA ratios of one to two for comparison to the previously presented methods for metallic nanofiber generation. Through this approach, the only thermal treatment that maintained nanofiber morphology was the low temperature air then inert treatment (scheme 2). Further, when using this low loading approach the electrical conductivity of the resultant nanofiber mat was significantly lower than that of the highly loaded approach at 922 S/m. This details the control of nanocrystal morphology and thus macroscopic electrical properties afforded by electrospinning highly loaded solutions generating dense metal nanofibers with extremely high aspect ratio which offers a large number of paths for electrons to transport.

Beyond the isotropic mat generation, electrospinning methods have been generated to produce anisotropic mats of nanofibers. The rotating collector approach has been used in the current study to align copper acetate – polyvinyl alcohol hybrid nanofibers.[104] This method does not match the initial alignment of the divided collector approach,[105] but has been shown to have a more stable alignment effect

over time and maintains the scalability afforded by electrospinning. Thus nanofibers aligned in this fashion were generated, thermally treated and presented in **Figure 31**.

Figure 31a-c present the scanning electron microscopy (SEM) images of as spun nanofibers for three different rotation speeds of the collector – 80, 100, and 120 rps, respectively. These nanofibers were then thermally treated using the second thermal treatment scheme, which was found previously to generate the greatest electrical conductivity throughout the samples tested. These nanofibers are presented through SEM in Figure 31d-f. The degree of alignment is commonly evaluated using the average offset angle. As spun nanofibers had an offset angle of 17.6, 8.3 and 4.1 degrees from the axis of alignment as calculated for two hundred nanofibers viewed under SEM. For comparison, nanofibers collected from a conventional, stationary collector generated an alignment angle of 41.4 degrees, which is nearly isotropic. These nanofibers were then tested for their electrical conductivities as presented in Figure 31g.

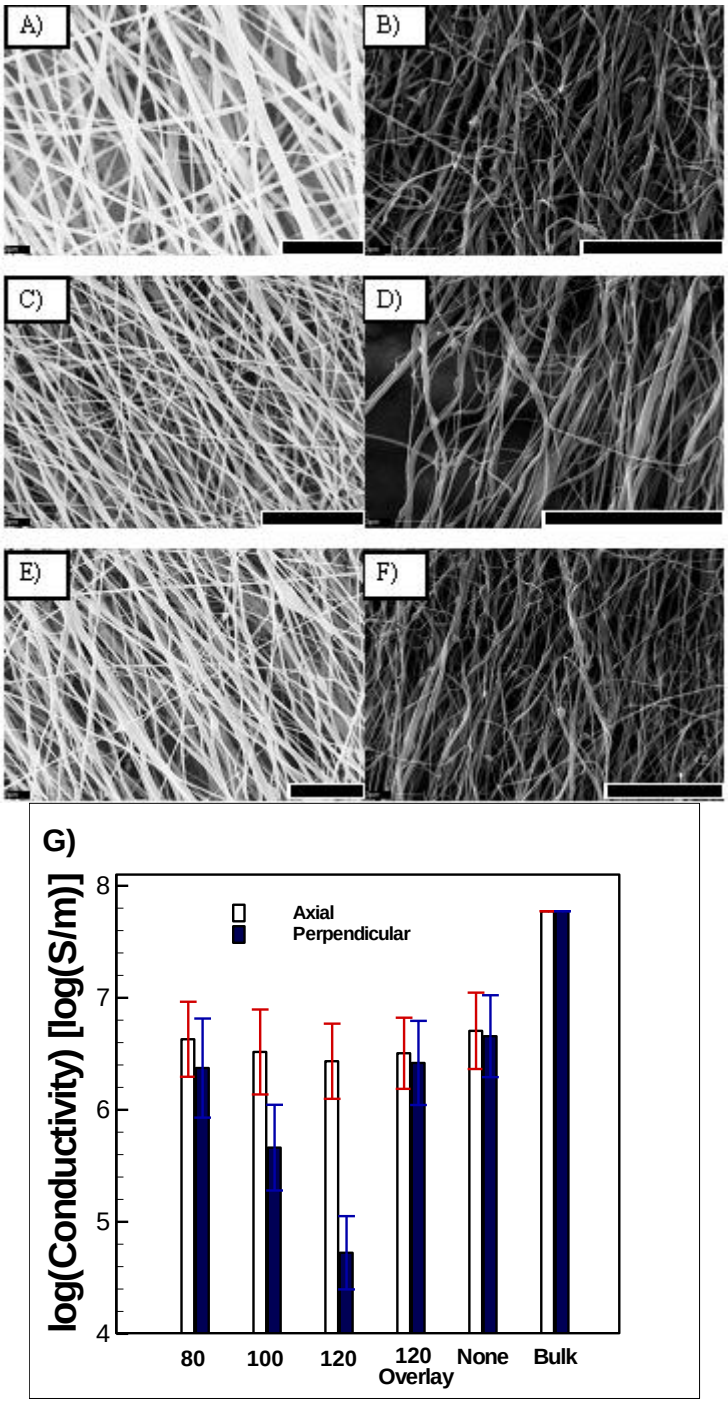

Figure 31. SEM images detailing alignment of (a-c) as spun PVA/copper acetate nanofibers followed by SEM images of these same nanofibers (d-f) following thermal treatment number two is presented, both for three different rotating collector speeds of 80, 100, and 120 rps, respectively. Scale bar is 5 microns. The associated axial and perpendicular electrical conductivity is presented (f) for these three cases as well as the known bulk case, the isotropic nanofiber case and two aligned nanofiber cases overlaid perpendicular to each other.

As can be seen, the axial electrical conductivity of aligned copper nanofibers remains near the value for isotropic electrospun nanofibers on the stationary collector. However, the perpendicular value steadily decreases with increasing the degree of alignment of fibers, and becomes two orders of magnitude lower than that along the axial direction. This is potentially due to the decreased contact in the perpendicular direction allowing for less electron flow. The directional variance in electrical conductivity is a phenomenon only available to aligned one-dimensional materials in such a method as this. Further, layers of nanofibers aligned at 120 rps were stacked on top of each other with perpendicular alignment directions. The electrical conductivity of these samples generated nearly isotropic conductivity measurements again. This confirms in fact that the electrical conductivity can be controlled overall by the crystal structure, but directionally by the alignment and degree of alignment of these electrospun nanofibers.

The iron, nickel, and cobalt nanofiber samples were then taken for the measurements of magnetic properties using superconducting quantum interference devices (SQUID) as presented in **Figure 32**. The saturation field as well as the room and low temperature coercivities of the nickel and cobalt nanofibers produced by the first thermal treatment scheme agree in number and trend with those previously reported for these materials.[99] One major discrepancy that is seen is the iron case. When tested at room temperature, iron has a high coercivity, but when tested at 100 K, near superparamagnetic behavior is seen. Then at 10 K, slightly coercive behavior is seen again but still significantly smaller than at room temperature. These effects were confirmed using low field and zero field cooling tests and significant deviations were

seen from the other temperatures. This can be seen from the three constant temperature field variance tests shown in Figure 32a, as well as the coercivity data presented versus temperature for iron as well as cobalt and nickel in Figure 32b. It is hypothesized that this iron behavior is due to the substantial difference in thermal expansion coefficients associated with amorphous iron and crystalline iron.[106] When cooling the sample, the thermal contraction of the amorphous region occurs faster than the crystalline material, which allows not only for the Neel relaxations to take place, but also for the crystal itself to rotate and align its overall dipole with the field generating a secondary effect, which may appear to generate superparamagnetic behavior at this temperature. Finally, at very low temperature the decrease in temperature reduces the impact of both of these relaxations to the point where some coercivity is viewed again.

Further, the high metal content of these nanofibers allow for a more robust approach to thermal treatment analysis, and thus an analysis of the average crystal size observed versus the coercivity of the sample. The three thermal treatment schemes for each of the three materials tested were analyzed at room temperature using a variable field scan. These results are presented in Figure 32c and 32d, where Figure 32c presents the long moment per gram of sample versus the applied field for the three samples of cobalt as an example, and Figure 32d presents the coercivity of each sample type as a function of observed crystal size. As can be seen in the Figure, the coercivity increases with crystal size for each sample, but is a much stronger function of crystal size for cobalt than iron, and iron than nickel. This is of particular importance in applications such as data storage where extremely high aspect ratio

materials with a tunable electrical conductivity as well as a tunable magnetic coercivity could be of great use.

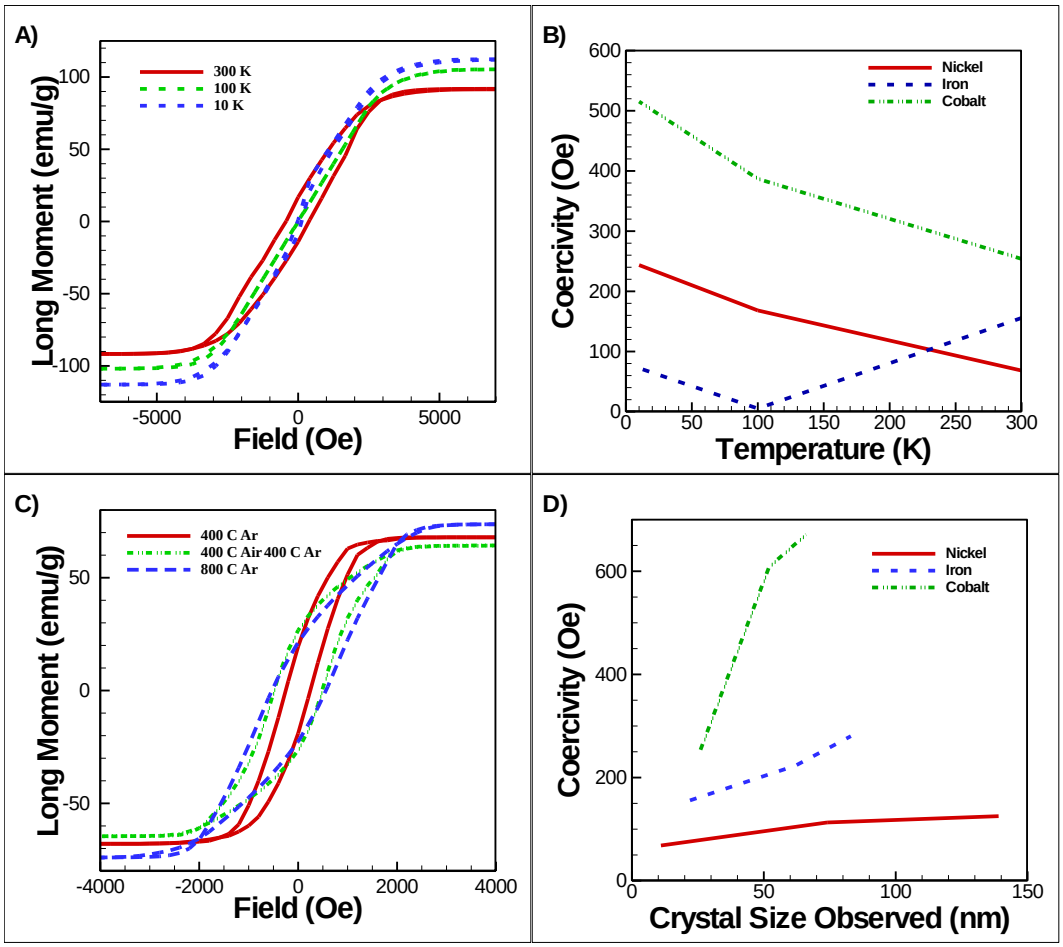

Figure 32. Magnetic properties of pure metal electrospun nanofibers as characterized under SQUID. (a) Iron nanofibers calcined through thermal treatment one characterized under SQUID at 300 K, 100 K, and 10 K. (b) Coercivity values calculated from data presented in Figure 4a and similar figures for cobalt and nickel plotted versus the temperature. (c) Room temperature variable field SQUID scans for cobalt nanofibers calcined at three different thermal treatments to produce various crystal sizes. (d) Coercivity data calculated from Figure 4c and similar for iron and nickel plotted versus the observed crystal size from TEM image analysis.

Beyond a single component nanofiber system, the composition of these nanofibers can be tuned to create a dual phase material by introducing two different precursors to create a substrate matrix and discrete domains of a secondary material. This could be useful in creating a magnetically active, but electrically insulating one-dimensional materials. Here a ceramic precursor, either aluminum or zirconium acetate, and a metal precursor, nickel acetate tetrahydrate, were used to generate a majority ceramic phase with small discrete domains of metal. This thereby adds an additional control to tune the size and density of the crystals produced.

Figure 33 presents TEM images of the resultant nanofibers as well as the magnetic properties of the resultant nanofibers as found by SQUID. Figure 33a and 33b are the TEM images of nickel nanocrystals in alumina and zirconia nanofibers, respectively. Figure 33c presents three constant temperature variable field scans of zirconia nanofibers with nickel nanocrystals displaying near superparamagnetic behavior at room temperature with growing coercivity as temperature decreases. Figure 33d presents the coercivity of both alumina and zirconia with nickel nanocrystals plotted against the temperature. In both cases, near superparamagnetic behavior is found at room temperature with growing coercivity as the temperature lowers. However, in neither case was a blocking temperature found through low field variable temperature scans, potentially due to the inhomogeneity of nanocrystal size.

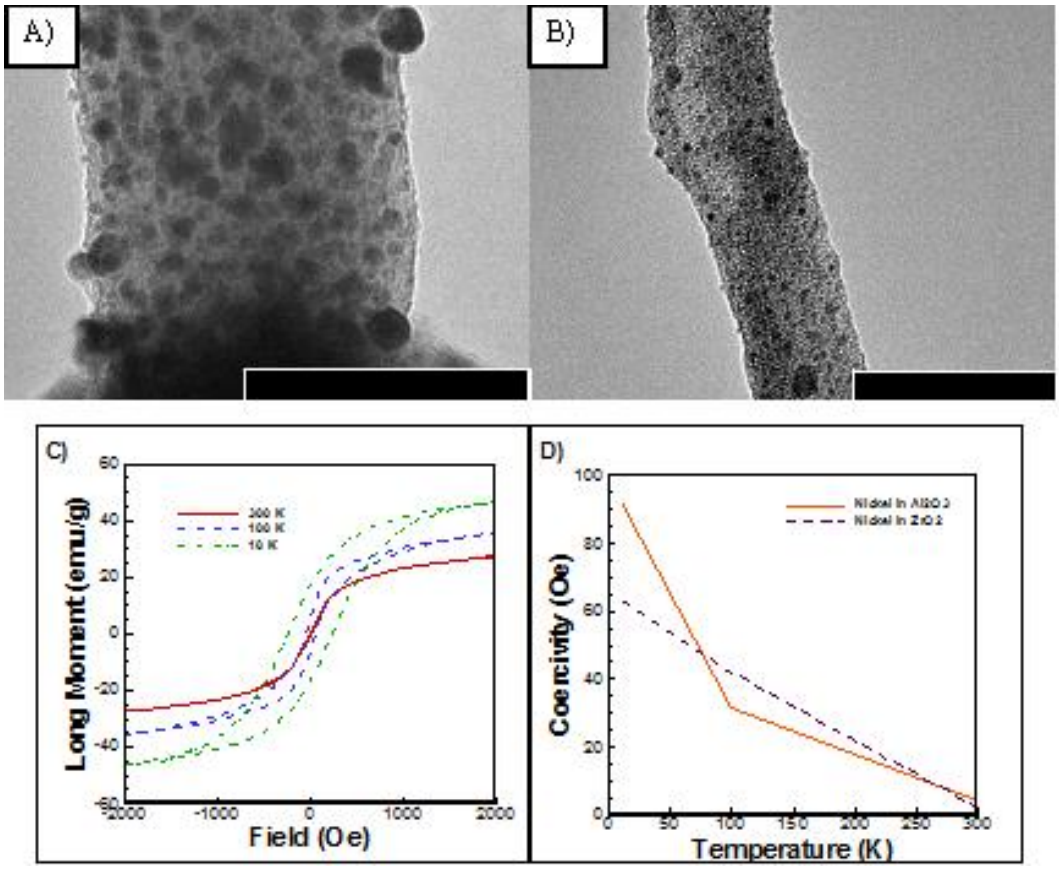

Figure 33. Dual phase nanofibers produced by including two precursors in electrospinning solution and their magnetic properties. TEM images of nickel nanocrystals supported in (a) alumina and (b) zirconia nanofibers. (c) Three constant temperature variable field scans conducted on nickel supported in zirconia using SQUID presenting the moment versus the applied field showing near superparamagnetic behavior at room temperature with growing hysteresis as temperature decreases. (d) Coercivity data as calculated from Figure 5c and similar data for nickel supported in alumina displaying ultra-low coercivity values at room temperature with growing coercivity as temperature decreases. Scale bar is 100 nm.

4. Conclusions

In summary, a purely water based approach has been used to electrospin nanofibers comprised of polyvinyl alcohol and metal precursors with a precursor to polymer mass ratio of 4:1. Various thermal treatments were subsequently used to control the crystal size and density in the nanofiber following removal of the polymer,

which in turn allows the control of the electrical and magnetic properties. The electrical conductivity of 10^6 to 10^7 S/m reported here are among the highest values reported for one-dimensional nanomaterials, due to the ability to generate large interconnected crystals with minimal amorphous regions in extremely high aspect ratio materials. Amorphous metal domains are found with mild thermal treatments and in turn reduce the electrical conductivity greatly. The magnetic properties with respect to temperature fluctuations display similar trends as reported previously, with the exception of iron displaying near superparamagnetic behavior at moderate temperatures potentially due to the balance of the amorphous and crystalline thermal expansion coefficient allowing for the crystal to align with the field at this temperature. Due to the high loading of the metal within the nanofibers, it is also found that the tuning of the crystal size greatly impacts the coercivity of the material with cobalt having the most significant size versus coercivity trend. Finally, two precursors were used simultaneously to create a dual phase material with the majority being an electrically insulating substrate and minority metal crystal domain. These magnetic properties display near superparamagnetic behavior at room temperature and growing coercivity with decreasing temperature for multiple substrates tested. This indicates that the water based electrospinning approach with high loading of metal precursors has the ability to create nanofibers with control of the crystal structure to control the electrical and magnetic properties simultaneously by controlling the composition of the nanofiber and the thermal treatment procedure.

CHAPTER 6

ALTERNATING LAYERS OF ALIGNED NANOFIBERS FOR LONG RANGE MAT MAINTENANCE

1. Introduction

Nanomaterials,[107] especially one-dimensional nanomaterials,[108] have garnered significant interest lately due to their exciting size dependent properties.[109-111] Electrospinning is one very advantageous method for generating one-dimensional materials because of its cost effective, scalable, and diverse nature which may have applications in membranes, filters, capacitors, electrodes, and many others.[29, 30, 105, 112] Purely inorganic metal or metal/ceramic nanofibers from a highly loaded water based system [91, 92, 113] have been generated in a number of morphologies, and seemingly bound only by the types of precursors and thermal treatments used. However, when these nanofibers mats are synthesized and thermally treated, the nanofiber mats curl or fracture, removing long range integrity of the nanofiber mat and thus decreasing the possible contribution of these materials to many applications. It is hypothesized that this is due to the volume reduction occurring during thermal treatment caused by the removal of the organic components and crystallization of the inorganic precursors. This volume reduction appears to occur not only in the radial but also in the axial direction potentially resulting in fiber curl or fracture. Here a "checkerboard" approach is proposed using alternating layers of aligned nanofibers [105] set perpendicular to each other to impede axial contraction thus increasing the radial contraction component while maintaining the flat, intact nanofiber mats over long distances.

2. Experimental Methods

Electrospun nanofibers are generated by mixing two solutions, the first an aqueous 10 wt. % solution of polyvinyl alcohol (PVA, 99.7% hydrolyzed 79 kDa) with the second, a 1:1:1 water: acetic acid: metal acetate by mass solution, in the proper ratio to create a polymer: metal mass ratio of 1:4. Subsequently a Harvard Apparatus PHD 2000 Infusion syringe pump at 0.005 ml/min and an electric field of 1 kV/cm generated by an HV ES3OP-5W power supply are used to generate proper conditions for electrospinning highly loaded water based nanofibers. Nanofibers are collected and aligned between separated copper collectors at a distance of 5 cm with each aligned layer consisting of 0.1 grams of nanofibers. Thermal treatment was conducted in a Neybox 1000ºC air furnace to remove organic components and crystallize the metal precursor. A Leica 440 SEM, a DI3100 AFM, and a Woollam Spectroscopic Ellipsometer are used to characterize the nanofiber and mat morphology and size.

3. Results & Discussion

A schematic presenting the approach for this "checkerboard" method is presented in **Figure 34.** Highly loaded precursor solutions are generated through the covalent bonding of polyvinyl alcohol (PVA) with metal acetate precursors [92, 113] and electrospun onto a split collector [105] to generate highly aligned nanofiber mats. 0.1 grams of nanofibers are collected on a free standing secondary collector aligned in the x direction, followed by 0.1 grams of nanofibers in the y direction, and so on until the desired number of layers is collected. Subsequently the nanofibers are taken to thermal treatment to remove the organic component and crystallize the metal precursors into purely inorganic nanofibers.

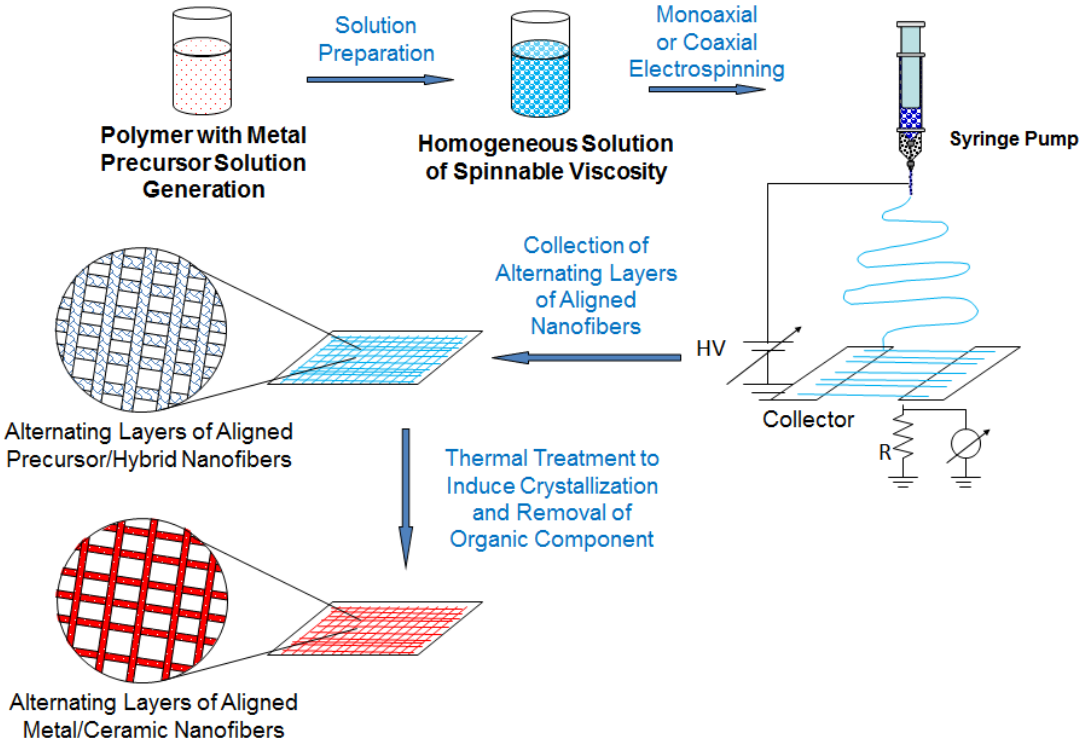

Figure 34. Schematic detailing electrospinning of water based nanofibers in alternating aligned layers followed by thermal treatment to remove organics and crystalize metal precursors.

To detail the effectiveness of this approach, atomic force microscopy (AFM), scanning electron microscopy (SEM), and ellipsometry were used to probe individual nanofiber morphology, overall nanofiber morphology, and macroscopic mat structure, respectively. These are presented in **Figure 35**. The AFM images of the isotropic nanofiber mats display randomly oriented nanofibers in the as-spun case and broken or curled nanofibers in the thermally treated case. However, the alternating aligned layers AFM images detail linear, aligned nanofibers with minimal curling or fracture observed in the as-spun and thermally treated cases. The SEM images further detail similar effects. The isotropic case displays a significant morphology change from the as-spun case, where a fairly uniform and linear nanofiber is observed on average, to the images after thermal treatment where the nanofibers are significantly curled and

broken – similar to the morphology change observed through AFM. In the mats with nanofibers aligned in alternating directions, however, it can be seen that the nanofibers, while sparsely populated to allow for viewing of the checkerboard approach are indeed oriented in a checkerboard approach. Further, this morphology is maintained following thermal treatment with no curling or breakage seen. Inlaid are SEM images of highly populated nanofiber mats. While only one direction of alignment is viewable in these images due to the high population, it can be seen that the linear structure of the nanofibers are indeed maintained through thermal treatment.

The morphology fluctuation observed in the isotropic nanofiber mats has long range effects in the nanofiber mat structure. This shift was probed by sputter coating the nanofiber mats to increase reflectivity and using ellipsometry to probe the surface normal direction at 100 points evenly distributed in a 10 by 10 grid format on each 5 cm by 5 cm nanofiber mat. These images display the significant improvement in nanofiber mat structure afforded by the "checkerboard" approach. As can be seen, the isotropic mat is initially fairly flat with ~2 degrees as the maximum offset angle. However, upon thermal treatment these nanofibers curl significantly, mostly at the edges, resulting in a decrease in mat integrity. This is in great contrast to the nanofibers generated through the "checkerboard" approach where extremely flat surfaces with a maximum offset angle of ~1 degree is observed in the as-spun case and retained through thermal treatment when the maximum offset angle only increases to ~3.2 degrees. Therefore, this approach has maintained long range mat integrity by decreasing the nanofiber curling or fracturing seen in isotropic cases.

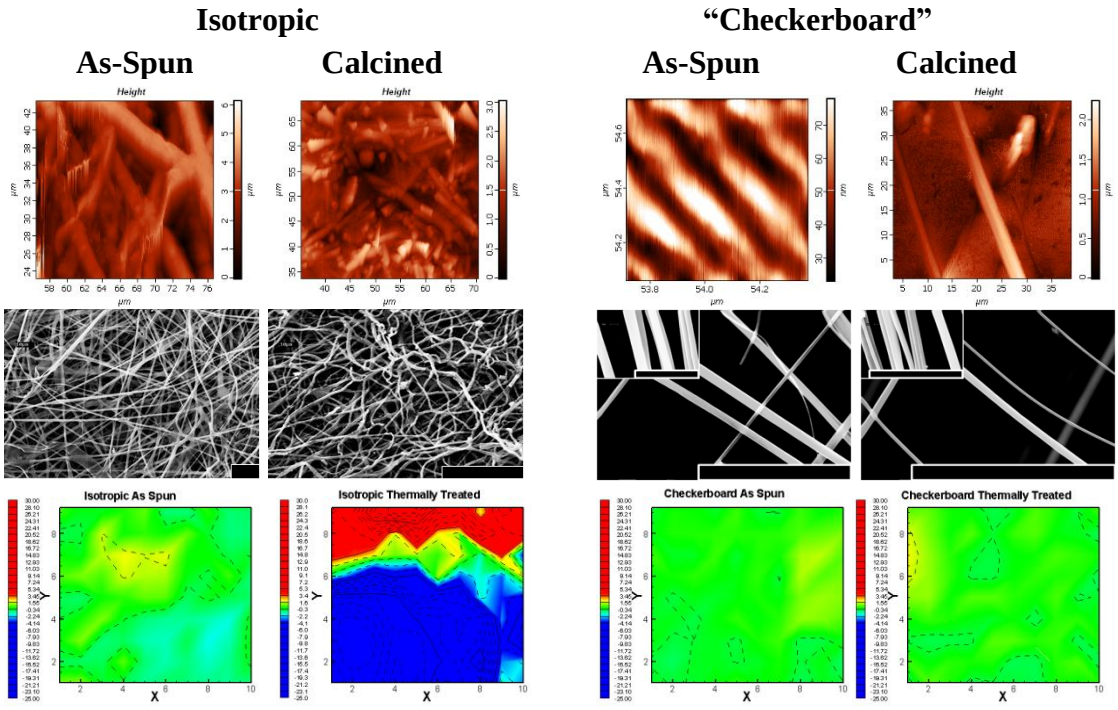

Figure 35. AFM, SEM, and ellipsometry data presented for isotropic and checkerboard nanofiber mats as spun and thermally treated detailing the curling and breakage in isotropic mats resulting in nanofiber mat integrity loss, while the maintenance of long, linear nanofibers afforded by the checkerboard approach maintains long range, flat, nanofiber mat integrity. Scale bar is 10 microns.

To further understand the mechanism of the mat maintenance, the average nanofiber length and the average volume fraction remaining following thermal treatment were calculated from the AFM and SEM images. These are displayed in **Figure 36**. The average nanofiber length was found for samples of isotropic morphology, a single aligned layer, and "checkerboard" samples of three, five and seven total layers for nickel oxide, zinc oxide, and an amorphous alumina sample for comparison by tracing the length of 50 individual nanofibers through SEM. As can be seen the length of the isotropic crystalline nanofibers are an order of magnitude shorter than the non-crystalline alumina material. This is due to the axial breakage of the nanofibers as seen through AFM in Figure 34. The average length of the

nanofibers further decreases when a single aligned layer is viewed, perhaps due to a similar breakage mechanism as with the isotropic mat. However, when the "checkerboard" approach is applied the average nanofiber length steadily increases until it approaches the length observed for the amorphous material. It is hypothesized that the original decrease in nanofiber length is caused by axial shrinkage during the volume reduction associated with removal of the organic component and metal crystallization during thermal treatment. Thus the nanofiber mat contracts in on itself resulting in the breaking and curling of nanofibers observed through AFM and SEM, which results in the destruction of mat integrity observed in ellipsometry. However, the alternating nanofiber layers may inhibit the axial shrinkage and contraction upon thermal treatment by offering perpendicular support through the alternating aligned layers given by the "checkerboard" approach. Thus the length of the fibers observed is maintained increasing the long range mat structure.

Figure 36b presents the average volume fraction radially remaining after calcination for isotropic and "checkerboard" nanofibers samples. Various metals, metal oxides, and ceramics were tested with the radial reduction calculated based on the average as spun nanofiber diameter and the average nanofiber diameter calculated following thermal treatment. As can be seen, there is a significant and consistent decrease in the radial volume fraction remaining in the "checkerboard" approach, which implies that there is a significantly higher contraction in the radial direction. If it is assumed that there should be a similar overall volume reduction due to the removal of organic components and crystallization of inorganic components consistent between the isotropic and "checkerboard" samples, the only difference should be the fraction of volume reduction that occurs radially or axially. Since there appears to be an enhanced radial reduction through the checkerboard approach, as well as a longer overall nanofiber length observed, it would follow that there would be a decrease in

the axial contraction. It makes sense, then, that this would result in a decrease in curling and a decrease in nanofiber fraction, which in turn would enhance the long range, flat, nanofiber mat integrity.

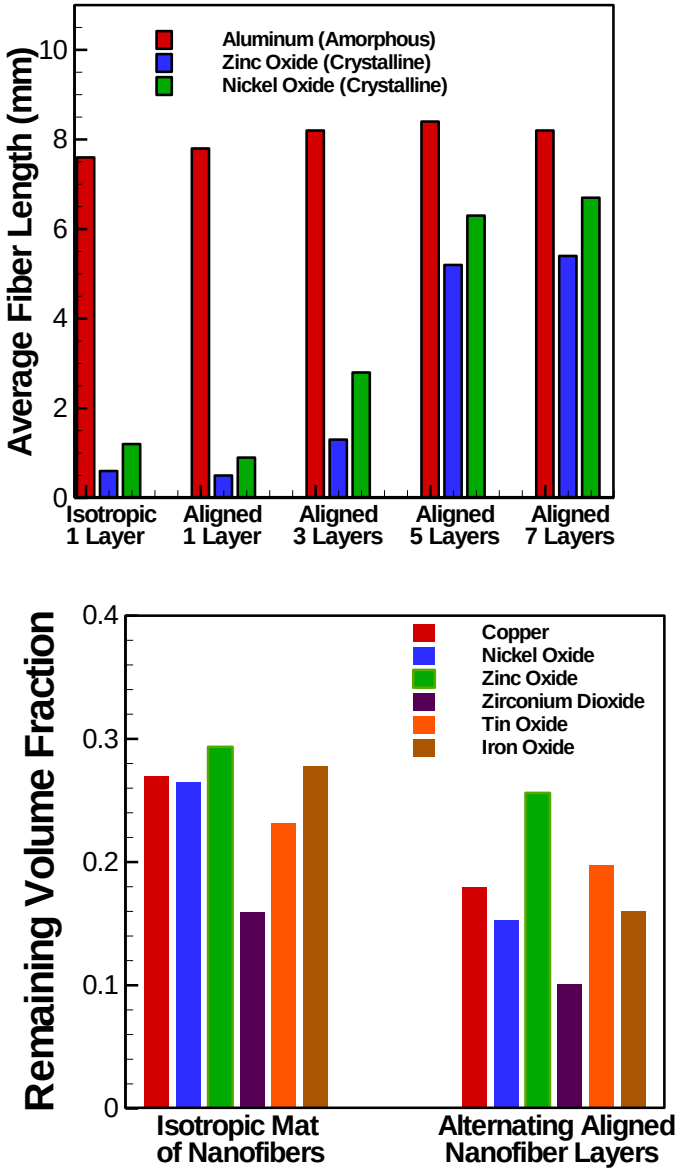

Figure 36. Graphical representation of the maintenance of nanofiber length due to layering aspects for ZnO and NiO nanofibers versus a non-crystalline alumina nanofiber. Further, the increase in radial volume reduction within the checkerboard approach versus the isotropic approach may indicate a decrease in axial volume reduction corresponding to less nanofiber breakage, and thus longer nanofibers.

4. Conclusions

In summary, we have presented an approach to align alternating layers of electrospun nanofibers in a "checkerboard" fashion. Through AFM, SEM and ellipsometry it can be seen that the isotropic mats due indeed suffer from significant curling and breakage following thermal treatment and that this results in significantly curled and broken nanofiber mats over the range of many centimeters. However, by aligning alternating layers of nanofibers through a checkerboard approach, the nanofibers do not suffer curling or breakage which results in a stable, flat, maintained nanofiber mat over the same centimeter long range. Further, the radial volume reduction appears to be enhanced in the checkerboard approach versus the isotropic mat case, which would result in a decrease in the axial contraction and thus a decrease in curling and breakage. All of these results indicate that aligning alternating layers of nanofibers increases the mat support following thermal treatment, which is crucial for the application of any of these nanofibers in real world application of these electrospun metallic nanofibers as electrodes, membranes, filters, capacitors, and many others. This method, when combined with the cost-effective and scalable process of water-based electrospinning from highly loaded solution of precursor nanofibers, as well as the diversity of materials able to be produced by electrospinning, displays a tremendous platform to generate materials with very exciting chemical, physical and electrical properties to solve real world problems in a range of applications from energy and fuels, to sensing and protective clothing, to selective filtration.

CHAPTER 7

INORGANIC ELECTROSPUN NANOFIBERS FOR ANODIC MATERIALS IN LITHIUM ION BATTERIES

1. Introduction

Lithium ion batteries have long been identified as an exciting, safe and efficient method to store and use energy.[114, 115] Electricity is stored by utilizing the transport and incorporation of lithium ions from the cathode to the anode via an electrolyte during charging, and from the anode to the cathode during use.[116] The amount of energy able to be stored, therefore, is a strong function of the amount of lithium able to be transferred to and from anode. When transferred to the anode, the lithium ions are incorporated into the anodic material itself through the process of lithiation, indicating that the intercalation parameter of lithium into each material strongly dictates the theoretical capacity of each material.[117] A list of theoretical capacities, as well as the corresponding volume expansions, is included later as **Table 6**. Lithium ion batteries utilizing high theoretical capacity materials have been identified as having many potential advantages that include high theoretical energy densities, high power densities allowing for fast charge/recharge rates, and long life spans of materials surviving hundreds of charge/discharge cycles.[118, 119]

However, high theoretical capacity bulk materials have difficulty being used in practice. During the process of lithiation, large quantities of lithium are transferred from the cathode to the anode. Upon their insertion into the anode, a large volume expansion occurs in the anode – up to 400% of the original anodic volume - first at electrolyte/anode interface. This large volume expansion at the surface while maintenance of original structure at the core results in a large hoop stress within the

anodic material, often resulting in a material fracture termed pulverization. This has long prevented high capacity anodes from being utilized in industry.[120] Due to this, the industry standard anodic material is a carbon anode due to its ability to allow for respectable capacities (~300-400 mAhr/g) while surviving many cycles in the same morphology without pulverizing.[121] This long lifespan is due mostly to the small volume expansion of only about 5% the original volume.

Material	**Theoretical Capacity (mAh/g)**	**Volume Expansion**
C	342	~5 %
SnO_2	1020	~320%
Co_3O_4	890	~220%
Ge	1800	~300%
Si	4200	~420%

Table 6. Tabulated values for the volume expansion and corresponding theoretical capacity data for a few interesting anodic materials are presented.

However, this capacity is very low and needs to be greatly increased to allow for the increased productivity of lithium ion battery technology. It has been shown that the use of nanomaterials can allow for a decrease in the pulverization phenomenon by decreasing one or more of the length scales so that when incorporating large volumes of lithium, the crystal has the opportunity to swell uniformly without fracturing decreasing the strain described previously.[122] Many companies currently are investigating the use of nanomaterials in lithium ion batteries, such as A123 Systems, which is using a slurry of nanoparticles.[123] However, due to the instability associated with these structures and the difficulty of maintaining contact

with the charge collectors, one-dimensional materials have been investigated to increase the stability and the contact between these materials, resulting in higher electron transfer.[124, 125] Metal oxides, metal sulfides, and high capacity germanium and silicon have been synthesized through a variety of methods and demonstrated to have high capacities over a moderate number of cycles.[126, 127] However, these materials are typically synthesized from expensive methods that are only able to produce mg/day not allowing for easy scalability to an industrial synthesis procedure.[128] Therefore, here highly loaded water based electrospinning has been used to generate pure metal oxide nanofibers [92, 113, 129] as anodic materials for lithium ion batteries. A standard coin style half-cell has then been used to characterize their capacity over many cycles. Further, materials with high theoretical capacities (germanium and silicon) have been synthesized in pure nanofiber form, and materials have been placed in a supporting matrix to further increase their stability during intercalation. These materials are under ongoing battery testing.

2. Experimental Methods

Highly loaded water based electrospinning has been used to synthesize precursor nanofibers using various metal acetate salts, as described previously. Nanofibers are generated by electrospinning highly loaded solutions consisting of aqueous 10 wt. % PVA (99.7% hydrolyzed, 79 kDa), *x* grams metal acetate, *x* grams acetic acid, and *x* grams H_2O where *x* is chosen to create a 4:1 mass ratio of metal acetate to PVA. Electrospinning is conducted using a Harvard Apparatus PHD 2000 Infusion syringe pump at 0.005 ml/min and an electric field of 1 kV/cm generated by an HV ES3OP-5W power supply, with nanofibers collected on a grounded collector plate and taken for thermal treatment under a LabTemp 2 Zone 1700℃ tube furnace or a Neybox 1000℃ box furnace depending on the atmosphere of testing. Thermal

treatments that have been used vary greatly depending on the metal and oxidation state, as detailed in **Table 7**. The structure and morphology of the resulting nanofibers are characterized using SEM, TEM, EDAX, and XRD as detailed previously. Following characterization, these materials are then taken for battery testing using a coin cell half-cell setup as purchased from Hohsen Batteries using lithium metal as the cathodic material.

3. Results & Discussion

Highly loaded water based electrospinning was used with various metal precursors to synthesize pure metal oxide nanofibers. **Figure 37** presents TEM images and XRD patterns (inlaid) of some metal oxide structures that were synthesized, but not an exhaustive list of those made and tested. Top left is a TEM image of reduced tin nanocrystals, as confirmed by the inlaid XRD image, supported within an amorphous tin oxide matrix which was confirmed by EDAX. This was done in an effort to compare incorporating nanomaterials within a matrix versus its purely metallic counterpart. The performance of these will be discussed further later. Top right is a TEM image of a purely crystalline tin oxide nanofiber comprised of ~5 nm tin oxide crystals, also confirmed by the inlaid XRD, connected to form continuous nanofiber structures. Bottom left details a Co_3O_4 nanofiber composed of larger ~40 nm crystals interconnected to maintain nanofiber morphology shown by the large peaks in the XRD inlaid. Finally, similar to the Co_3O_4 nanofiber, the bottom right presents a Fe_3O_4 nanofiber comprised of many larger interconnected crystals and its corresponding XRD pattern. Similar structures were created in Fe_2O_3, Cu_2O, SnO, and others. The thermal treatments used to generate these nanofibrous structures are presented in **Table 7**.

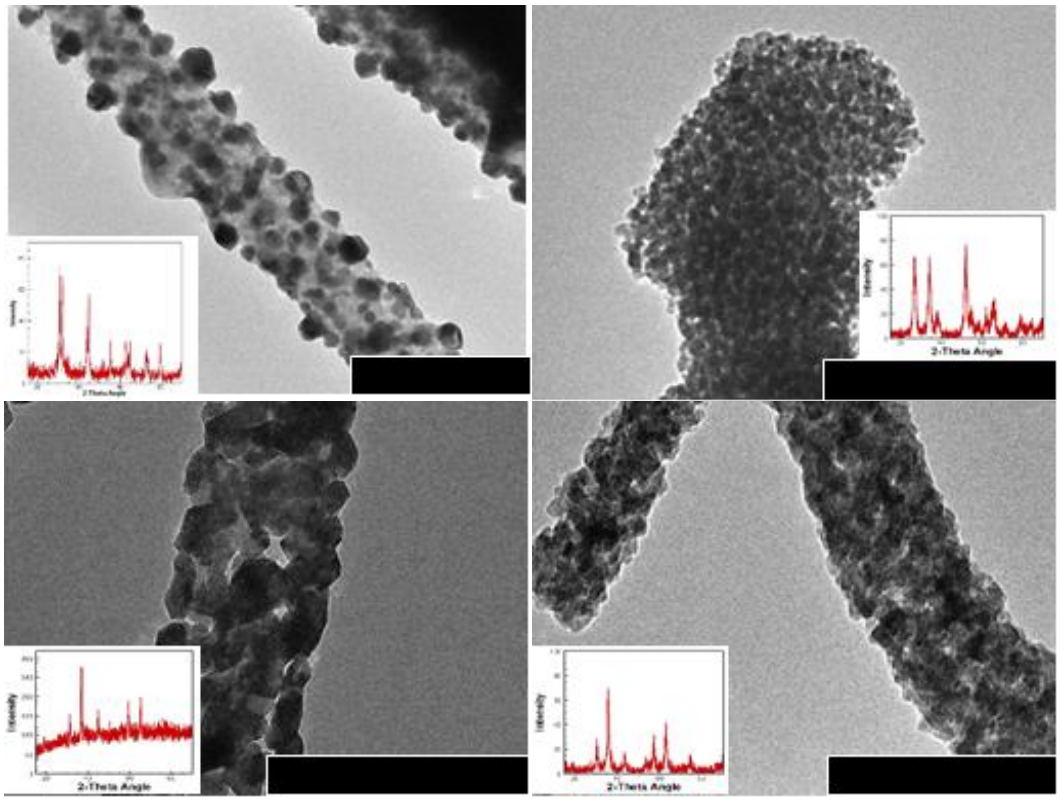

Figure 37. TEM images and XRD graphs (inlaid) of representative metal oxide nanofibers tested as anodic materials. Reduced tin (Sn) nanocrystals are supported within an amorphous tin matrix (top left), purely crystalline tin oxide (SnO_2) with small crystal diameters (top right), purely crystalline Co_3O_4 (bottom left), and purely crystalline Fe_3O_4 (bottom right) are some of the metal oxides tested.

These structures, while comprised of similar elements as the one dimensional metal oxides detailed previously,[126] have a uniquely different morphology being composed of many smaller crystals rather than a single, unidirectional crystal which the template and catalytic growth mechanism are able to produce. This multi-crystalline structure, when applied as anodic materials in the lithium ion battery setup, could have the added benefit of having "pores" where structures could expand into without fracturing. Further this could allow for greater electrolyte access allowing faster charge transfer. However, it could suffer from mechanical failure as pinch points are formed where crystals attempt to swell and joints are forced to bend and fracture.

Nanofiber Structure	Heating Rate	Maximum Temperature	Atmosphere	Cooling Rate
Fe_2O_3	5 ℃/min	800 ℃	Air	5 ℃/min
Fe_3O_4	5 ℃/min	500 ℃	Air	Quench
Co_3O_4	2 ℃/min	500 ℃	Air	Quench
Cu_2O	5 ℃/min	800 ℃	Air	5 ℃/min
SnO_2	5 ℃/min	900 ℃	Air	2 ℃/min
Purely Crystalline Sn	2 ℃/min	800 ℃	Argon/H2	2 ℃/min
Sn in Amorphous Sn	2 ℃/min	450 ℃	Argon	2 ℃/min

Table 7. Thermal treatment conditions, including heating rate, cooling rate, atmosphere, and maximum temperature to generate metal oxide nanofibers of various composition, morphology, and oxidation states.

These metal oxide materials' performance as anodic material is presented in **Figure 38** as the fraction of the theoretical capacity (mAh/g) observed versus the cycle number. High capacity, single crystalline one-dimensional materials perform at a fractional theoretical capacity of 30-40%.[125] As can be seen, quite a few show relatively good performance over a low number of cycles. Fe_2O_3, as a pure metal oxide, especially appears to maintain reasonably high performance about 35% until cycle number 50. Further, reduced tin crystals supported in an amorphous tin matrix appear to have extremely exciting properties. The fractional theoretical capacity shows very high capacities until cycle number 44 where the material steeply declines to nearly zero in a matter of 3 cycles. This could be due to a number of phenomenon, that as of yet haven't been confirmed. The tin crystals could be forced out of the amorphous tin oxide matrix due to their swelling and shrinking during cyclization thereby decreasing the crystalline stability. Also, some materials have shown

reactions with electrolytes previously,[123] which could deactivate the material. However, this support mechanism appears to greatly outperform the purely crystalline tin nanofiber tested, which provides some insight into how to synthesize high capacity materials that may avoid pulverization over many cycles.

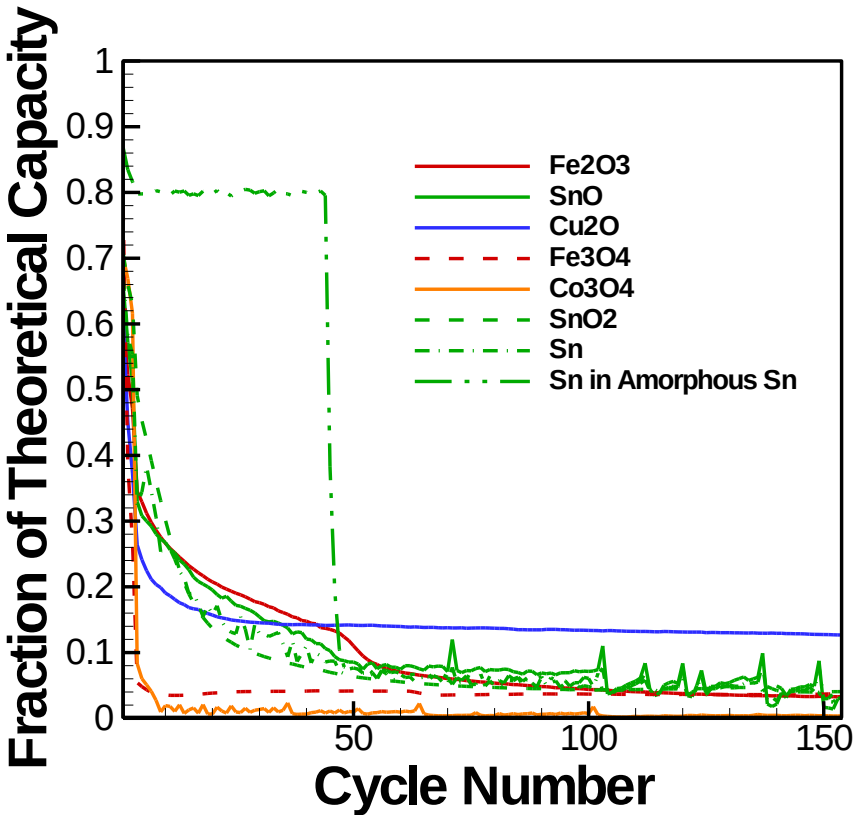

Figure 38. Graph of capacity versus cycle number for many metal oxides tested. As can be seen, capacity drops quickly for all nanofibers displaying pulverization potentially due to the numerous small crystals with minimal growth direction observed above.

TEM images and XRD graphs (inlaid) are presented in **Figure 39** detailing the composition, crystal structure, and morphology produced for high capacity nanofibrous materials both supported in a matrix and as a pure nanofiber. High capacity materials, such as purely inorganic, crystalline germanium and silicon nanofibers have been synthesized by highly loaded water based electrospinning with prefabricated nanopowders (nanoparticle diameter <100 nm) as purchased.

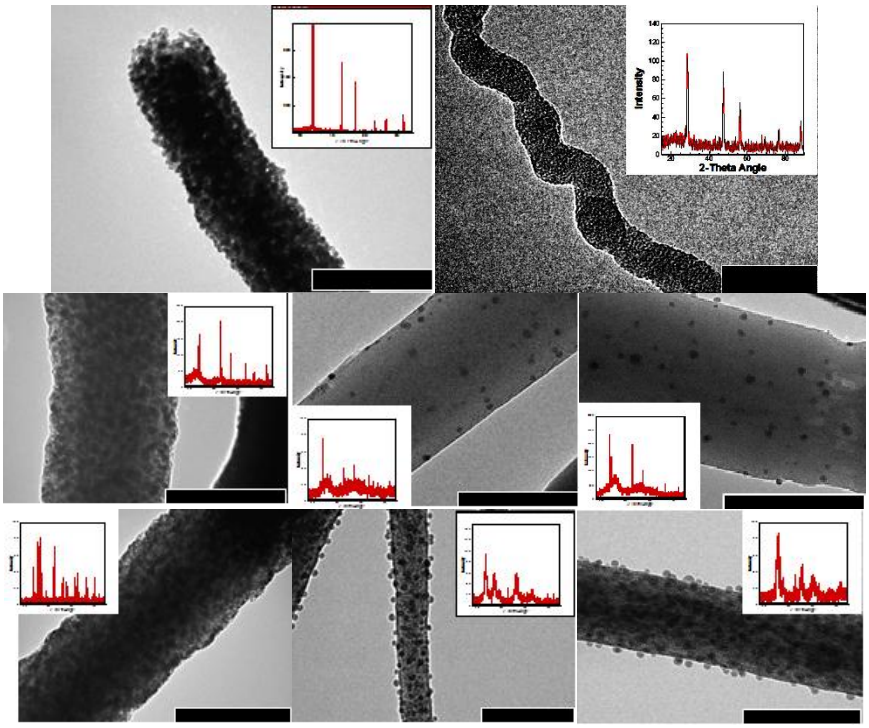

Figure 39. TEM Images and XRD of high capacitance materials, including Germanium and Silicon pure nanofibers at top as well as Germanium and Tin each placed in a carbonized PAN, alumina, and zirconia, matrix to decrease pulverization effects and increase material stability. These are currently in battery testing. Scale bar is 200 nm.

By heating and mixing in concentrated acetic acid, followed by drying, these nanopowders show similar bonding characteristics with PVA as the precursor approach. Through this method, it can be seen that germanium nanofibers have been synthesized consisting of ~7 nm germanium crystals interconnected. Silicon nanofibers have also been fabricated and appear to be of uniform, nearly single crystal fiber diameter. Further, to increase stability and decrease pulverization, tin and germanium have been placed within a supporting matrix. Both materials have been placed in alumina and zirconia at metal to ceramic mass ratios of 1:4. Also, to give insight into the effect of a more electrically conductive, porous matrix, germanium and tin have been placed in a poly-acrylonitrile (PAN) polymer solution. Subsequently the

PAN/metal nanofibers were heat treated to stabilize and carbonize the PAN and generate small metal crystals within a porous, electrically conductive carbon nanofiber.

Preliminary data corresponding to the use of these materials as anodes in half cell tests is presented in **Figure 40.** Others are ongoing and will yield more conclusive results as they become available. Of first note is the fact that pure silicon nanofibers appear to pulverize quickly. Within 3-4 cycles the fraction of the theoretical capacity has declined steadily to ~10 percent with the actual capacity hovering around 450 mAh/g. While this is still higher than the commonly used carbon anode, it does not present enough stability and energy density to be used broadly. Prefabricated germanium nanoparticles placed within alumina nanofibers do present very good stability. Over 100 cycles they present maintained capacities greater than 800 mAh/g. Similar capacities were also viewed when testing *in-situ* fabricated tin nanoctrystals within alumina nanofibers as these have achieved ~850 mAh/g for a few cycles. While the crystal size and density differed greatly from the germanium sample detailed previously, high stability was offered. Further, initially the capacity increased rather than decreasing due to material loss and pulverization. This could be due to the high stability offered by this process decreasing the material loss as well as the need for these insulating nanofibers to come in great contact with the charge collector, and therefore after a few cycles this contact has been made more thoroughly. With both tin and germanium, it is hypothesized that the high capacity could be due to the small crystal size of the materials placed within the alumina matrix, but also the flexibility of the non-crystalline nanofiber matrix allowing for the volume change of each nanoparticle without fracturing the nanofiber itself. However, there are still further improvements that could be made to this alumina system. An increase in nanofiber porosity would allow for greater crystalline – electrolyte contact and therefore

potentially allow for greater ion transfer. Further, an increase in nanofiber electrical conductivity would allow for greater charge/discharge capabilities. To this end, a PAN nanofiber was used with pre-synthesized germanium nanoparticles and tested in an identical half-cell test. As can be seen, very high capacities are achieved through this system with the initial plateau occurring around ~1000 mAh/g. It appears as though this may be a very attractive option to generate nanofiber anodic materials through electrospinning. Further improvements that could be made will be discussed in Chapter 9.

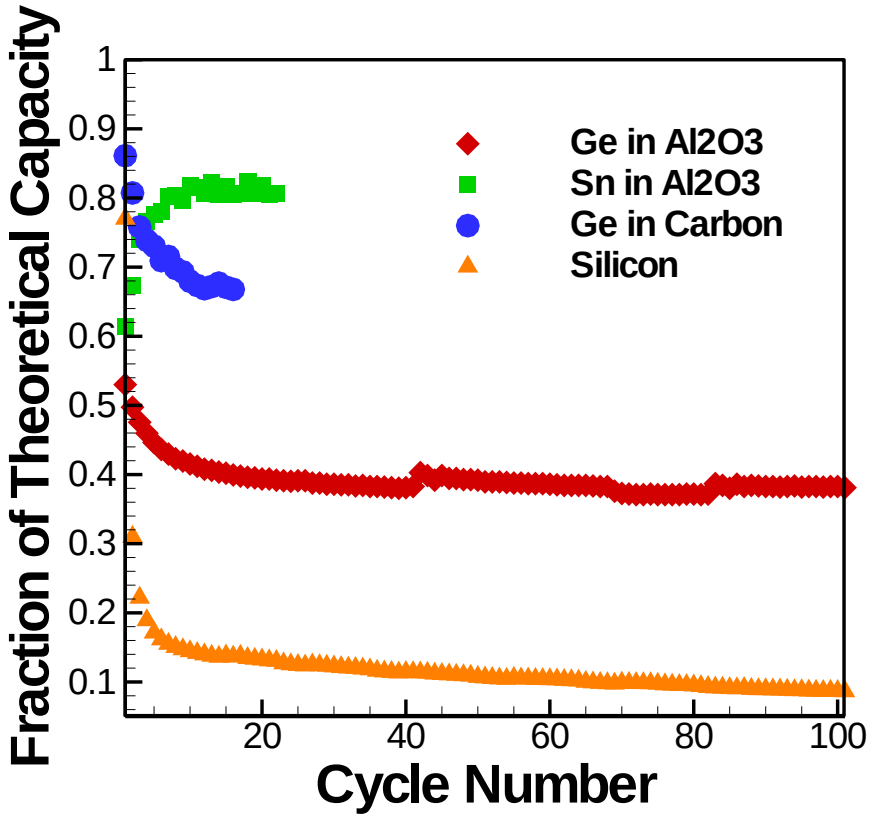

Figure 40. Preliminary capacity data is presented for pure silicon, germanium within alumina and carbon, and tin within alumina corresponding to new high capacity nanofiber materials that were presented in Figure 39. Data is presented as the fraction the of theoretical capacity for the pure material.

4. Conclusions

In summary, purely inorganic nanofibers have been synthesized by the highly loaded water based electrospinning method. A number of metal oxide nanofibers, including Fe_2O_3, Fe_3O_4, Co_3O_4, Cu_2O, SnO_2, Sn, SnO, and Sn supported in an amorphous Sn matrix have been synthesized. These display reasonable capacities over a short number of cycles, but quickly pulverize – potentially due to their brittle crystalline structure without directional growth. To increase capacity, different materials have to be used with a greater intercalation coefficient. Two such materials are germanium and silicon, and have been synthesized in the pure nanofiber form. Further, to help increase stability and thus decrease the pulverization effect seen after many cycles, high capacity materials are placed as small nanocrystals within a nanofiber support matrix. Various matrices are tested including Al_2O_3 and ZrO_2 from the highly loaded water based electrospinning method, but also carbonized PAN from a standard electrospinning method to test the need for an electrically conductive nanofiber backbone. These nanofibers display strong XRD peaks, highly crystalline crystals, and good fiber morphology and are currently under battery testing now. Preliminary results pertaining to these materials demonstrate that they have great capacity and stability (~1000 mAh/g) over many cycles (100) when contained within a secondary matrix. Further, this capacity is increased when a more electrically conducting and porous nanofiber matrix is used. Many future works pertain to this project and are detailed in Chapter 9.

CHAPTER 8

INORGANIC ELECTROSPUN NANOFIBERS FOR THIN FILM PHOTOVOLTAIC DEVICES

1. Introduction

Photovoltaic devices, while representing little of the current energy production due to expensive production and relatively low efficiency,[130] have been investigated in a number of forms due to the benefit of long term, on site renewable energy.[131] First generation photovoltaic solar cells consist of p-n junctions and are typically manufactured as single crystalline silicon.[132] These materials, while the most popular technology industrially, are plagued by low efficiencies,[133] high manufacturing,[134] shipping, and installation costs.[135] Second and third generation photovoltaic devices represent the potential to overcome these drawbacks. Second generation devices, while still bound by the theoretical maximum efficiency of 41%,[136] employ thin film technology to allow for a less expensive process with similar or greater efficiencies. Third generation materials in particular, due to the ability to increase efficiency even beyond the 41% efficiency by using various materials and sizes, junctions, and geometries, could produce not only a more attractive option but an option that produces energy at a price competitive or even more economical than fossil fuels.[137]

Typical thin film solar cells, both second and third generation, consist of at least 5 layers.[134] Moving from the backing to the front (or top) of such a 5 layer cell, the first layer is a backing electrode followed by a selective charge transport layer, the photovoltaic material itself, an additional charge transport layer selective to the opposite charge from the previous layer, and the top electrode.[138] The

photovoltaic material, when struck by a photon of high enough energy, can absorb that energy and promote an electron to the conducting band. The electron and resulting hole need to then be selectively transferred in opposite directions to avoid recombination, with the electron being used for electricity on the way. One of the increases in efficiency within these next generation materials is the ability to tune the band-gap of photovoltaic nanomaterials by controlling their size. It has been shown that by controlling the diameter of photovoltaic material below a diameter where the size of the particle is on the order of the wavelength of the electron being promoted, the material is termed 'quantum confined'. By doing this, the band-gap of the material can be controlled by controlling the size of the material. Thus, when the band-gap is controlled, the wavelength of light it absorbs is controlled and the energy of the electron that is promoted is controlled. Therefore, more energy can be harvested from the same distribution of light.[139, 140]

Upon the promotion of the electron to the conducting band, the electron must move to the charge transport layer with its respective band-gap as controlled by material selection, move through that layer and to that electrode. Similar transport mechanisms must be used for the holes as well.[141] The materials currently used for these charge transport layers are very diverse, but are chosen to have selective band gaps so as to absorb only the electrons or holes selectively while having high electrical conductivities. In this way, there is a directed circuit allowing for higher efficiency by decreasing the recombination effects that can be felt through the transport layers. Currently, spin coated PCBM and PEDOT are common transfer layers due to their high conductivities, well understood geometry and ease of fabrication through spin coating.[142] However, both of these materials suffer from being expensive and thermally unstable.[143] Therefore, metal oxide nanoparticles – most notably ZnO and NiO – have been investigated to replace these due to their stability and proper

band-gap.[144, 145] A schematic of the charge transfer flow and corresponding band gap analysis for each of the materials in a typical thin film photovoltaic device is presented below in **Figure 41**.

These nanoparticle charge transport layers, though, are plagued by a different set of problems. First, uniform thin layers are difficult to generate and maintain in a compact, stacking structure. Second, layers constructed of nanoparticles require hopping a charge transport mechanism, which is an inefficient transport mechanism and can allow for recombination at the photovoltaic – charge transport layer interface. This results in relatively low electrical conductivities, typically around 7000-8000 S/m.[146] Therefore, to limit this hopping mechanism, one dimensional metal oxides have been used by some to eliminate the inefficient hopping requirement within the charge transport layers [147] by allowing the charge to transfer to the one dimensional material, and subsequently transfer directly through the materials' axis to the electrode. This is reported to increase the electrical conductivity of the transport layer and thus increase the cell efficiency, but it does make the cell less cost effective due to the increase in expensive nanomaterial synthesis and an increase in complicated nanomaterial orientation.[148] Also included below in Figure 41 are schematics detailing the nanoparticle and one-dimensional charge transport layers incorporated into thin film photovoltaic devices.

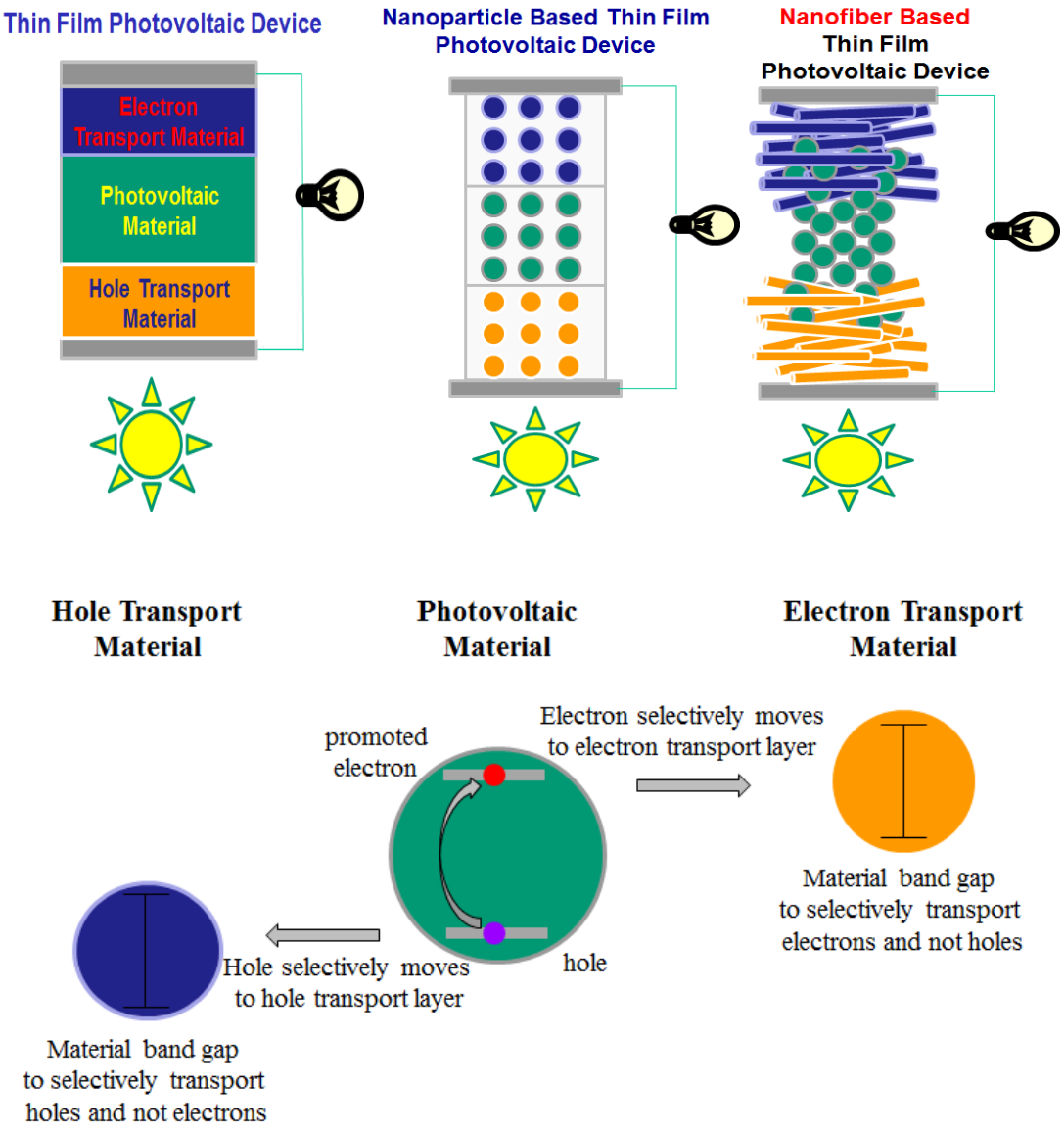

Figure 41. Schematics detailing the typical film photovoltaic structure, thin film photovoltaic devices including nanoparticle charge transport layers as well as one dimensional material transport layers are presented. A schematic showing the promotion and charge transfer elements within such a device is also included.

Here, highly loaded water based electrospinning [92, 113] has been employed to generate mats of purely crystalline ZnO and NiO with high electrical conductivities. The "checkerboard" approach [129] has been used to generate long range mat integrity so that direct thermal treatment and inclusion in a thin film solar cell could be

generated and eliminate post thermal treatment processing such as sonication and spin coating. These materials, while presently not included in photovoltaic devices, demonstrate properties that make them very promising materials. Further, pure PbSe nanofibers have been generated through the highly loaded water based electrospinning approach. The average crystal size and nanofiber structure has been shown to be controlled by the thermal treatment conditions. However, until now the thermal treatment conditions haven't been able to generate PbSe of small enough diameter to be quantum confined.

2. Experimental Methods

Electrospun nanofibers are generated from the highly loaded water based approach where an aqueous 10 wt. % PVA solution is mixed with a 1:1:1 solution of metal acetate, water, and acetic acid in a ratio such that a 1:4 PVA: metal acetate ratio by mass is generated. Electrospinning occurs using a Harvard Apparatus PHD 2000 Infusion syringe pump flowing 0.005 ml/min through a 22 gauge needle where it is met by an electric field of 1 kV/cm generated by an HV ES3OP-5W power supply. Nanofibers are collected between a split-collector with a spacing of 5 cm in an alternating aligned layer approach as detailed previously. Each layer is 0.1 g of PVA/metal acetate hybrid nanofibers, and following the proper alternating layered structure generation, the nanofibers are taken for thermal treatment in a LabTemp 2 Zone 1700˚C tube furnace or a Neybox 1000˚C box air furnace depending on the atmosphere of testing. Following thermal treatment, SEM, TEM, and XRD are used to characterize the resulting nanofibers as discussed previously, while the electrical conductivity is tested using a standard 2 point probe following ASTM standards. The average crystalline diameters are calculated based on both XRD patterns with the Scherrer Equation as well as by TEM size observation.

3. Results & Discussion

Similar to the construction of the alternating aligned layers of nickel oxide nanofibers discussed previously in Chapter 6, nickel oxide nanofibers were generated with a number of different layers using the same split collector approach. Further, similar structures were generated from zinc oxide nanofibers. SEM images were taken to confirm the nanofiber mat morphology and were very similar to the structures presented previously. TEM images were also taken and XRD patterns confirm the purely crystalline nanofiber morphology. These are displayed in **Figure 42**. This purely crystalline structure, as discussed in Chapter 5, is crucial for high electrical conductivities, but it is also crucial to maintain the selective band-gap so that ZnO will selectively transport electrons and NiO will selectively transport holes to prevent possible recombination within the charge transport layers.

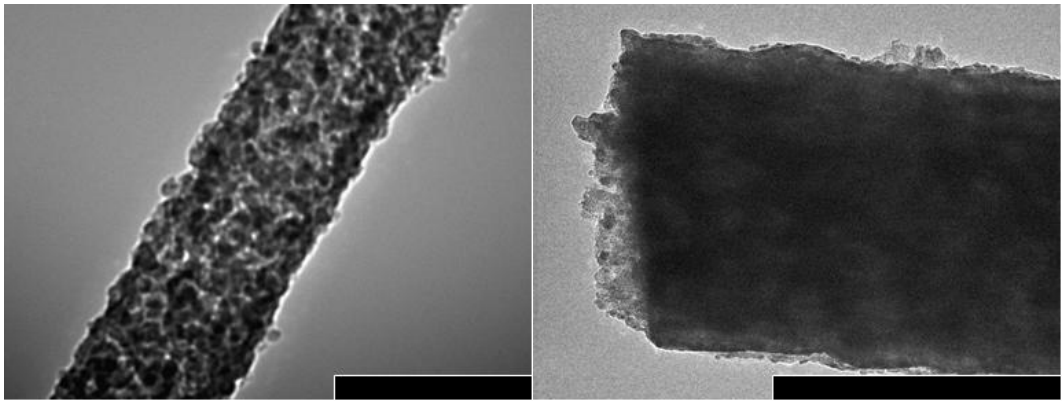

Figure 42. TEM images of purely crystalline ZnO (left) and NiO (right) nanofibers following thermal treatment at 500℃ for 1 hour and quenching to room temperature under air. Scale bar is 200 nm.

Following the generation of these ZnO and NiO purely inorganic nanofibers, the electrical conductivities were tested and presented in **Figure 43**. As can be seen, the electrical conductivities steadily increase with increasing number of nanofiber layers. This is potentially due to the increase in z-axis conductivity through the

nanofiber mat allowing for more conducting paths for electrons to move through the mat. However, it could also be due to the increase in nanofiber length associated with the increase in number of layers decreasing the axial contraction as reported previously in Chapter 6. Within the previous discussion, it was found that the nanofiber length increases steadily from 3 layers to 7 layers, which is where the electrical conductivity also increases. Perhaps this increase in nanofiber length allows for a decrease in the required transport from one nanofiber to another allowing for a decrease in electrical resistivity. It should be noted that while a consistent value for conductive ZnO and NiO is difficult to find due to the dependence on oxygen vacancies, synthesis procedure and impurities, these nanofibers display electrical conductivities twice that of typical nanoparticle conductivities (~7000 S/m) and still greater than sputtered material (~10,000 S/m).[146] Therefore, these structures present very exciting properties that could be used within thin film photovoltaic devices due to their great electrical properties and porous structure allowing for high contact between photovoltaic material and charge transport layer.

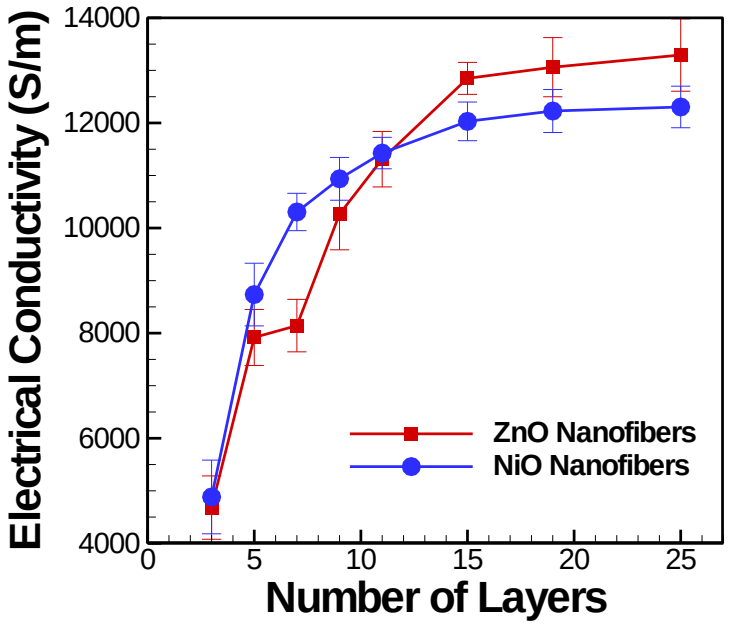

Figure 43. Electrical conductivity of ZnO and NiO nanofibers produced via alternating aligned layers method described previously.

Further, the other layer within the typical construction of photovoltaic devices that may also be impacted by inorganic electrospun nanofibers is the photovoltaic material itself. Due to high recombination effects within the photovoltaic material layer caused by similar hopping mechanisms, one-dimensional materials could be utilized to transport charges directly to the proper layer. Thus, purely inorganic nanofibers comprised solely of PbSe were fabricated using the highly loaded water based electrospinning method followed by thermal treatment. The maximum temperature and the time at that temperature were varied to attempt to control the crystal size. **Figure 44** presents representative TEM images of PbSe nanofibers heat treated at 300℃, 450℃, and 600℃ resulting in PbSe nanocrystals with an average diameter of 14.2, 27.8, and 43.9 nm, respectively. This demonstrates the control of the crystal size by controlling the temperature of thermal treatment, similar to the process presented to control nickel and iron crystallization in Chapter 5.

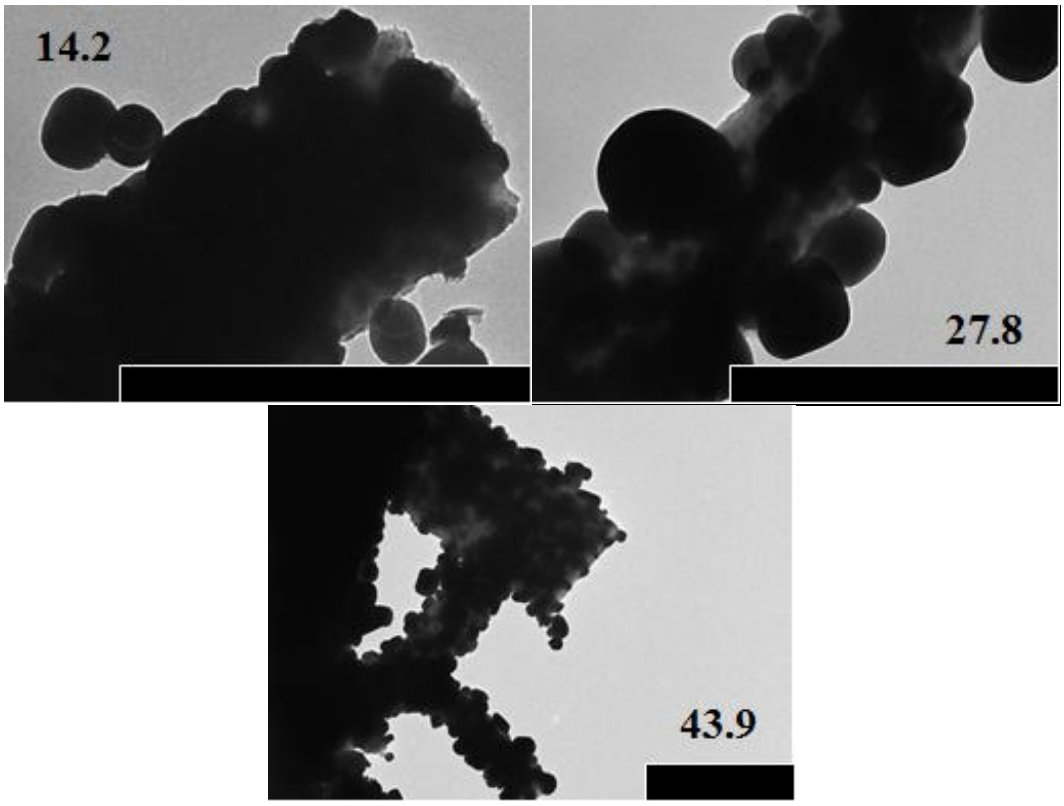

Figure 44. TEM images of highly loaded water based electrospun nanofibers following thermal treatment to generate PbSe crystals. Nanofibers are treated at 300℃ (top left), 450℃ (top right), and 600℃ (bottom) for 30 min displaying crystal size control. Average crystal size is inlaid in TEM images. Scale bar is 200 nm.

Graphs detailing the average crystal size for various thermal treatments are presented in **Figure 45**. The first method used to control crystal size, as detailed by the TEM images in Figure 44, was varying temperature with a constant dwell time. This showed the ability to control crystal size between 14.2 and 43 nm. However, as even smaller crystals are required to generate quantum confinement, the dwell time was also used at the lowest temperature to further attempt to control the crystal size. The second graph details this test where the dwell time was varied at 300℃ detailing the ability to control the crystal size from 10.2 to 31.7 nm for dwell times of 1 min to 120 min, respectively. The sample with the average crystal size of 10.2 nm was subsequently ground into powder form, placed in sonication for 10 min to generate a

coherent mixture of solution, and taken for absorption testing to find the wavelengths of light absorbed and subsequently the energy of photons promoting electrons within this material. However, even with this small crystal diameter the absorption peak was observed above 2500 nm near where the bulk absorption would be expected for PbSe. This indicates that quantum confinement, which typically occurs around 8 nm for PbSe,[139] hasn't been achieved in a consistent manner.

Further, the error bars in both graphs detail a large fluctuation in crystal diameter, which could also affect the performance of these nanofibers. Even when quantum confined crystals are generated, the poly-dispersity of the sizes within this structure could generate difficulties in maximizing the energy generated by these devices. If a higher energy photon, one that is of proper energy to promote an electron to the conducting band of a quantum confined crystal, is absorbed by a crystal of larger size and thus decreased band-gap energy, the rest of the energy from the photon would be lost as heat. This would result not only in decreased efficiency but also potential degradation of the device itself. The poly-dispersity could be a difficult phenomenon to overcome when generating photovoltaic materials by water based electrospinning with *in-situ* crystallization.

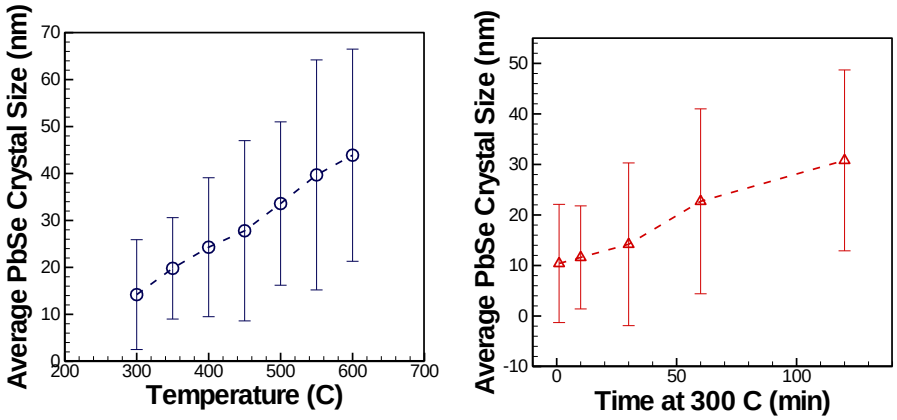

Figure 45. PbSe crystal size control via heating temperature temperature (top) and dwell time at a low maximum temperature. Small crystals are achieved in both methods, but neither showed quantum confined absorptions.

4. Conclusions

In summary, purely inorganic nanofibers are generated from the metal acetate precursor inclusion into highly loaded water based electrospinning. Various thermal treatments are used to generate ZnO, NiO, and PbSe nanofibers. ZnO and NiO were generated using the alternating aligned layer approach detailed previously display mat maintenance over 5 cm and great electrical conductivities surpassing both nanoparticle and sputtered film methods. These materials show great promise to increase the transport mechanism within thin film photovoltaic devices. Pure PbSe nanofibers are generated by precursor inclusion and display unique crystal size control by controlling the temperature and dwell time. However, neither method demonstrates the ability to control PbSe crystal control to generate small enough crystals to generate quantum confinement or mono-dispersity. Many future works pertain to this project and will be discussed in Chapter 9.

CHAPTER 9

CONCLUSIONS AND FUTURE WORK

1. Electrospinning Inorganic Nanofibers for Biomass Conversion via Alkaline Hydrothermal Treatment.

Initially, sol-gel chemistry was used to generate purely inorganic precursor solutions with the proper viscosity for electrospinning. Secondary metal precursors, iron and nickel nitrate, were included within this solution, and following electrospinning thermal treatment was used to crystallize these and generate silica nanofibers with *in-situ* fabricated nanoparticles. These were then tested as catalysts in the alkaline hydrolysis of glucose and shown to have great conversions. The catalytic effectiveness of nickel was shown to be superior to iron, the kinetics of the reaction were probed and shown through Damkohler number and effectiveness factor calculations that monoaxial nanofibers have significant mass transfer limitations but these are overcome in coaxial nanofibers with the catalyst tuned toward the surface. It was also shown via constant temperature tests and heating rate tests that the conversion and purity of gas produced can be optimized to a near pure hydrogen stream at low temperature – ideal for a setting using an onsite H_2/O_2 fuel cell. However, drawbacks were found due to catalytic deactivation within the silica nanofibers potentially caused by the absorption of water into the nanofiber matrix.

Therefore, a new method to generate purely inorganic nanofibers was found by covalently bonding high concentrations of metal precursors to a water soluble polymer, electrospinning, and thermally treating these to remove the organic component and crystallize the precursor. The covalent bonding of the metal precursor is confirmed via FTIR and shown to be nearly saturated at a composition of metal

acetate: PVA of 4:1 by mass. This bonding allows for the generation of a homogeneous distribution of metal throughout the polymer, which therefore allows for proper solution properties for nanofiber production. From this, as well as the generation of various solution compositions by inclusion of multiple precursors and the various thermal treatment procedures allowed for a number of different morphology and materials to be generated. A few such morphologies were purely catalytic surfaces, discrete catalysts tuned to the surface, and a pure catalyst shell with a substrate core all moving away from silica to avoid the catalytic deactivation viewed previously. This method, when applied to the alkaline hydrolysis of glucose, showed exciting catalytic properties where the temperature range at which near pure hydrogen gas is produced was controlled by the available surface area of catalyst within the diffusion length scale of the reactant – increasing from 140℃ to 193℃ by tuning discrete domains of catalyst to the surface of the nanofiber.

2. Magnetic and Electrical Properties of Purely Inorganic Nanofibers via High Loading Water Based Electrospinning.

Highly loaded water based electrospinning was shown to be able to generate very diverse materials that allow for use in a variety of property tests and applications. Purely metallic nanofibers were generated both isotropically and aligned, thermally treated under a variety of conditions and tested for electrical conductivity. These materials show electrical conductivities orders of magnitude higher than previously reported for one-dimensional materials, and the electrical conductivity was shown to be directionally tunable by nanofiber alignment. Further the magnetic properties were tested and shown to be a function of test temperature, crystal size, and crystal density. These variables are known to be a function of thermal treatment for single component nanofibers, but also controlled by including a discrete domain of minor phase crystals

supported within a majority domain insulating matrix. This generates very small nanocrystals capable of attaining near superparamagnetic behavior at room temperature.

3. Alternating Layers for Long Range Mat Maintenance

As-spun isotropic nanofiber mats and single-direction aligned mats from highly loaded water based electrospinning, among other methods, were shown to have the tendency to curl and/or fracture during thermal treatment due to the volume reduction caused by removing the organic components and crystallizing the metallic precursors. This curling and fracturing decreases the macroscopic ability to use these nanofibers as membranes, stand-alone electrodes, catalytic layers on membranes, and many other real world applications. Alternating layers of aligned nanofibers were subsequently electrospun to generate a layered checkerboard mat where each layer, when thermally treated, has a reduced ability to contract axially because of the perpendicular support offered by the previous and subsequent layer, and thus has an enhanced radial contraction. In turn macroscopic mats are maintained over long ranges as tested by ellipsometry detailing maintained uniform surface reflectivity for checkerboard mats after thermal treatment, but strong variances in surface reflectivity for isotropic mats thermally treated.

5. Inorganic Electrospun Nanofibers as Power Generation Materials.

One-dimensional materials have been synthesized previously by other research groups and shown to reduce the pulverization phenomenon often seen in high capacity materials when utilized as lithium ion battery anodes. Therefore, similar materials were synthesized here via water based electrospinning. Many metal oxides have been tested, but due to the inability to synthesize a single-crystalline nanofiber,

pulverization has still been seen. Especially high capacity materials such as germanium and silicon nanofibers have been synthesized high capacity crystals have placed within matrices of zirconia, alumina, and carbon to analyze their stability when placed in a supporting structure as a secondary material. These are currently being tested as anodic materials within lithium ion batteries. These materials, as well as other materials possible because of the diverse materials and morphologies able to be synthesized display great promise for generating high capacity electrodes.

Photovoltaic thin films also may benefit from the inclusion of inorganic electrospun nanofibers. Typical thin film structures include five layers, two outer electrode layers, two inner charge transport layers, and a central photovoltaic material layer. Other groups have probed using ZnO and NiO as the transport layers with sputtered and nanoparticle layers indicating proper band-gap structures but limited electrical conductivities and transport mechanisms. However, as previously described ultra-high aspect ratio inorganic electrospun nanofibers have high electrical conductivities and high surface areas, both great characteristics for charge transport layers. Pure ZnO and NiO metal oxide crystalline nanofibers were synthesized and shown to have high conductivities, even greater than typical closely packed nanoparticle systems. Further, pure PbSe nanofibers are able to be created potentially to be included as the photovoltaic material itself, but to this point quantum confinement has not been achieved. Both of these materials, however, display great promise as materials to be included within thin film photovoltaic devices.

6. *Future Work*

From these results pertaining to catalytic nanofibers, there are a number of different avenues to pursue. First and foremost, the water-based highly loaded catalytic nanofibers indicated that even beyond the concentration of catalyst available,

the geometry available to the reactants greatly influenced the purity of the products found. This indicates that perhaps increasing the available surface area beyond a pure shell or discrete domains near the surface would influence the effectiveness of these materials greatly. Increasing the porosity of these materials could increase the available surface of the material greatly thereby increasing the purity of products, especially in gas phase reactions. This increase in porosity could be achieved simply by including a second water soluble polymer that will not react with the metal acetate precursors and thus would leave a void upon thermal treatment. Also, hollow materials could allow for increased surface area to volume ratio through coaxial electrospinning, or by including a block copolymer that is known to phase separate into inverse cylinders that thereby could generate pores upon thermal treatment. This could be especially advantageous when using expensive catalysts to allow for the use of nearly all the material.

The catalytic nanofibers synthesized currently could also be tested in catalyzing higher order biomass as well. Glucose was thoroughly tested in this round of procedures, but this is only marginally useful in an industrial setting as the majority of biomass comes as cellulosic or other biomass feed stocks. Therefore, nickel catalysts from the high loading water based system could be synthesized and tested for catalyzing model cellulose as purchased with variables pertaining to degree of crystallinity, degree of polymerization, and biomass morphology. The mobility of these biomass particles could generate even further mass transfer limitations due to the decreased diffusion of high molecular weight cellulose within the nanofiber matrix and thus require greater catalyst concentrations and tuning toward the surface of the nanofiber. Blends of real biomass could also be used as feed stocks to analyze the real world applicability of these catalysts. Hemicellulose and lignin typically plague these processes, and developing a catalyst/support system that could overcome this would

be a breakthrough and significantly decrease the pretreatment requirements to generate a usable fuel source. The diverse morphologies generated by highly loaded water based electrospinning, as well as the potential use of block copolymers to generate porous nanofibers could overcome both of these current impediments. However, it is likely that a pretreatment step may still be required to generate solutions capable of being incorporated into the nanofiber framework.

The highly loaded water based electrospinning also appeared to have very exciting electrical properties. Beyond the preliminary tests done indicating the control of conductivity by control of the crystal structure within the nanofiber and the macroscopic nanofiber direction, many exciting tests can be run. Temperature dependence can be tested to display differences in electrical conductivity between bulk structures, which should decrease with increasing temperature, and nanofiber systems which may increase with increasing temperature. Further superconducting temperatures can be tested via variable temperature tests, and dopants can be used in materials such as semiconductors to increase conductivities. Hall-effect tests, which apply a current in one direction and measure the voltage in the perpendicular direction, can be run to both further quantify the degree of anisotropy within the nanofiber mats and to analyze the carrier density within many of these semiconductor materials. Carrier densities are a function of material, structure, and the synthesis procedure by function of oxygen vacancies. This would further indicate the relevance of using ZnO and NiO nanofibers within the thin film photovoltaic devices.

These ZnO nanofibers, as well as NiO nanofibers, can currently be incorporated into thin film photovoltaic devices as charge transport layers. These materials would have the advantage of having more contact area with the photovoltaic material and decrease the hopping inefficiencies required to transport charge through nanoparticle films. To test these materials, ShotKey devices may be the best first

analysis tool to probe their usefulness. ShotKey devices consist of two electrodes surrounding a single charge transport layer and the photovoltaic material, thereby decreasing the difficulty of analyzing two transport layers and the associated different interfaces. These devices will have lower overall efficiencies, but when analyzed against ShotKey devices fabricated of typical nanoparticle layers and sputtered layers, the general increase in efficiency could be analyzed, as detailed by **Figure 46**. If this displays benefits, the charge transport layers could be included in full five layer thin film photovoltaic devices with each nanofiber layer tested separately with a highly conductive opposite charge transport layer. If these charge transport layers continue to prove advantageous, both layers could be incorporated into a device using lamination of the second layer, with a typical photovoltaic material as the center layer.

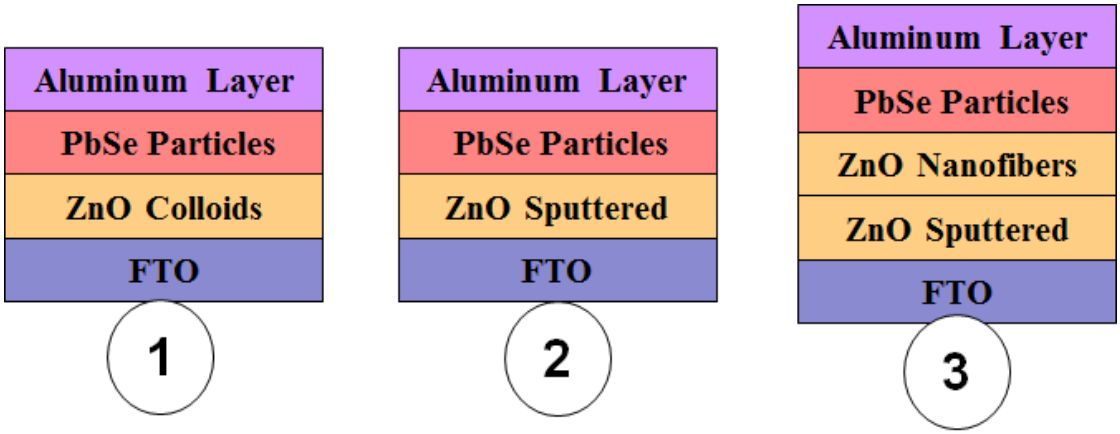

Figure 46. A proposed method for analyzing the effectiveness of each charge transport layer independently is the use of ShotKey devices where only one charge transport layer is used to minimize efficiency effects associated with the other layer interface.

Near pure PbSe nanofibers can also be fabricated as displayed by TEM. The crystal size, while controlled by time and temperature, does not appear controllable down to the quantum confinement size below 11 nm. Therefore, PbSe could be included within a secondary matrix, initially perhaps ZrO_2, to control crystal size. This, therefore, could generate PbSe nanocrystals that are quantum confined within a

nanofiber matrix. After this, perhaps including these materials into a conducting matrix such as copper or silver would be advantageous to not only control crystal size but also allow for transport of electrons and holes to their respective charge transport layers. This may induce large amounts of recombination within the conducting nanofiber, in which case additional research into core shell morphologies using ZnO and NiO with PbSe in each domain or tri-axial electrospinning with ZnO, PbSe, and NiO as three layers respectively could be formed to decrease this effect while generating a single nanofiber photovoltaic device. However, if these quantum confined PbSe crystals could be formed in a conducting matrix that doesn't suffer tremendous recombination inefficiencies, these could directly be incorporated into a typical thin film photovoltaic device with highly functional charge transport layers such as PCBM and PEDOT. Subsequently, if this proves useful, ZnO and NiO nanofiber layers could be used in place of their respective transport layers used previously, to generate a purely electrospun photovoltaic device. Finally, some of the Copper/PbSe nanofibers could be placed in sonication to generate shorter nanofibers allowing for them to probe the micron size pores between the charge transport layers, thereby increasing the use of the high contact area afforded by the nanofiber structure. The evolution of this proposed research is detailed below in **Figure 47**.

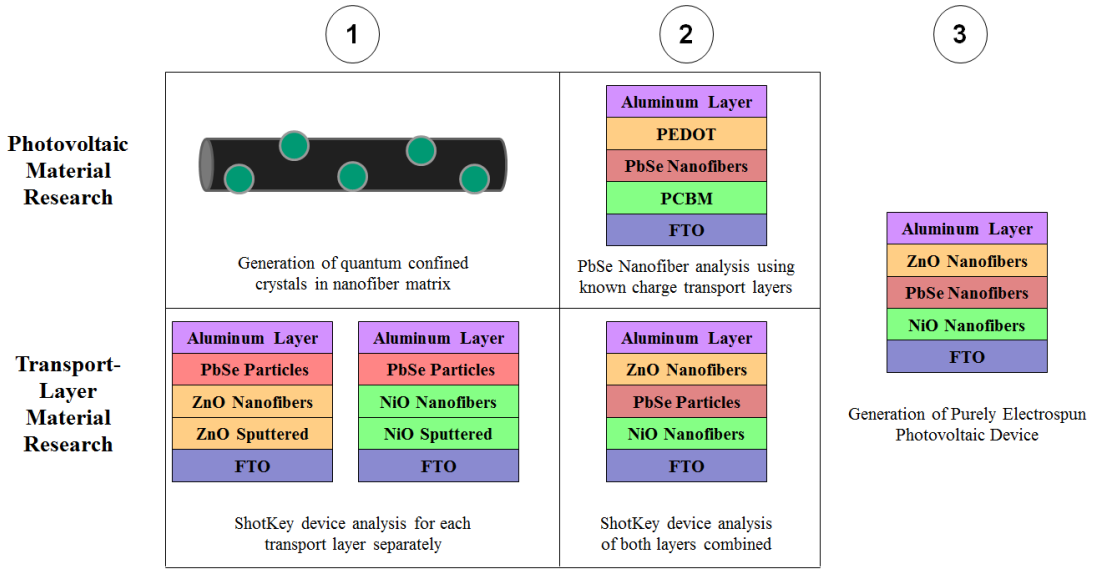

Figure 47. Evolution of proposed photovoltaic material research from quantum confined crystal generation within zirconia nanofibers to inclusion in a conducting nanofiber, the subsequent inclusion of those materials within a standard photovoltaic device and finally the incorporation of these into an electrospun photovoltaic device.

Further power generation materials are also able to be fabricated. Preliminary data is presented for nanofibers of many metal oxide morphologies displaying pulverization or loss of crystal adherence at short cycles. Metal sulfides also display high capacities and may generate even further stability and could be tested. Further, germanium and tin are incorporated in a number of matrices in an attempt to generate high capacity materials that will withstand many cycles and decrease pulverization. These are still ongoing tests. Preliminary data presented indicates that these display promising capacities and stability, and thus increased concentrations of these nanoparticles could be included to decrease the loading requirement and increase the capacity per nanofiber. Silicon nanoparticles and precursors could also be incorporated within these matrices to advance to an even higher capacity. Smaller nanoparticles could be synthesized prior to inclusion and placed specifically near the surface of the nanofiber to account for electrically insulating substrates. Some data

indicates that electrically conductive substrates provide greater electron distribution and thus this could overcome some of those influences. Coaxial nanofibers could also be fabricated with an electrically conducting core such as copper or silver to overcome the insulating phenomenon associated with zirconia and alumina. A schematic detailing some avenues that could be used to control various properties is presented in **Figure 48**. Cathodic materials could also be fabricated, such as $LiTi_5O_{10}$, $LiCoO_2$, $LiMn_2O_4$ and others. These materials could be fabricated with a conducting core such as Copper that may serve as a stabilization aspect to these nanofibers during charging and discharging as well as provide strong electrical conductivity for faster charge/discharge rates.

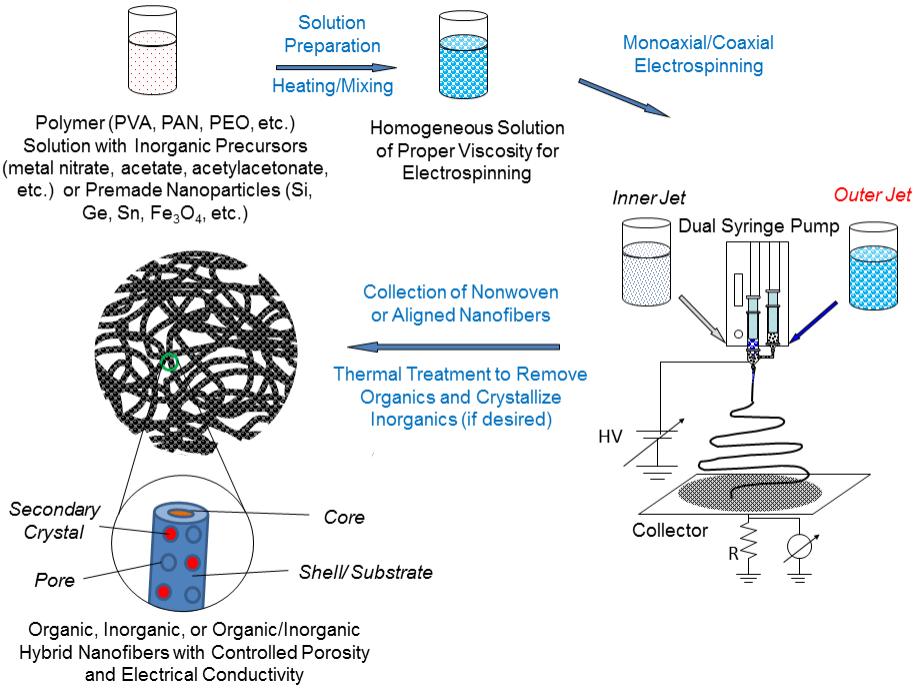

Figure 48. Schematic detailing potential property control within lithium ion battery electrodes to generate high capacity materials stable over many cycles capable of high charge/discharge rates.

These are but a taste of the number of directions that this research could proceed in. Super-capacitors, membranes, biochemical electrodes, magnetically active filters are other potential avenues for research, but this work could transfer to drug delivery, enzymatic bio-fuel cells, model crystallization reactors, and many others. It appears to be a very diverse platform for generating unique structures from a cost effective, scalable process.

REFERENCES

1. Kruis, F.E., H. Fissan, and A. Peled, *Synthesis of nanoparticles in the gas phase for electronic, optical and magnetic applications - A review.* Journal of Aerosol Science, 1998. **29**(5-6): p. 511-535.
2. Bakunin, V.N., et al., *Synthesis and application of inorganic nanoparticles as lubricant components - a review.* Journal of Nanoparticle Research, 2004. **6**(2-3): p. 273-284.
3. Lee, E.J.H., et al., *Photoluminescence in quantum-confined SnO2 nanocrystals: Evidence of free exciton decay.* Applied Physics Letters, 2004. **84**(10): p. 1745-1747.
4. Sun, S.H. and H. Zeng, *Size-controlled synthesis of magnetite nanoparticles.* Journal of the American Chemical Society, 2002. **124**(28): p. 8204-8205.
5. Xu, A.W., Y. Gao, and H.Q. Liu, *The preparation, characterization, and their photocatalytic activities of rare-earth-doped TiO2 nanoparticles.* Journal of Catalysis, 2002. **207**(2): p. 151-157.
6. Robel, I., et al., *Quantum dot solar cells. Harvesting light energy with CdSe nanocrystals molecularly linked to mesoscopic TiO2 films.* Journal of the American Chemical Society, 2006. **128**(7): p. 2385-2393.
7. Gas, J., et al., *Superparamagnetic polymer nanocomposites with uniform Fe3O4 nanoparticle dispersions.* Advanced Functional Materials, 2006. **16**(1): p. 71-75.
8. Rioux, R.M., et al., *High-surface-area catalyst design: Synthesis, characterization, and reaction studies of platinum nanoparticles in mesoporous SBA-15 silica.* Journal of Physical Chemistry B, 2005. **109**(6): p. 2192-2202.
9. Balazs, A.C., T. Emrick, and T.P. Russell, *Nanoparticle polymer composites: Where two small worlds meet.* Science, 2006. **314**(5802): p. 1107-1110.
10. Hamley, I.W., *Nanostructure fabrication using block copolymers.* Nanotechnology, 2003. **14**(10): p. R39-R54.
11. Xie, J.W., X.R. Li, and Y.N. Xia, *Putting Electrospun Nanofibers to Work for Biomedical Research.* Macromolecular Rapid Communications, 2008. **29**(22): p. 1775-1792.
12. Grzelczak, M., et al., *Shape control in gold nanoparticle synthesis.* Chemical Society Reviews, 2008. **37**(9): p. 1783-1791.
13. Nedelcu, M., et al., *Block copolymer directed synthesis of mesoporous TiO(2) for dye-sensitized solar cells.* Soft Matter, 2009. **5**(1): p. 134-139.
14. Stoykovich, M.P. and P.F. Nealey, *Block copolymers and conventional lithography.* Materials Today, 2006. **9**(9): p. 20-29.
15. Bratlie, K.M., et al., *Platinum nanoparticle shape effects on benzene hydrogenation selectivity.* Nano Letters, 2007. **7**(10): p. 3097-3101.
16. Lu, X.F., C. Wang, and Y. Wei, *One-Dimensional Composite Nanomaterials: Synthesis by Electrospinning and Their Applications.* Small, 2009. **5**(21): p. 2349-2370.

17. Weber, J., et al., *One-dimensional nanostructures: fabrication, characterisation and applications.* International Materials Reviews, 2008. **53**(4): p. 235-255.
18. Daly, B., et al., *Synthesis and characterization of highly ordered cobalt-magnetite nanocable arrays.* Small, 2006. **2**(11): p. 1299-1307.
19. Woodruff, J.H., et al., *Vertically oriented germanium nanowires grown from gold colloids on silicon substrates and subsequent gold removal.* Nano Letters, 2007. **7**(6): p. 1637-1642.
20. Schmidt, V., S. Senz, and U. Gosele, *Diameter-dependent growth direction of epitaxial silicon nanowires.* Nano Letters, 2005. **5**(5): p. 931-935.
21. Feng, X.J., et al., *Vertically Aligned Single Crystal TiO2 Nanowire Arrays Grown Directly on Transparent Conducting Oxide Coated Glass: Synthesis Details and Applications.* Nano Letters, 2008. **8**(11): p. 3781-3786.
22. Zhang, Y., et al., *Control of catalytic reactions at the surface of a metal oxide nanowire by manipulating electron density inside it.* Nano Letters, 2004. **4**(3): p. 403-407.
23. Vaddiraju, S., et al., *Mechanisms of 1D crystal growth in reactive vapor transport: Indium nitride nanowires.* Nano Letters, 2005. **5**(8): p. 1625-1631.
24. Duan, X.F. and C.M. Lieber, *Laser-assisted catalytic growth of single crystal GaN nanowires.* Journal of the American Chemical Society, 2000. **122**(1): p. 188-189.
25. Busbee, B.D., S.O. Obare, and C.J. Murphy, *An improved synthesis of high-aspect-ratio gold nanorods.* Advanced Materials, 2003. **15**(5): p. 414-+.
26. Huang, L.M., et al., *Polyaniline nanowires by electropolymerization from liquid crystalline phases.* Journal of Materials Chemistry, 2002. **12**(2): p. 388-391.
27. Xu, C., et al., *Growth of Ga-doped ZnO nanowires by two-step vapor phase method.* Applied Physics Letters, 2005. **86**(13).
28. Dzenis, Y., *Spinning continuous fibers for nanotechnology.* Science, 2004. **304**(5679): p. 1917-1919.
29. Li, D. and Y.N. Xia, *Electrospinning of nanofibers: Reinventing the wheel?* Advanced Materials, 2004. **16**(14): p. 1151-1170.
30. Teo, W.E. and S. Ramakrishna, *A review on electrospinning design and nanofibre assemblies.* Nanotechnology, 2006. **17**(14): p. R89-R106.
31. Huang, Z.M., et al., *A review on polymer nanofibers by electrospinning and their applications in nanocomposites.* Composites Science and Technology, 2003. **63**(15): p. 2223-2253.
32. Chronakis, I.S., *Novel nanocomposites and nanoceramics based on polymer nanofibers using electrospinning process - A review.* Journal of Materials Processing Technology, 2005. **167**(2-3): p. 283-293.
33. McCann, J.T., M. Marquez, and Y.N. Xia, *Melt coaxial electrospinning: A versatile method for the encapsulation of solid materials and fabrication of phase change nanofibers.* Nano Letters, 2006. **6**(12): p. 2868-2872.
34. Wang, X.F., et al., *Formation of water-resistant hyaluronic acid nanofibers by blowing-assisted electro-spinning and non-toxic post treatments.* Polymer,

2005. **46**(13): p. 4853-4867.
35. Deitzel, J.M., et al., *Electrospinning of polymer nanofibers with specific surface chemistry.* Polymer, 2002. **43**(3): p. 1025-1029.
36. Pham, Q.P., U. Sharma, and A.G. Mikos, *Electrospinning of polymeric nanofibers for tissue engineering applications: A review.* Tissue Engineering, 2006. **12**(5): p. 1197-1211.
37. Kalra, V., et al., *Controlling Nanoparticle Location via Confined Assembly in Electrospun Block Copolymer Nanofibers.* Small, 2008. **4**(11): p. 2067-2073.
38. Li, D. and Y.N. Xia, *Direct fabrication of composite and ceramic hollow nanofibers by electrospinning.* Nano Letters, 2004. **4**(5): p. 933-938.
39. Panels, J.E. and Y.L. Joo, *Incorporation of vanadium oxide in silica nanofiber mats via electrospinning and sol-gel synthesis.* Journal of Nanomaterials, 2006.
40. Hansen, N.S., et al., *Inorganic nanofibers with tailored placement of nanocatalysts for hydrogen production via alkaline hydrolysis of glucose.* Nanotechnology, 2011. **22**(32).
41. Loscertales, I.G., et al., *Electrically forced coaxial nanojets for one-step hollow nanofiber design.* Journal of the American Chemical Society, 2004. **126**(17): p. 5376-5377.
42. Kalra, V., et al., *Confined assembly in coaxially electrospun block-copolymer fibers.* Advanced Materials, 2006. **18**(24): p. 3299-+.
43. Yin, Y.D., et al., *Silver nanowires can be directly coated with amorphous silica to generate well-controlled coaxial nanocables of silver/silica.* Nano Letters, 2002. **2**(4): p. 427-430.
44. Sun, Y. and J. Cheng, *Hydrolysis of lignocellulosic materials for ethanol production: a review.* BIORESOURCE TECHNOLOGY, 2002. **83**(1): p. 1-11.
45. Steele, B. and A. Heinzel, *Materials for fuel-cell technologies.* NATURE, 2001. **414**(6861): p. 345-352.
46. Baschuk, J. and X. Li, *Carbon monoxide poisoning of proton exchange membrane fuel cells.* INTERNATIONAL JOURNAL OF ENERGY RESEARCH, 2001. **25**(8): p. 695-713.
47. Schlapbach, L. and A. Zuttel, *Hydrogen-storage materials for mobile applications.* NATURE, 2001. **414**(6861): p. 353-358.
48. Ishida, M., et al., *Production of COx-free hydrogen from biomass and NaOH mixture: Effect of catalysts.* Energy & Fuels, 2006. **20**(2): p. 748-753.
49. Kulprathipanja, A. and J. Falconer, *Partial oxidation of methanol for hydrogen production using ITO/Al2O3 nanoparticle catalysts.* APPLIED CATALYSIS A-GENERAL, 2004. **261**(1): p. 77-86.
50. Zhang, Y., N. Kohler, and M. Zhang, *Surface modification of superparamagnetic magnetite nanoparticles and their intracellular uptake.* BIOMATERIALS, 2002. **23**(7): p. 1553-1561.
51. Jia, H., G. Zhu, and P. Wang, *Catalytic behaviors of enzymes attached to nanoparticles: The effect of particle mobility.* BIOTECHNOLOGY AND BIOENGINEERING, 2003. **84**(4): p. 406-414.
52. Hughes, G., *Nanostructure-mediated drug delivery.* DM DISEASE-A-MONTH, 2005. **51**(6): p. 342-361.

53. Kalra, V., et al., *Controlling Nanoparticle Location via Confined Assembly in Electrospun Block Copolymer Nanofibers.* SMALL, 2008. **4**(11): p. 2067-2073.
54. delMonte, F., et al., *Formation of gamma-Fe2O3 isolated nanoparticles in a silica matrix.* LANGMUIR, 1997. **13**(14): p. 3627-3634.
55. Fabrizioli, P., et al., *Synthesis, structural and chemical properties of iron oxide-silica aerogels.* JOURNAL OF MATERIALS CHEMISTRY, 2002. **12**(3): p. 619-630.
56. Zhang, L., et al., *Novel gamma-Fe2O3/SiO2 magnetic nanocomposites via sol-gel matrix-mediated synthesis.* NANOSTRUCTURED MATERIALS, 1997. **9**(1-8): p. 185-188.
57. Ishida, Y., et al., *Selective hydrogen generation from real biomass through hydrothermal reaction at relatively low temperatures.* Biomass & Bioenergy, 2009. **33**(1): p. 8-13.
58. Li, D. and Y. Xia, *Electrospinning of nanofibers: Reinventing the wheel?* ADVANCED MATERIALS, 2004. **16**(14): p. 1151-1170.
59. Teo, W. and S. Ramakrishna, *A review on electrospinning design and nanofibre assemblies.* NANOTECHNOLOGY, 2006. **17**(14): p. R89-R106.
60. Bognitzki, M., et al., *Nanostructured fibers via electrospinning.* ADVANCED MATERIALS, 2001. **13**(1): p. 70-+.
61. Li, D. and Y. Xia, *Direct fabrication of composite and ceramic hollow nanofibers by electrospinning.* NANO LETTERS, 2004. **4**(5): p. 933-938.
62. Choi, S., et al., *Silica nanofibers from electrospinning/sol-gel process.* JOURNAL OF MATERIALS SCIENCE LETTERS, 2003. **22**(12): p. 891-893.
63. Zhan, S., D. Chen, and M. Jiao, *Co-electrospun SiO2 hollow nanostructured fibers with hierarchical walls.* JOURNAL OF COLLOID AND INTERFACE SCIENCE, 2008. **318**(2): p. 331-336.
64. Zhao, Y., et al., *Fabrication of refining mesoporous silica nanofibers via electrospinning.* MATERIALS LETTERS, 2008. **62**(1): p. 143-146.
65. Watthanaarun, J., V. Pavarajarn, and P. Supaphol, *Titanium (IV) oxide nanofibers by combined sol-gel and electrospinning techniques: preliminary report on effects of preparation conditions and secondary metal dopant.* SCIENCE AND TECHNOLOGY OF ADVANCED MATERIALS, 2005. **6**(3-4): p. 240-245.
66. Panels, J., et al., *Synthesis and characterization of magnetically active carbon nanofiber/iron oxide composites with hierarchical pore structures.* NANOTECHNOLOGY, 2008. **19**(45): p. -.
67. Chew, S., et al., *Sustained release of proteins from electrospun biodegradable fibers.* BIOMACROMOLECULES, 2005. **6**(4): p. 2017-2024.
68. Luong-Van, E., et al., *Controlled release of heparin from poly(epsilon-caprolactone) electrospun fibers.* BIOMATERIALS, 2006. **27**(9): p. 2042-2050.
69. Patel, A., et al., *Electrospinning of porous silica nanofibers containing silver nanoparticles for catalytic applications.* CHEMISTRY OF MATERIALS, 2007. **19**(6): p. 1231-1238.

70. Ketteler, G., et al., *Bulk and surface phases of iron oxides in an oxygen and water atmosphere at low pressure.* PHYSICAL CHEMISTRY CHEMICAL PHYSICS, 2001. **3**(6): p. 1114-1122.
71. Bailey, J.R. and M.M. McGuire, *ATR-FTIR observations of water structure in colloidal silica: Implications for the hydration force mechanism.* Langmuir, 2007. **23**(22): p. 10995-10999.
72. Amonette, J.E. and D. Rai, *Identification of Noncrystalline (Fe,Cr)(Oh)3 by Infrared-Spectroscopy.* Clays and Clay Minerals, 1990. **38**(2): p. 129-136.
73. Krehula, S. and S. Music, *Influence of ruthenium ions on the precipitation of alpha-FeOOH, alpha-Fe2O3 and Fe3O4 in highly alkaline media.* Journal of Alloys and Compounds, 2006. **416**(1-2): p. 284-290.
74. Sinag, A., et al., *Catalytic hydrothermal conversion of cellulose over SnO(2) and ZnO nanoparticle catalysts.* Journal of Supercritical Fluids, 2011. **56**(2): p. 179-185.
75. Lin, Y.C. and G.W. Huber, *The critical role of heterogeneous catalysis in lignocellulosic biomass conversion.* Energy & Environmental Science, 2009. **2**(1): p. 68-80.
76. Kim, T., et al., *Kinetics of gold nanoparticle aggregation: Experiments and modeling.* Journal of Colloid and Interface Science, 2008. **318**(2): p. 238-243.
77. Li, D., J.T. McCann, and Y.N. Xia, *Electrospinning: A simple and versatile technique for producing ceramic nanofibers and nanotubes.* Journal of the American Ceramic Society, 2006. **89**(6): p. 1861-1869.
78. Patel, A.C., et al., *Electrospinning of porous silica nanofibers containing silver nanoparticles for catalytic applications.* Chemistry of Materials, 2007. **19**(6): p. 1231-1238.
79. Goyal, H.B., D. Seal, and R.C. Saxena, *Bio-fuels from thermochemical conversion of renewable resources: A review.* Renewable & Sustainable Energy Reviews, 2008. **12**(2): p. 504-517.
80. Sutton, D., B. Kelleher, and J.R.H. Ross, *Review of literature on catalysts for biomass gasification.* Fuel Processing Technology, 2001. **73**(3): p. 155-173.
81. Mohan, D., C.U. Pittman, and P.H. Steele, *Pyrolysis of wood/biomass for bio-oil: A critical review.* Energy & Fuels, 2006. **20**(3): p. 848-889.
82. Wang, P.S., et al., *H-1 nuclear magnetic resonance characterization of Portland cement: molecular diffusion of water studied by spin relaxation and relaxation time-weighted imaging.* Journal of Materials Science, 1998. **33**(12): p. 3065-3071.
83. Wu, C.H., A. Mulchandani, and W. Chen, *Versatile microbial surface-display for environmental remediation and biofuels production.* Trends in Microbiology, 2008. **16**(4): p. 181-188.
84. Carere, C.R., et al., *Third generation biofuels via direct cellulose fermentation.* International Journal of Molecular Sciences, 2008. **9**(7): p. 1342-1360.
85. Datar, R., et al., *Hydrogen production from the fermentation of corn stover biomass pretreated with a steam-explosion process.* International Journal of Hydrogen Energy, 2007. **32**(8): p. 932-939.
86. Saxena, R.C., D.K. Adhikari, and H.B. Goyal, *Biomass-based energy fuel*

through biochemical routes: A review. Renewable & Sustainable Energy Reviews, 2009. **13**(1): p. 156-167.
87. Lynd, L.R., et al., *Fuel Ethanol from Cellulosic Biomass.* Science, 1991. **251**(4999): p. 1318-1323.
88. Onda, A., T. Ochi, and K. Yanagisawa, *Selective hydrolysis of cellulose into glucose over solid acid catalysts.* Green Chemistry, 2008. **10**(10): p. 1033-1037.
89. Ni, M., et al., *An overview of hydrogen production from biomass.* Fuel Processing Technology, 2006. **87**(5): p. 461-472.
90. Hansen, N.S.C., D.; Joo, Y.L., *Catalytic Silica Nanofibers with Nickel Nanocrystals from Sol-Gel Chemistry for Hydrogen Production via Alkaline Hydrolysis of Glucose.* Journal of Catalysis, 2011: p. In Preparation.
91. Cho, D., et al., *Properties of PVA/HfO(2) Hybrid Electrospun Fibers and Calcined Inorganic HfO(2) Fibers.* Journal of Physical Chemistry C, 2011. **115**(13): p. 5535-5544.
92. Hansen, N.S.C., D.; Joo, Y.L., *Metal Nanofibers with Highly Tunable Electrical and Magnetic Properties via Highly Loaded Water Based Electrospinning.* SMALL, 2011: p. In Preparation.
93. Park, T.J., et al., *Size-dependent magnetic properties of single-crystalline multiferroic BiFeO3 nanoparticles.* Nano Letters, 2007. **7**(3): p. 766-772.
94. Kan, S., et al., *Synthesis and size-dependent properties of zinc-blende semiconductor quantum rods.* Nature Materials, 2003. **2**(3): p. 155-158.
95. Werner, F., et al., *Electrical Conductivity of InN Nanowires and the Influence of the Native Indium Oxide Formed at Their Surface.* Nano Letters, 2009. **9**(4): p. 1567-1571.
96. Wu, B. and J.J. Boland, *Synthesis and dispersion of isolated high aspect ratio gold nanowires.* Journal of Colloid and Interface Science, 2006. **303**(2): p. 611-616.
97. Hersee, S.D., X.Y. Sun, and X. Wang, *The controlled growth of GaN nanowires.* Nano Letters, 2006. **6**(8): p. 1808-1811.
98. Ramaseshan, R., et al., *Nanostructured ceramics by electrospinning.* Journal of Applied Physics, 2007. **102**(11).
99. Wu, H., et al., *Electrospinning of Fe, Co, and Ni nanofibers: Synthesis, assembly, and magnetic properties.* Chemistry of Materials, 2007. **19**(14): p. 3506-3511.
100. Ponhan, W. and S. Maensiri, *Fabrication and magnetic properties of electrospun copper ferrite (CuFe(2)O(4)) nanofibers.* Solid State Sciences, 2009. **11**(2): p. 479-484.
101. Shen, X.Q., et al., *Characterization and magnetic properties of electrospun Co(1-x) Zn (x) Fe(2)O(4) nanofibers.* Applied Physics a-Materials Science & Processing, 2010. **99**(1): p. 189-195.
102. Barakat, N.A.M., B. Kim, and H.Y. Kim, *Production of Smooth and Pure Nickel Metal Nanofibers by the Electrospinning Technique: Nanofibers Possess Splendid Magnetic Properties.* Journal of Physical Chemistry C, 2009. **113**(2): p. 531-536.

103. Lotus, A.F., et al., *Electrospinning route for the fabrication of p-n junction using nanofiber yarns.* Journal of Applied Physics, 2009. **106**(1).
104. Katta, P., et al., *Continuous electrospinning of aligned polymer nanofibers onto a wire drum collector.* Nano Letters, 2004. **4**(11): p. 2215-2218.
105. Li, D., Y.L. Wang, and Y.N. Xia, *Electrospinning of polymeric and ceramic nanofibers as uniaxially aligned arrays.* Nano Letters, 2003. **3**(8): p. 1167-1171.
106. Shelby, J.E., *Thermal-Expansion of Amorphous Metals.* Journal of Non-Crystalline Solids, 1979. **34**(1): p. 111-119.
107. Xin, B.F., et al., *Photocatalytic activity and interfacial carrier transfer of Ag-TiO2 nanoparticle films.* Applied Surface Science, 2005. **252**(5): p. 2050-2055.
108. Kim, F., J.H. Song, and P.D. Yang, *Photochemical synthesis of gold nanorods.* Journal of the American Chemical Society, 2002. **124**(48): p. 14316-14317.
109. Boukai, A.I., et al., *Silicon nanowires as efficient thermoelectric materials.* Nature, 2008. **451**(7175): p. 168-171.
110. Chan, C.K., et al., *High-performance lithium battery anodes using silicon nanowires.* Nature Nanotechnology, 2008. **3**(1): p. 31-35.
111. Inoue, M., et al., *Magneto-optical properties of one-dimensional photonic crystals composed of magnetic and dielectric layers.* Journal of Applied Physics, 1998. **83**(11): p. 6768-6770.
112. Li, D., T. Herricks, and Y.N. Xia, *Magnetic nanofibers of nickel ferrite prepared by electrospinning.* Applied Physics Letters, 2003. **83**(22): p. 4586-4588.
113. Hansen, N.S.C., D.; Joo, Y.L., *Control of Catalyst Geometry and Location Within Highly Loaded Water Based Electospinning for Selective Hydrogen Production from Biomass via Alkaline Hydrothermal Treatment.* ACS Advanced Materials and Interfaces, 2011: p. In Preparation.
114. Scrosati, B., *Recent advances in lithium ion battery materials.* Electrochimica Acta, 2000. **45**(15-16): p. 2461-2466.
115. Arico, A.S., et al., *Nanostructured materials for advanced energy conversion and storage devices.* Nature Materials, 2005. **4**(5): p. 366-377.
116. Kang, Y.M., et al., *A study on the charge-discharge mechanism of Co3O4 as an anode for the Li ion secondary battery.* Electrochimica Acta, 2005. **50**(18): p. 3667-3673.
117. Zhang, X.C., W. Shyy, and A.M. Sastry, *Numerical simulation of intercalation-induced stress in Li-ion battery electrode particles.* Journal of the Electrochemical Society, 2007. **154**(10): p. A910-A916.
118. Idota, Y., et al., *Tin-based amorphous oxide: A high-capacity lithium-ion-storage material.* Science, 1997. **276**(5317): p. 1395-1397.
119. Hosono, E., et al., *Synthesis of Single Crystalline Spinel LiMn(2)O(4) Nanowires for a Lithium Ion Battery with High Power Density.* Nano Letters, 2009. **9**(3): p. 1045-1051.
120. Chen, W.X., J.Y. Lee, and Z.L. Liu, *The nanocomposites of carbon nanotube with Sb and SnSb0.5 as Li-ion battery anodes.* Carbon, 2003. **41**(5): p. 959-966.

121. Wu, Y.P., E. Rahm, and R. Holze, *Carbon anode materials for lithium ion batteries.* Journal of Power Sources, 2003. **114**(2): p. 228-236.
122. Han, S.J., et al., *Simple synthesis of hollow tin dioxide microspheres and their application to lithium-ion battery anodes.* Advanced Functional Materials, 2005. **15**(11): p. 1845-1850.
123. Peterson, S.B., J. Apt, and J.F. Whitacre, *Lithium-ion battery cell degradation resulting from realistic vehicle and vehicle-to-grid utilization.* Journal of Power Sources, 2010. **195**(8): p. 2385-2392.
124. Kim, B.S., et al., *Catalyst-free Growth of Single-Crystal Silicon and Germanium Nanowires.* Nano Letters, 2009. **9**(2): p. 864-869.
125. Peng, K.Q., et al., *Silicon nanowires for rechargeable lithium-ion battery anodes.* Applied Physics Letters, 2008. **93**(3).
126. Wang, Z.Y., G. Chen, and D.G. Xia, *Coating of multi-walled carbon nanotube with SnO2 films of controlled thickness and its application for Li-ion battery.* Journal of Power Sources, 2008. **184**(2): p. 432-436.
127. Momma, T., et al., *SnS2 anode for rechargeable lithium battery.* Journal of Power Sources, 2001. **97-8**: p. 198-200.
128. Persson, A.I., et al., *Solid-phase diffusion mechanism for GaAs nanowire growth.* Nature Materials, 2004. **3**(10): p. 677-681.
129. Hansen, N.S.E., T.K.; hinestroza, J.; Joo, Y.L., *Maintenance of Flat, Thin, Nanofiber Mat Structure in water Based Electrospinning via Checkerboard Structure to Control Nanoscale Crystallization Direction.* SMALL, 2011: p. In Preparation.
130. Lewis, N.S., *Toward cost-effective solar energy use.* Science, 2007. **315**(5813): p. 798-801.
131. Gratzel, M., *Photoelectrochemical cells.* Nature, 2001. **414**(6861): p. 338-344.
132. Conibeer, G., et al., *Silicon nanostructures for third generation photovoltaic solar cells.* Thin Solid Films, 2006. **511**: p. 654-662.
133. Trupke, T., et al., *Very efficient light emission from bulk crystalline silicon.* Applied Physics Letters, 2003. **82**(18): p. 2996-2998.
134. Conibeer, G., et al., *Silicon quantum dot nanostructures for tandem photovoltaic cells.* Thin Solid Films, 2008. **516**(20): p. 6748-6756.
135. Green, M.A., *Recent developments in photovoltaics.* Solar Energy, 2004. **76**(1-3): p. 3-8.
136. Shockley, W. and H.J. Queisser, *Detailed Balance Limit of Efficiency of P-N Junction Solar Cells.* Journal of Applied Physics, 1961. **32**(3): p. 510-&.
137. Sivakov, V., et al., *Silicon Nanowire-Based Solar Cells on Glass: Synthesis, Optical Properties, and Cell Parameters.* Nano Letters, 2009. **9**(4): p. 1549-1554.
138. Kruger, J., et al., *High efficiency solid-state photovoltaic device due to inhibition of interface charge recombination.* Applied Physics Letters, 2001. **79**(13): p. 2085-2087.
139. Kamat, P.V., *Quantum Dot Solar Cells. Semiconductor Nanocrystals as Light Harvesters.* Journal of Physical Chemistry C, 2008. **112**(48): p. 18737-18753.
140. Danek, M., et al., *Synthesis of luminescent thin-film CdSe/ZnSe quantum dot*

composites using CdSe quantum dots passivated with an overlayer of ZnSe. Chemistry of Materials, 1996. **8**(1): p. 173-180.
141. Greenham, N.C., X.G. Peng, and A.P. Alivisatos, *Charge separation and transport in conjugated-polymer/semiconductor-nanocrystal composites studied by photoluminescence quenching and photoconductivity.* Physical Review B, 1996. **54**(24): p. 17628-17637.
142. Waldauf, C., et al., *Highly efficient inverted organic photovoltaics using solution based titanium oxide as electron selective contact.* Applied Physics Letters, 2006. **89**(23).
143. Yang, X.N., et al., *Nanoscale morphology of high-performance polymer solar cells.* Nano Letters, 2005. **5**(4): p. 579-583.
144. White, M.S., et al., *Inverted bulk-heterojunction organic photovoltaic device using a solution-derived ZnO underlayer.* Applied Physics Letters, 2006. **89**(14).
145. Yang, H.B., et al., *NiO/Graphene Composite for Enhanced Charge Separation and Collection in p-Type Dye Sensitized Solar Cell.* Journal of Physical Chemistry C, 2011. **115**(24): p. 12209-12215.
146. Zhang, Q.F., et al., *ZnO Nanostructures for Dye-Sensitized Solar Cells.* Advanced Materials, 2009. **21**(41): p. 4087-4108.
147. Leschkies, K.S., et al., *Photosensitization of ZnO nanowires with CdSe quantum dots for photovoltaic devices.* Nano Letters, 2007. **7**(6): p. 1793-1798.
148. Takanezawa, K., et al., *Efficient charge collection with ZnO nanorod array in hybrid photovoltaic devices.* Journal of Physical Chemistry C, 2007. **111**(19): p. 7218-7223.